SAND78-2306
Unlimited Release
UC-21

Laser Development for Laser Fusion Applications
Research Progress Report
April 1978 - September 1978

Directorate of Physical Research 4200

Sandia Laboratories

113885

Issued by Sandia Laboratories, operated for the United States
Department of Energy by Sandia Corporation.

Accession Number: 3885

Publication Date: Dec 01, 1978

Title: Laser Development for Laser Fusion Applications Research Progress Report, April 1978-September 1978

Personal Author: UC-21

Corporate Author Or Publisher: Sandia National Laboratories, Albuquerque, NM 87185 Report Number: SAND78-2306

Report Prepared for: U.S. Department of Energy Report Number Assigned by Contract Monitor: SLL 80 676

Comments on Document: Archive, RRI, DEW

Descriptors, Keywords: Laser Development Fusion Application Oscillator Amplifier Geometry Electron Beam Iodine Hydrogen Fluoride Kinetic Process Photolysis Atom Research Development Photoionization

Pages: 00077

Cataloged Date: Nov 23, 1992

Contract Number: AT(29-1)-789

Document Type: HC

Number of Copies In Library: 000001

Record ID: 25201

Source of Document: DEW

LASER DEVELOPMENT FOR LASER FUSION APPLICATIONS
RESEARCH PROGRESS REPORT
April 1978 - September 1978

Directorate of Physical Research 4200
Sandia Laboratories
Albuquerque, New Mexico 87185

3-4

CONTENTS

CONTENTS (cont)

LASER DEVELOPMENT FOR LASER FUSION APPLICATIONS
RESEARCH PROGRESS REPORT
April 1978 - September 1978

INTRODUCTION

Advances in knowledge about inertial-confinement fusion (ICF) have been paced by the development of high-power drivers. The laser-driven option to ICF will continue to be paced by the development of advanced high-power lasers. The long-term goal of ICF, commercial power generation, will require an efficient and reliable high-average-power driver. The near-term goal of our research is to provide an alternative to CO_2 and Nd:glass for large-system scientific demonstration studies; the long-term goal is to develop the laser technology that is necessary for commercialization of laser-fusion energy.

Our program addresses three high-power laser systems: iodine, hydrogen fluoride, and Group VI atoms. Both the iodine laser and the HF laser have a demonstrated high-power capability, and experimental results indicate that there are probably no serious problems hindering development of either of these lasers for laser-fusion applications. In both of these technology-development programs, we are making steady technical progress.

The HF laser has a proven high electrical efficiency, a projected overall efficiency of better than 4%, and staging of multimegajoule systems is felt to be possible. If laser-energy-to-thermonuclear-energy gains of a few hundred can be realized, it is an attractive ICF driver. From a capital cost point of view, it is very attractive in comparison with other candidate lasers.

We now know that an iodine laser system can be built that would satisfy all near-term requirements of laser fusion including the driver of an experimental power reactor, but its efficiency needs to be improved before it can be considered as a driver for a commercial ICF power generator. With available technology the best electrical efficiency that can be realized for a ~ 1-MJ, 10-pps iodine laser is 0.4 to 0.5%, and the overall efficiency including regeneration of laser medium starting chemicals is 0.35 to 0.4%. This projected efficiency requires very high laser-energy-to-thermonuclear-energy gains for economically attractive electric power generation and its low electrical efficiency would require a prohibitively high capital investment in the pulse power source. We are investigating both surface discharges and $HgXe^*$ exciplexes as ways to improve the efficiency (up to 2%) of the iodine laser.

The class of lasers based on the excitation of the p^4 ^1S state of Group VIA atoms (e.g., O, S, Se, Te) with energy extraction on the p^4 $^1S \rightarrow p^4$ ^1D or p^4 $^1S \rightarrow p^4$ $3P$ transition offers long energy-storage times since the ^1S state exhibits a long radiative lifetime and is resistant to deactivation by a wide variety of other species. Also, these transitions occur at what are thought to be excellent wavelengths (459 nm to 790 nm) for laser fusion and exhibit stimulated emission cross sections that are low enough to inhibit parasitic amplified spontaneous emission but not so low that the medium cannot be saturated at reasonable energy fluences. The emphasis of our work on this class of lasers is to perform laboratory kinetic studies that will permit the development of a model that can be used to project large-system laser performance. According to what we know now, an overall

efficiency of up to 3% may be possible.

The key highlights achieved during this report period include:

1. Near-diffraction-limited beam quality was demonstrated for a switched-out 6-ns portion of a HF-laser amplified beam.

2. HF laser characteristics for high-pressure operation were established.

3. Details of individual-line suppression of ASE in an HF amplifier were worked out.

4. Design of the Phoenix II HF amplifier cell was frozen and the experimental details were worked up for the first large-scale study of angular multiplexing: a pulsewidth compression scheme.

5. Establishing that iodine lasers can be stabilized against self focusing.

6. Demonstration of an efficient method to chemically regenerate iodine-laser-medium starting materials and showing that chemical regeneration will not be an important consideration in the overall efficiency of a large iodine laser system.

7. Theoretical determination of the photo-ionization cross section for sulfur $(3p)^4$ ^1S_O and selenium $(4p)^4$ ^1S_O.

8. Measurement of the yield of $S(^1S_O)$ by photolysis of OCS by 157-nm laser light at intensities up to 0.1 J/cm^2.

9. Demonstration that photoionization of $S(^1S)$ and electron runaway processes will not compromise the performance of the $S(^1S)$ laser if suitable precaution is exercised.

10. Modeling studies of the chemically pumped iodine laser suggest that it may be an attractive candidate driver for commercial application of ICF.

11. Measurements of fluorescence efficiencies for HgXe* exciplexes excited by an electric discharge.

HF-LASER PROGRAM

OVERVIEW

The HF laser is an attractive candidate driver for a large-system ICF scientific demonstration facility, for an ICF experimental power reactor and for a commercial laser-fusion power reactor. Its proven high electrical efficiency offers a relatively low capital cost and high reliability, and staging of multimegajoule systems is felt to be possible. Also, its overall efficiency is high enough and its projected capital cost is low enough to make it look attractive from a cost-of-electricity point of view if laser-energy-to-thermonuclear-energy gains of a few 100 can be realized. The near-term goal of the HF-laser program is to develop a technology and engineering data base so that a meaningful tradeoff analysis for the various candidate ICF advanced drivers can be made on a time scale consistent with DOE planning.

Previous accomplishments of our program have included demonstrations of high efficiency and high energy capability, efficient energy extraction from HF amplifiers, good beam quality and focusability, and short-pulse generation and amplification. In this reporting period, beam quality has been determined to be near-diffraction limited for a short pulsewidth (6 ns to 25 ns) oscillator-amplifier chain, suppression of amplified spontaneous emission has been demonstrated on an individual spectral line, high-pressure characteristics have been determined for the Phoenix I amplifier, and detailed comparisons between the kinetic code and experiments have been made.

Details of two major upcoming experiments are also included in this report. The first is energy extraction and beam quality measurements on the Phoenix I amplifier operating under saturated output power conditions. The second experiment, using a newly designed amplifier (Phoenix II), is designed to demonstrate the concept of angular-multiplexing: a pulse width-compression scheme.

OSCILLATOR-AMPLIFIER STUDIES USING THE λ-GEOMETRY ELECTRON-BEAM-INITIATED HF AMPLIFIER

In the last report,[1] the radially dependent electron-beam-energy deposition profile of the λ-geometry amplifier was presented and compared with the laser output radial energy density distribution when the system was operated as an oscillator. We have also made comparisons of the radial energy variation of laser-amplifier output with its level of excitation counterpart. The input intensity to the amplifier was essentially uniform over its aperture. The energy density in the input beam was about 32 mJ/cm^2 in a pulse width (FWHM) of about 100 ns. The radial distribution of the amplifier output energy density is shown in Fig. 1 for two different total pressures. These results confirm that the electron-beam deposition in the λ-geometry amplifier (λ-amplifier) is highly nonuniform in the radial direction. The difference between the 620-torr data and the 775-torr data seems to indicate that the electron-beam was slightly off axis, toward the outside of the laser tube, as the beam propagated around the corner. This may mean that the magnetic field used to guide the electron-beam into the amplifier tube should be adjusted for each operating pressure to assure a more nearly symmetrical deposition profile.

Since the electron-beam-energy deposition is radially nonuniform, the rate of atomic fluorine production and, hence, the production rate of excited HF molecules will be radial nonuniform. This should result in the temporal behavior of the amplified pulse also having a radial variation. The radial variation of the pulse width (FWHM) is shown in the upper curve of Fig. 1. These results show a radial variation of pulse width (FWHM) of about 50% with the λ-geometry amplifier.
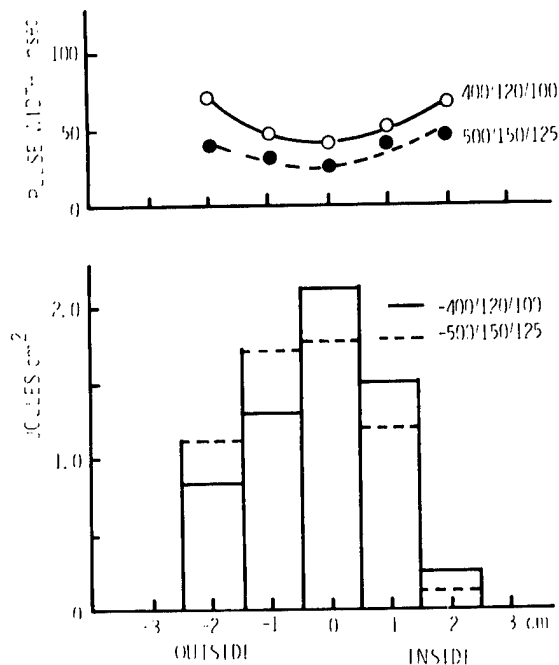
Fig. 1. Pulse width and radial output energy profile from an axial amplifier for two different pressures. These results were obtained for an input intensity of 10^5 W/cm^2. These results confirm the nonuniform electron-beam energy deposition.

BEAM QUALITY STUDIES USING THE DISCHARGE OSCILLATOR-PREAMPLIFIER AND THE λ-AMPLIFIER

The electron-beam-initiated λ-geometry amplifier which is initiated by a PI Model-110A electron-beam machine will be used in future experiments as a preamplifier. This system will be used to saturate the Phoenix I amplifier and for angular multiplexing experiments with the Phoenix II amplifier. The experiments described here were to determine the optical quality of amplified beams and to further determine if a short pulse (5 ns to 25 ns) could be amplified

without degrading the beam quality. Previous experiments with a transverse-initiated cell (Phoenix I) indicated that a high-optical-quality beam could be amplified without degrading the beam. However, the λ-amplifier is excited nonuniformly in the radial dimension. Extraction experiments using this amplifier and the SF_6-HI fueled oscillator-amplifier system have shown that about 50% of the energy can be extracted from the amplifier. [2]

The first measurements of the beam quality were made by using a 25-ns pulse that was generated by the polarization rotation method described previously. The beam quality of the input beam was measured by using lateral shearing interferometry, where reflections from the front and rear surfaces interfere to form a fringe pattern. Information about the radius of curvature of the beam and the phase front distortion is contained in such patterns. [3] Fringe patterns for the input beam were measured by using the pyroelectric vidicon system that has been described in a previous report. The beam quality measured was in agreement with beam quality measurements previously reported. The output beam was recorded as a burn pattern on unexposed developed Polaroid film. The resulting measurement is shown in Fig. 2 where it appears that the wavefront distortion is less than $\lambda/2$ over the diameter of the beam. The tilt of the fringes indicates the curvature of the wavefront at the point of measurement. The curvature can be adjusted by using the beam expanders in the system. However, the tilt in the fringes indicate that the curvature of the wavefront or the divergence of the beam was approximately 400 μrad. Comparison of the input and output beams indicates that the beam through the axially initiated amplifier was not degraded to a measurable degree.

A more quantitative measurement of the beam quality is the measurement of the energy that can be focused through a pinhole. These measurements have been made for the Phoenix I and have been previously described. Measurements of output optical quality from the λ-geometry amplifier were made by using a 5-m-focal-length mirror. The beam intensity was reduced by using front surface

reflections from quartz wedges in order to eliminate the possibility of air breakdown at the pinhole. The pulse length for these experiments was 25 ns. The results are shown in Fig. 3 where the pinhole size has been converted to an equivalent angle. Data were taken down to 40% transmission which corresponded to a 0.9-mm pinhole.
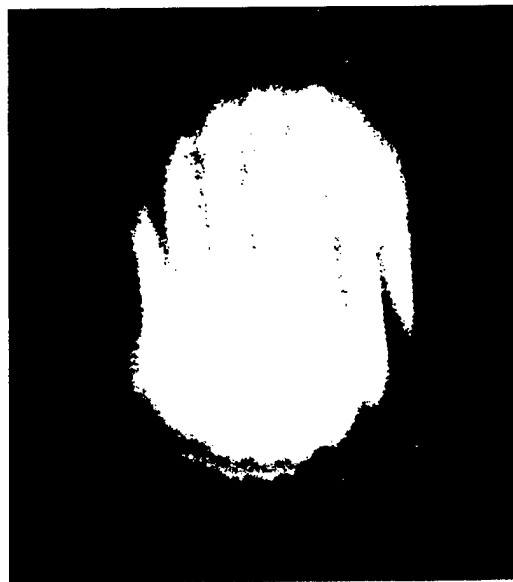
Fig. 2. Lateral shearing interferograms from an axial initiated amplifier. This interferogram shows very little phase-front degradation of the beam from the amplifier.

The beam quality was further examined with a short focal length mirror (45.7 cm) in a vacuum. The vacuum was necessary in this case to prevent air breakdown. The apparatus used here was the same as that described previously. [4] The pulse length was reduced to ~ 6 ns in width for this set of experiments. The minimum pinhole for this experiment was 200 microns where the measured maximum transmission was 92%. The data from this experiment are shown in Fig. 3.

From a comparison of this data at the 84% transmission point, it appears that the beam is approximately two to three times diffraction-limited, which implies the input beam is not seriously degraded by the axially initiated amplifier.
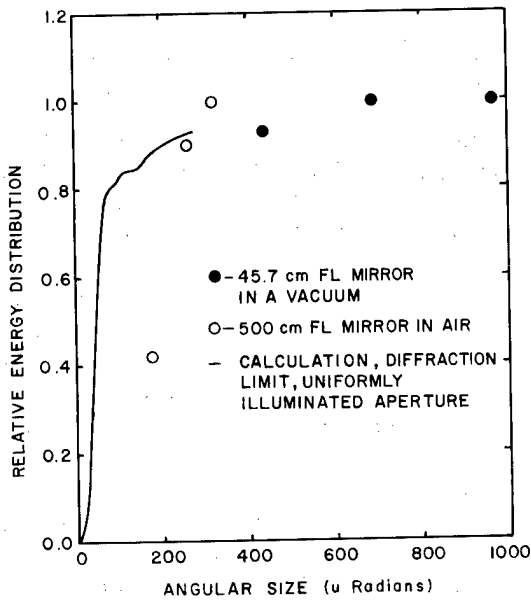
Fig. 3. Focal spot energy distribution obtained from the axially initiated amplifier. A long focal length focusing mirror was used to focus in air and a short focal length mirror was used to focus in a vacuum.

SHORT PULSE AMPLIFICATION

In order to amplify a short pulse (~ 5 ns) with the λ-geometry amplifier, a polarization-rotation technique is used. This technique is selected because HF is a nonstorage laser system and requires a signal in the amplifier during the total time of positive gain to suppress amplified spontaneous emission.

The technique of polarization rotation is illustrated in the schematic diagram shown in Fig. 4. The output from the oscillator is passed through a polarizer to produce p-polarization and then through an electro-optical crystal. This crystal, which is CdTe in the present system, can then be used to rotate the polarization and produce a short pulse with s-polarization. This signal is then amplified and the output is incident onto a small-angle-wedge beam splitter oriented at the Brewster angle. The long pulse with p-polarization is transmitted through the Brewster angle plate, but during the short period of time when the polarization is rotated to s-polarization, some fraction of this signal is reflected from the two surfaces of the Brewster angle plate. Only the reflection from the front surfaces of the wedged plate is used.

The reflection efficiency for the s-polarized light will depend upon the index of refraction of the material. Some of the materials which have or are being considered for use are listed below.

Material	Refractive Index ($\lambda \sim 3\mu$)	φ Brewster (deg)	Reflectance (%)
Quartz	1.419	54.8	11.3
ZnSe	2.44	67.7	50.7
Si	~ 3.0	71.6	64
Ge	4.057	76.2	78.4
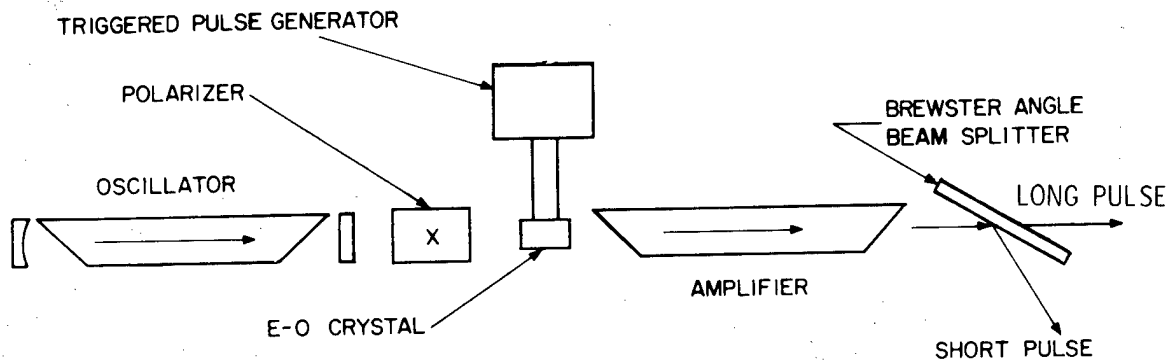
Fig. 4. Schematic diagram showing technique for generation and amplification of short pulses using polarization rotation.

With the polarization-rotation technique described in the preceding section, we have amplified a nominal 6-ns pulse. The Brewster angle beam splitter was quartz.

The results of amplifying a short pulse utilizing the polarization technique are shown in Fig. 5. The upper curve shows the temporal behavior of the s-polarization input pulse. The p-polarization component of the input pulse is not shown, but it has a pulse width (FWHM) of about 100 ns. The long pulse started at about 40 ns. The amplified pulse (s-polarization) is shown in the lower curve. There is essentially no distortion of the pulse with both the input and output having a pulse width of 6 ns. The contrast ratio, that is the ratio of the signal prior to the amplified pulse to the peak pulse signal, is estimated to be greater than 20. Additional measurements will be necessary to determine the best contrast ratio that can be obtained with this technique.
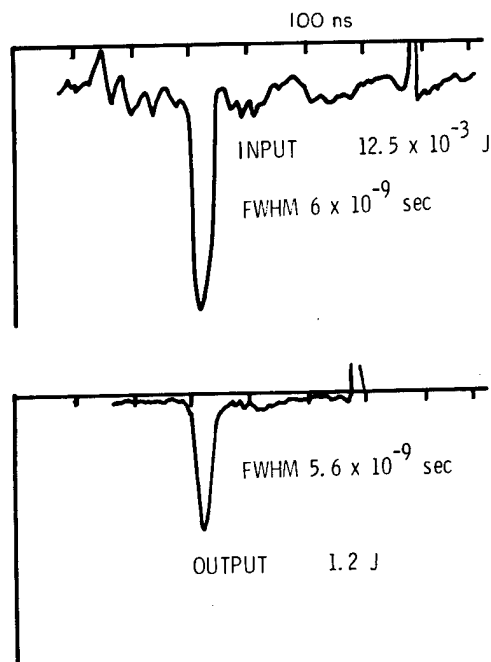
Fig. 5. Input and amplified pulse using an axially initiated H_2-F_2-O_2 amplifier. The energy gain of this system was about 96. The full width at half max (FWHM) of the input pulse was 6 ns and the FWHM of the output pulse was 5.6 ns.

Suppression of Amplified Spontaneous Emission

Measurements of amplified spontaneous emission (ASE) which were obtained during the energy extraction experiments on the Phoenix I amplifier[5] indicated that the ASE was reduced only a factor of three for an input intensity of 10^4 W/cm^2. Increasing the input power above this level did not further reduce the ASE. These results are not in agreement with the HFOX code which predicts a much larger suppression.

Measurements of the ASE radiated by the λ-geometry amplifier have also been made. These measurements have been made under two conditions: 15-degree windows and Brewster angle windows on the amplifier. The calorimeters used in the ASE measurements were arranged so that they could detect the energy within a solid angle of 1.5 x 10^{-2} sterdians. This was about twice the geometric solid angle subtended by the amplifier.

With an input intensity of about 1 x 10^5 W/cm^2 from an oscillator-preamplifier system the ASE reduction was a factor of 1.5 with 15-degree windows and 1.9 with Brewster angle windows. The magnitude of the energy radiated by ASE with Brewster angle windows was a factor of two less than it was with 15-degree windows. These results would seem to indicate that there is some feedback from the 15-degree windows resulting in increased ASE, but if this is the case, then we would have expected a greater reduction in ASE with the Brewster angle windows.

Since the HF laser operates on about 50 vibration-rotation transitions, it was felt that a better understanding of ASE suppression could be obtained by making measurements on a single transition. A schematic diagram of the experimental arrangement used to monitor the ASE on the $P_1(7)$ transition is shown in Fig. 6. The intensity of the incident $P_1(7)$ radiation was monitored with a beam splitter and a monochromator. The ASE radiated at a small angle to the amplifier optic axis (2-degrees) was monitored by a monochromator.
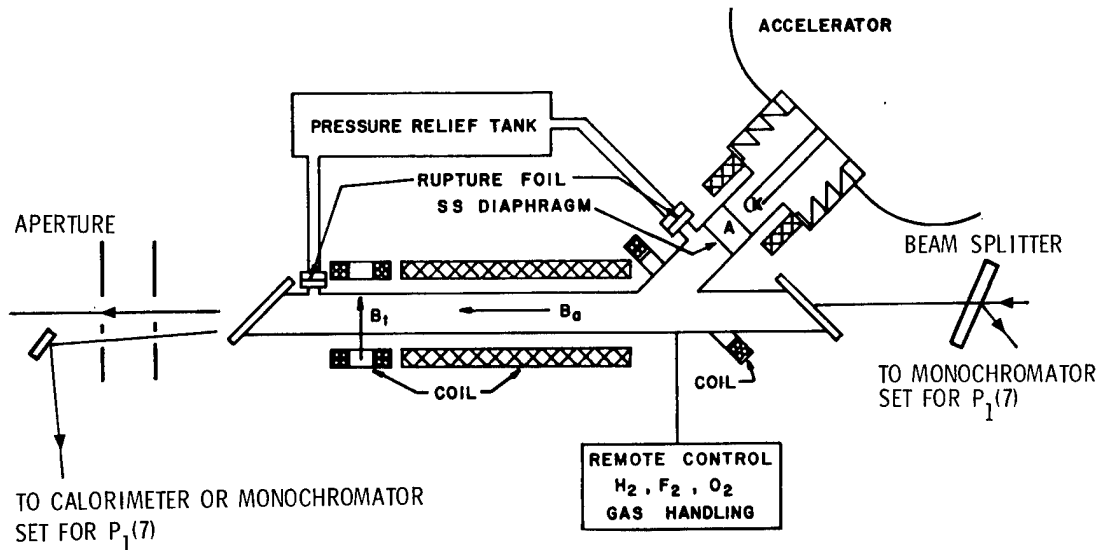
Fig. 6. Schematic diagram of the experimental set up to investigate amplified spontaneous emission. The beam splitter was used to monitor the input intensity of the $P_1(7)$ lines. The apertures were used to allow only radiation at 2-degrees from the centerline to be monitored.

The results of these measurements with Brewster angle windows on the amplifier are illustrated in Fig. 7. Curve (b) shows the temporal behavior of the incident $P_1(7)$ line. The peak intensity is estimated to be about 2×10^2 W/cm^2. Curve (d) shows the temporal behavior of the $P_1(7)$ line with no incident radiation. Curve (c) illustrates the suppression of $P_1(7)$ ASE with an incident $P_1(7)$ radiation. The ASE on the $P_1(7)$ transition shows a large decrease as soon as the $P_1(7)$ radiation is incident.

These same experiments were done with 15-degree windows on the amplifier. In this case, with an incident intensity of about 10^3 W/cm^2, the reduction of ASE on the $P_1(7)$ line was not as good as when the amplifier had Brewster angle windows. These results seem to indicate that with 15-degree windows there is some feedback which allows parasitic oscillation to occur in the amplifier.

These preliminary results indicate that to reduce ASE from an amplifier it will probably be necessary to achieve the following:

1. Good temporal match on all spectral lines between oscillator and amplifier. This also means that it will be necessary to achieve a

good spectral match between the oscillator and amplifier.

2. Reduction of feedback which might allow parasitics oscillation to occur in the amplifier.

ENERGY AND PULSE WIDTH CHARACTERISTICS OF PHOENIX I

Measurements of laser energy output and laser pulse width as a function of H_2-F_2-O_2 pressures for the Phoenix I amplifier configured as an oscillator have been described in a previous progress report.[6] In those measurements, the pressure ratio of $F_2:O_2:H_2$ was held fixed at 1.0:0.3:0.25. With a flat total reflector on one end of the laser cell and a sapphire output coupler on the opposite end, the output energy increased from 150 J at an F_2 pressure of 400 torr to 220 J at an F_2 pressure of 1200 torr. Over this pressure range the pulse width remained nearly constant at ~50 ns. It is desirable to obtain amplifier inversion times of the order of 20 ns so that angular multiplexing staging, that will reduce the pulse-width to about 10 ns, is simple and inexpensive. Calculations indicate that the use of

13

hydrogen-lean mixtures at higher total pressures should reduce pulse widths and at the same time increase the chemical efficiency of the amplifier.
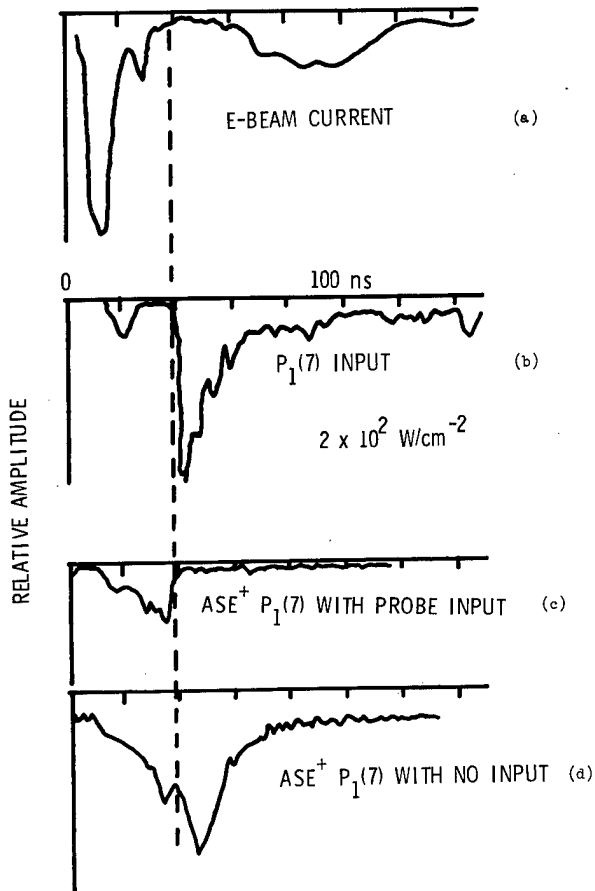
Fig. 7. Suppression of amplified spontaneous emission ($P_1(7)$ line). The upper curve shows the temporal behavior of the electron-beam current. The next curve shows the temporal behavior of the $P_1(7)$ input. The next curve shows the suppression of the $P_1(7)$ line from the amplifier. These data were obtained at 2-degrees from the amplifier optical axis. The bottom curve shows the $P_1(7)$ amplified spontaneous emission from the amplifier with no input.

For the experiments reported here, Phoenix I was configured as an oscillator to investigate the laser characteristics as a function of F_2 pressure for a hydrogen-lean mixture. In these experiments, the H_2 pressure was held constant at 200 torr while the F_2 pressure was varied from 380 to 3040 torr. In order to reduce the probability of mixture predetonation the O_2 pressure was varied as $P_O = 240 + 0.05 P_F$ where P_O is the oxygen pressure and P_F is the fluorine pressure. For these measurements, the amplifier cell was fitted with a flat gold mirror on one end and a sapphire output coupler on the opposite end. The multimode output energy was measured by using a 20-cm-diameter surface calorimeter, collecting the energy reflected from a quartz beam splitter. The temporal history of laser radiation was recorded with a AuGe (77 K) detector.

Figure 8 shows the laser energy output as a function of pressure. The pressure, shown on the abscissa, consisted of 95% fluorine and 5% oxygen. The laser output energy monotonically increased for pressures from 400 to 2800 torr, then decreased slightly at a pressure of 3200 torr. The large scatter in data may be due to variations in mixture homogeneity since the 200 torr of hydrogen was added last and turbulence of the injected gas was the predominant mixing mechanism. The laser output energy shown in Fig. 8 does not increase as rapidly with pressure as does the anticipated electron-beam deposition. Cyltran[7] calculations indicate that for a total pressure of one atmosphere about 2% of the available electron-beam energy is deposited in the gas mixture. Therefore, it is expected that the deposited energy should increase about linearly with increasing pressure. The decrease in electrical efficiency with increasing pressure is accountable in part to the burn being completed before the end of the electron-beam pulse at the higher pressures. Computer calculations using Sandia's HF laser code are planned to compare with the measured output laser variation with pressure.
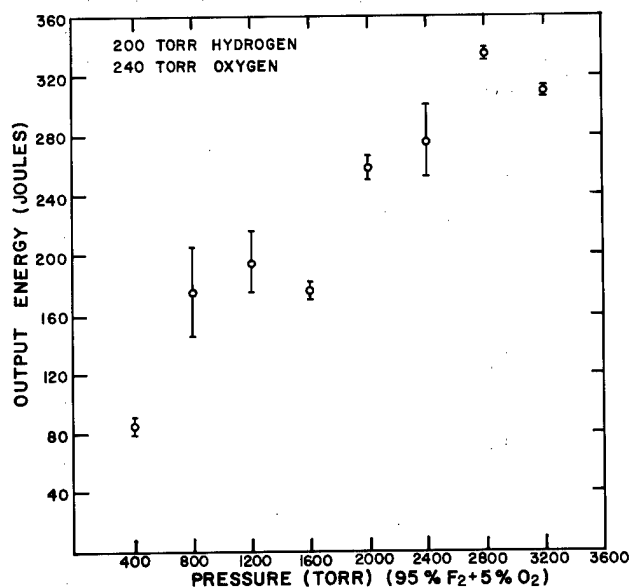
Fig. 8. Laser output energy as a function of pressure.

Laser pulse width (FWHM) as a function of pressure is shown in Fig. 9 for the same conditions that were used in Fig. 8. The pulse width decreased from ~ 50 ns at 400 torr to 24 ns at 3200 torr. While this latter value is near the desired 20 ns, the variation in pulse width with pressure also needs to be compared with computer calculations.
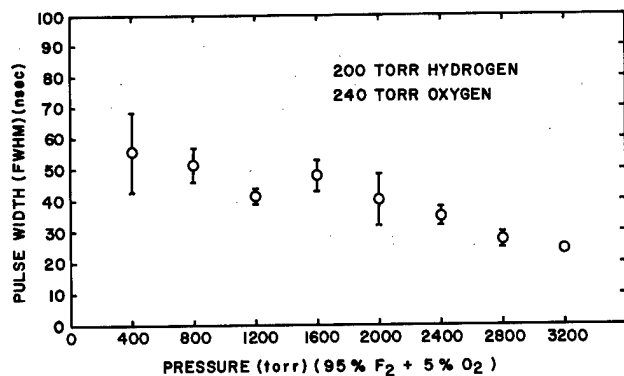
Fig. 9. Laser pulse width as a function of pressure.

The maximum chemical efficiency (laser energy output divided by total exothermic energy released in the H_2-F_2 reaction) achieved with the 200 torr H_2 mixtures was approximately 3%. This value is based on an excited volume of 4l.

A limited number of measurements was also made by using the same cavity geometry as for the above measurements but with even less hydrogen in the mixture. Pressure ratios of $F_2/O_2/H_2$ of 800/240/100 and 3200/408/100 torr were used. For the 800-torr F_2 case, the laser energy was 149 J and the pulse width (FWHM) was 88 ns. At 3200-torr F_2 the laser energy was 226 J and the pulse width was 45 ns. Laser burn patterns for these low-hydrogen pressure cases indicated a very nonuniform initiation over the amplifier cross section. Intense film damage was observed in a region around the horizontal diameter with considerably less damage through the remainder of the aperture. This suggests that, for these conditions, the electron-beam did not spread sufficiently to completely fill the cross section of the amplifier.

The maximum chemical efficiency obtained with the 100-torr H_2 mixtures was about 4%, assuming uniform initiation of the entire cell volume.

Experiments were also done on Phoenix I to investigate effects of nonuniform electron-beam distribution on laser pulse width. Electron-beam energy distribution along the optical axis of the laser cell has previously been measured to have a FWHM of 44 cm.[8] To investigate whether slower H_2-F_2 reactions at the ends of the laser cell where the energy density is smaller contribute to a longer pulse width, re-entrant window holders were used on each end to shorten the active length from 91 cm to 46 cm. The arrangement is shown schematically in Fig. 10. For these measurements, a gas mixture of F_2:O_2:H_2 of 800:240:200 torr was used and the results with the re-entrant windows were compared with measurements when sapphire windows were placed directly on the ends of the Phoenix I cell. With the windows on the ends of the cell, the average energy output (sum of both ends) was 168 J and the average laser pulse width was 43 ns. With the 46-cm-long cavity using re-entrant windows, the total energy (both ends) was 71 J and the average pulse width was 56 ns. The reason for the increase in pulse width with the short cavity is not understood at this

time. However, it is apparent that the smaller electron-beam energy density near the ends of the amplifier cell is not responsible for a lengthening of the laser pulse. The ratio of the energy output with the 46-cm cavity to the output with the 91-cm cavity is 0.42, while the ratio of the areas of the apertures for the two cavities is 0.44. Therefore, if the laser radiation were propagating predominantly parallel to the cavity axis, the energy measurements would be consistent with both cavities containing the same laser energy. Further measurements would be required to determine if this is indeed the case.
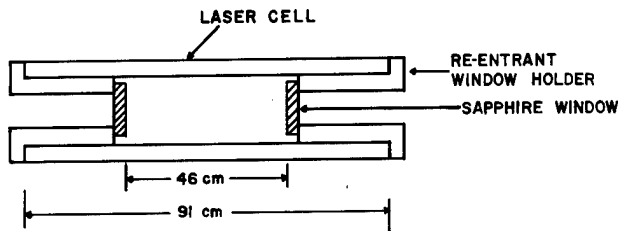
Fig. 10. Re-entrant window configuration for Phoenix I.

The output energy of the amplifier configured as an oscillator was compared for two different values of cavity coupling to estimate extractable energy. For these comparisons, the $F_2/O_2/H_2$ pressures were 800/240/200 torr. In the first case, the cavity reflectors, spaced at 91 cm, consisted of a gold mirror and a sapphire flat. The product of reflectivities, R_oR_L, for this cavity was 0.134. In the second case, sapphire flats were placed on each end of the Phoenix cell giving a value of R_oR_L of 0.019. Figure 11 shows the normalized output energy for the two couplings. The output energy was constant, within experimental error, for these largely different couplings. This indicates that the energy measured with the amplifier configured as an oscillator gives a good estimate of the energy that can be extracted from Phoenix I operated as an amplifier.
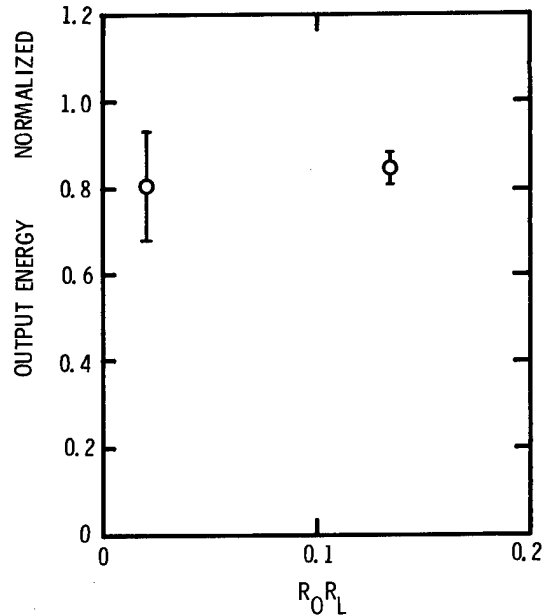
Fig. 11. Normalized output energy as a function of cavity coupling.

SATURATED PHOENIX-I AMPLIFIER EXPERIMENT

The objectives of the saturated amplifier experiment are to determine the efficiency of energy extraction at input levels up to 10^7 W/cm^2 and to determine the optical beam quality.

The experimental setup is shown schematically in Fig. 12. The output from a small pin discharge is amplified by two discharge driven preamplifiers. The output of this system is about 1 J in a pulse (FWHM) = 100 ns and consists of about 23 P-branch lines. These spectral lines are listed below:

$P_1(6-8)$ $P_4(4-9)$

$P_2(4-8)$ $P_5(4-7)$

$P_3(5-9)$

16
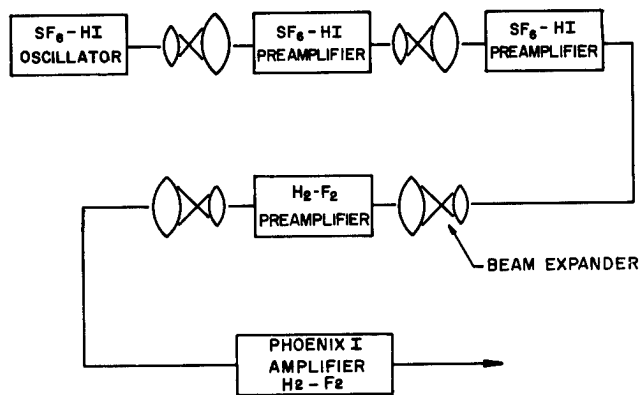
Fig. 12. Schematic diagram of saturated
amplifier experiment.

The output from the oscillator-preamplifier
system will drive an electron-beam-initiated
intermediate amplifier operating with mix-
tures of H_2 and F_2. The output from this
amplifier should be about 30 J with a FWHM
of 40 ns. This optical beam will be expanded
and directed into the Phoenix I final amplifier.
The energy extracted from this amplifier
will then be measured as a function of input
intensity.

Measurements will also be made of the
amount of total amplified spontaneous emis-
sion (ASE) radiated by the Phoenix amplifier
and also the amount of ASE radiated on a
single vibration-rotation transition.

After the energy extraction part of the experi-
ment is completed, the output beam will be
focused through small diameter pinholes by
using an off-axis parabolic mirror to deter-
mine the beam quality.

At present, the energy extraction experiment
is being set up and timing of the various
oscillator-amplifier drivers is underway.
The present plans are for both parts of this
experiment to be completed by the end of
December 1978.

PLANS FOR TWO-BEAM ANGULAR MULTI-
PLEXING DEMONSTRATION IN A LARGE-
VOLUME HF AMPLIFIER

Angular multiplexing has been proposed as a
technique for short pulse amplification in
high-gain systems.[9] Generally, the techni-
que allows for the amplification of any num-
ber of pulses, sequentially arranged in time
so that their summed pulse widths approxi-
mate the total gain time in the amplifier
medium. By coding each beam in space in
some manner, the beams can then, in prin-
ciple, be separated after the amplifier and
then recombined temporally and spatially to
create a single, short pulse. In practice,
the coding can be accomplished by bringing
in each beam at a slightly different angle
with respect to the amplifier axis. The con-
cept has been demonstrated on a small scale,
using the high-gain infrared transition in
xenon around 3.39 microns.[10] Using two
separate oscillator beams, this study
showed that with pulses whose pulsewidths
(FWHM) were approximately one-half the
measured gain time of the amplifier each
was amplified without significant temporal
distortion of the individual pulses. Also,
the amplified spontaneous emission (ASE)
was well suppressed.[10] The experiment
described here is intended to evaluate the
angular multiplexing technique in an
electron-beam-initiated HF amplifier of ap-
propriate scale (several hundred joules per
beam). This experiment is intended to com-
mence in the spring of 1979.

Design Considerations

The amplifier cell (Phoenix II) will be driven
by the Maxwell Poco Beam Electron-Beam
Machine, as is the current cell (Phoenix I).
In order to provide scaling information for
the HF code and to allow for up to several
hundred joules per beam in the two-beam
multiplexing experiment, the size of the
Phoenix II cell was chosen to be four to five
times the size of the Phoenix I cell. Figure
13 shows a schematic illustration of the
Phoenix II cell together with some of the
pertinent characteristics. The dimensions
of the two probe beams are shown consider-
ably smaller than the optimum size in order
to emphasize their individual spatial rela-
tionships within the amplifier. A rectangu-
lar cell was chosen in order to minimize the
volume in the cell which is unprobed by
either beam. For a given beam path length,
a circular beam tends to fill a slightly

smaller volume in a cylindrical cell than does a rectangular beam in a rectangular cell. The unprobed volume is not a severe design restraint, however, since it could be completely eliminated by a beam on axis or with suitably designed baffles.

- 15 cm SQUARE APERTURE
- VOLUME = 15.8 LITERS
- WINDOWS – AR COATED SAPPHIRE (1.25 ln THICK) AT 10° TO NORMAL
- 2.5 % UNPROBED VOLUME (TWO BEAMS) WITH 15.2 METER PATH LENGTH
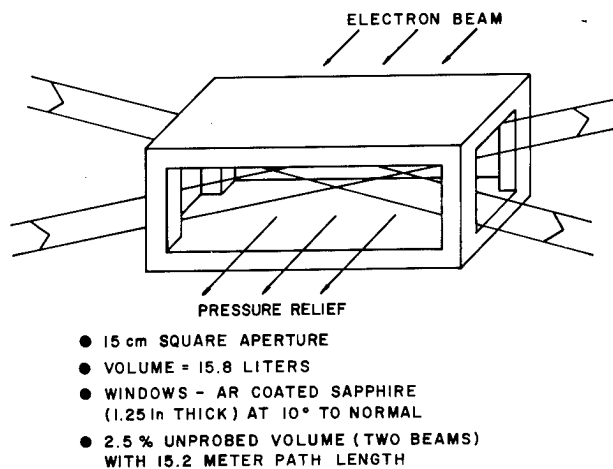
Fig. 13. Schematic of the Phoenix II cell. The two oscillator beams are shown smaller than their true sizes relative to the cell. The incident angles are exaggerated to illustrate the spatial relationships in two-beam angular multiplexing.

The electron-beam entrance foil and the overpressure blowout diaphragm structure are both designed to be in a re-entrant configuration. In this manner, the active volume is defined in part by these two structures and any "dead" volume along the sides which is not accessible to the probe beams is almost eliminated.

For rectangular beams of height W_a (equal to the amplifier height) and width W_b and for a given optical path length L (measured from the cell center), the minimum angle (α) that one beam makes with respect to the amplifier axis is given by (for small α)

$$\alpha = \frac{W_b \left(\dfrac{d}{W_b} + 0.5 \right)}{L} \tag{1}$$

where 2d is the separation of the beams at distance L (determined from mirror mounting considerations) and W_b is chosen to be as large as possible accounting for the vignetting created in the off-axis configuration:

$$W_b \leq \frac{W_a}{1 + \dfrac{L_a}{L} \left(\dfrac{d}{W_b} + 0.5 \right)} \tag{2}$$

where L_a is the overall length of the amplifier cell. From Eqs (1) and (2), one sees that the desired beam spacing at distance L determines the appropriate beam width and relative input angle. This in turn determines the fraction of the amplifier volume which, for the two beam case, is not probed by either beam. For a rectangular cell this volume is given by

$$V = \frac{V_a L_a \, \mathrm{Tan}\, \alpha}{2W_a} \simeq \frac{V_a L_a \alpha}{2W_a} \tag{3}$$

where V_a is the amplifier volume. For the Phoenix II cell (L_a = 80 cm) and for a path length of 15.24 m (50 ft), one obtains α = 9.5 mrad, V/V_a = 2.5% for 2d = W_b.

The energy deposition characteristics of Phoenix II will depend largely on the new diode operation which is currently in the design stage. However, these characteristics are expected to be similar to those of Phoenix I (about 17 J/ℓ-atm deposited for the "standard" mixture of F_2:O_2:H_2 = 1:0.3:0.25). For a 2-atm mixture under these conditions, a trial run was done with Sandia's HF code and the results are shown in Fig. 14. The top graph shows the ASE time history under these conditions, and the bottom graph illustrates the input beams (solid lines) and the calculated amplifier outputs (dashed lines). For this case, the two input beams were chosen to have a pulse width of 25 ns (FWHM) with relative time delays selected so that the sum of the input intensities in the region where the beams overlap was more or less constant. Inasmuch as the code does not distinguish

between the two beams in the region where they overlap, the bottom curves in Fig. 14 were obtained by apportioning the computed output intensity among the two beams in accordance with their relative input intensities at any given point. From this figure, it is clear that the two areas of concern regarding possible temporal pulse distortion are at the leading edge of the first pulse and the trailing edge of the second pulse: these are the two periods of nonlinear gain in the amplifier. In order to perform the experiments at pulse widths in the range of 10 ns to 15 ns per beam, it is assumed that the Phoenix II amplifier can be scaled down in

pulse width in accordance with Fig. 14. Figure 15 shows the experimental layout including the oscillator-preamplifier with a polarization switch to create the short (10 ns to 15 ns) pulse.[11] This beam is amplified in the electron-beam-initiated preamplifier and the short pulse is switched out. This beam is subsequently filtered and beam expanded to match the Phoenix II cell. A 50-50 beam splitter splits this beam into two beams of approximately equal intensity. By translating this splitter, it is possible to create the desired path differences between the two beams. According to current estimates, we expect nearly 10^7 W/cm^2 (single beam) input to the Phoenix II amplifier and nearly 5 x 10^6 W/cm^2 for the angular multiplexing experiment.

Fig. 14. Results of a preliminary run with Sandia's HF code applied to the Phoenix II experiment. The top curve shows the duration of the amplified spontaneous emission (ASE) in the forward (+) and backward (-) direction with no input beam. A two-atm mixture ($F_2/H_2/O_2$ = 800 torr/200 torr/240 torr) with e-beam deposition similar to Phoenix I was assumed. The bottom curves show the two input beams (solid lines) and the resultant amplified signals (dashed lines).

Fig. 15. Beam paths and principle equipment layout for the two-beam angular multiplexing experiment. The dots and dashes correspond to the two equally intense beams which are created at a 50-50 beam splitter. The diagnostic layouts are not shown here.

Experimental Goals

The two-beam multiplexing experiment is intended to demonstrate efficient energy extraction from the Phoenix II amplifier while suppressing the ASE from this amplifier. The observed parameters will be evaluated against the single-beam oscillator-amplifier characteristics which are expected to cover a range of input intensities up to 10^7 W/cm^2. Measurements will include the contrast ratio of amplified pulses, beam quality using shear-plate interferometry, ASE (forward and backward), and spatial profiles of the beams. It is expected that each of these parameters will depend strongly on the individual pulse widths and relative time delays. Provisions have been made to allow the variation of both of these parameters over the expected range.

DIAGNOSTIC EXPERIMENTS FOR DETAILED CODE COMPARISON

In an attempt to explain some of the discrepancies that exist between the HF kinetic model and experiments, a small electron-beam-initiated laser is being constructed that will be used solely for diagnostic experiments. This laser will use an existing electron-beam system (Physics International Model 215 WR Pulserad). The laser cell is designed so that on the order of 100 J/1-atm will be deposited uniformly in the gas, which is similar to deposited energy of the larger electron-beam-initiated lasers. Detailed energy deposition measurements will be done with segmented totally stopping calorimeters.

The diagnostic experiments to better understand the kinetics of the laser will include measurements of (1) electron-beam deposition in F_2, (2) the density of fluorine atoms initially produced by the electron-beam, (3) the rate of F_2 disappearance in a standard laser gas mixture, (4) the small-signal gain on several vibration-rotation transitions, and (5) time-resolved laser-output spectra.

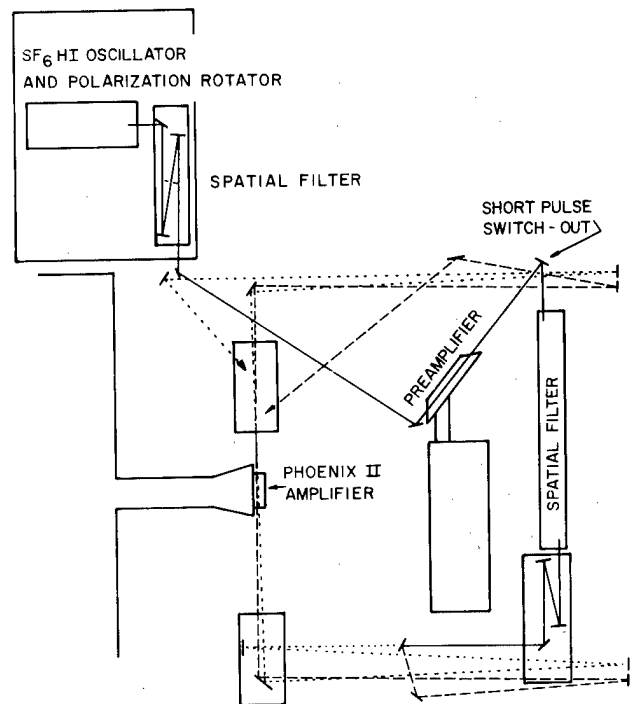The F-atom concentration will be measured by the HCl titration technique. This involves reaction of F with HCl to produce HF. The number of HF molecules produced will then be determined by absorption spectroscopy. One potential problem could be the reaction of Cl with F_2 to produce an additional F atom. However, evidence in the literature indicates that this second reaction will be slow on the time scale of the experiment. Also, there is data that suggest that electron-beam dissociation of HCl will be small.

The rate of F_2 disappearance, which will yield the total chain-reaction time, will be monitored by using a frequency-doubled dye laser to measure absorption on the 285-nm band of F_2. Potential problems here arise from the fact that in a standard laser mix the temperature increases significantly following electron-beam initiation. The F_2 absorption cross section can be inferred at elevated temperatures, but a measurement may be required.

The other diagnostics on the experiment use well-established methods of measurement, and problems are not anticipated in obtaining these data.

NUMERICAL MODELING OF HF LASER PERFORMANCE

In the last semiannual report, electron-beam deposition nonuniformity was shown to be an important factor in modeling two HF chemical laser oscillator experiments. When deposition nonuniformity was taken into account, previously noted discrepancies between experiment and prediction were significantly reduced. Most importantly, reasonable results were then obtained by using an F-atom production cost consistent with published values (5 eV).

Comparison has now been extended to an additional pressure regime for one of the above oscillator experiments and to include a third oscillator experiment and two amplifier experiments. Also, a sensitivity study has been carried out to assess the possibility that errors in the various rates explain the remaining discrepancies.

In the last report, it was shown that the observed long tail in the output power pulse

of the Febetron 706 initiated laser can be predicted when deposition nonuniformity is taken into account. The correct prediction of output-energy dependence on oxygen pressure then follows (Fig. 16). Comparison at double the indicated partial pressures has since been completed (Fig. 17). The results show that doubling the pressure does not result in doubling the output energy and, in fact, leads to reduced output at the higher O_2 fractions. The computer model shows that this is a result of the chain terminating reactions which form HO_2 and FO_2, coupled with the relatively weak initiation strength. Had the initiation strength in these experiments been sufficiently strong, the chain terminating reactions would not have been important in the time scale required for the chain reaction, and the reported oxygen effects would not have been seen.

As was reported in the last semiannual report, radial deposition profile measurements, obtained from the λ-geometry laser suggested that deposition nonuniformity must be accounted for in modeling these experiments. This was accomplished by dividing the cylindrical laser medium into concentric regions, each assigned a deposition energy density corresponding to its radial position.
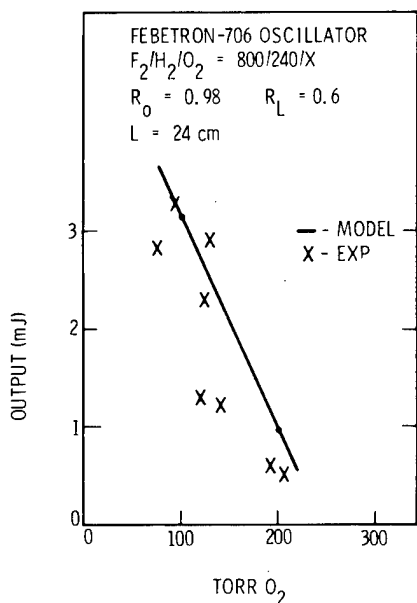
The model predictions for each region were added together with proper volume-based weightings, to obtain "composite solutions." Results were presented for an oscillator case, showing greatly improved agreement with experiment, at a reasonable F-cost of 5 eV.

The composite-solution approach has since been extended to amplifier cases. Figure 18 shows a set of input spectral time histories for a particular case. The amplitude scales are arbitrary in the figure, but measured scale factors were used for the calculation. Figure 19 shows the total input time history and the calculated and measured amplifier power output. The peak power is only mildly overpredicted, while the pulse width is

Fig. 16. Comparison of measured and calculated output energy for the Febetron-706 experiments.
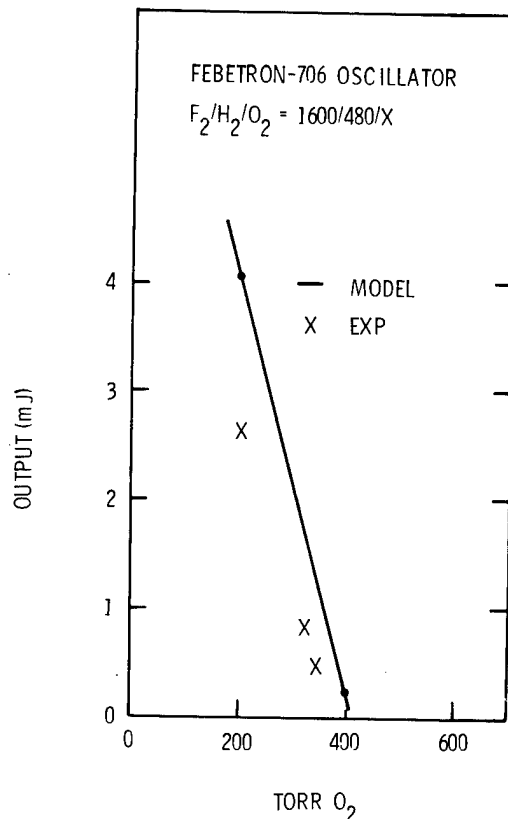
Fig. 17. Comparison of measured and calculated output energy for the Febetron-706 experiments at double the pressure of the previous figure.

overpredicted by about a factor of two, as in the oscillator case. Only moderate ASE suppression is predicted, in agreement with the experiment. The calculations indicate that incomplete suppression is due to spectral and temporal mismatch of the oscillator and amplifier. Figure 20 shows (from another case) the effect of temporal mismatch on ASE suppression for a particular spectral line. The ASE in the absence of an input pulse is seen to persist from about 40 ns to 120 ns after the electron-beam current begins. The $P_1(9)$ input pulse only covers the first half of this period. During that time, the calculation shows very strong ASE suppression, even though the input intensity is less than 100 W/cm^2. As soon as the input cuts off, the $P_1(9)$ ASE rebounds to nearly the unprobed value. Similar results have been observed experimentally, as presented in another section of this report.

Fig. 19. Calculated and measured λ-amplifier response. A three-region composite solution was used.

Fig. 18. Measured input spectral time histories as used in a λ-amplifier experiment. This experiment was chosen for comparison with calculation because a complete set of time histories was available. The amplitude scales of each line are in arbitrary units here, but measured scale factors were used in the code.
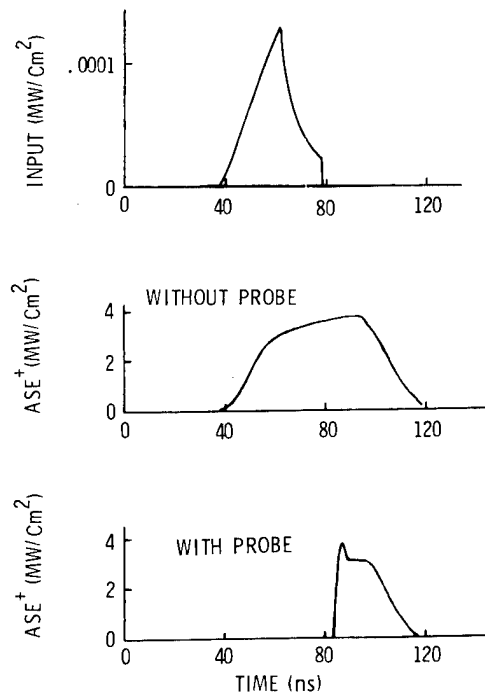
Fig. 20. Calculated effect of temporal mismatch on $P_1(9)$ ASE suppression for the λ-amplifier innermost annulus.

For the Phoenix I laser experiments, less is known about deposition level and uniformity. The two-dimensional Monte-Carlo CYLTRAN suggests significantly lower deposition than in the λ-geometry core but with considerably more uniformity as depicted in Fig. 21. For the transverse excitation, uniform deposition is assumed. Figure 22 shows a comparison of computed and measured oscillator power output. As in the λ-geometry cases, predicted peak power is slightly high, but the main difficulty is pulse-width overprediction. In the calculation, the second peak is caused by FO_2 breakup with increasing temperature. For the Phoenix I amplifier extraction experiments, the λ-geometry oscillator output was used as input to Phoenix I. Since a complete set of spectral time histories was not available, the missing histories were

assumed to be identical to those of nearest-neighbor transitions. The resulting set is shown in Fig. 23. Experimentally determined scale factors for each line were used in the calculations. The predicted output power is compared with experiment in Fig. 24 for the case of an input intensity of 10^7 W/cm^2. In this case, the pulse width is not overpredicted because the input pulse is shorter than the predicted gain pulse width. Finally, in Fig. 25, the calculated and measured results of the energy extraction experiment are shown. Energy extraction is overpredicted for very low input power levels possibly because of parasitic oscillations in the amplifier.

Fig. 21. Result of a two-dimensional Monte-Carlo calculation (CYLTRAN) of electron-beam deposition in the transversely excited oscillator/amplifier.

1-METER CAVITY
$R_0 = .98$ $R_L = 0.06$
$F_2/H_2/O_2 = 800/200/240$ TORR
0.1 J/TORR DEPOSITED IN 2 LITERS; 5 ev/F
$5 \times 7.5 \times 45$ Cm^3 ACTIVE MEDIUM
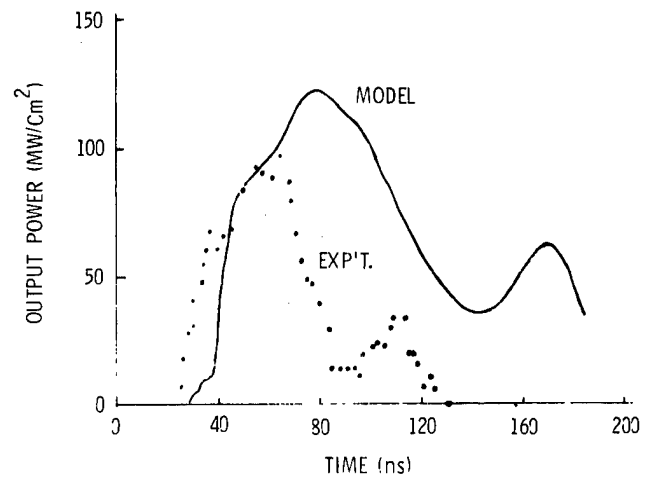
Fig. 22. Comparison of calculated and measured Phoenix I oscillator output-power vs time.
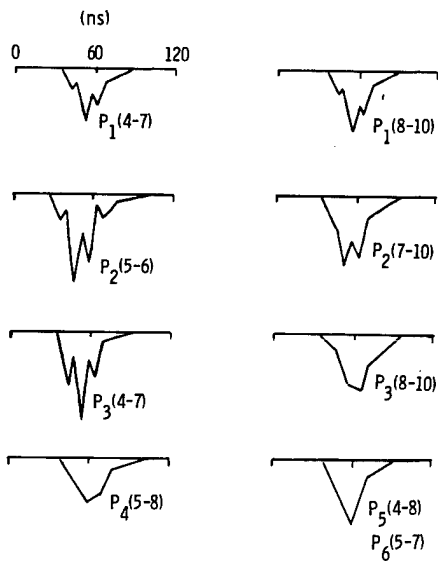
Fig. 23. Measured input spectral time histories used in the λ-oscillator/ Phoenix I amplifier extraction experiments and calculations. As shown, these are approximations to the oscillograms. The amplitude scales here are in arbitrary units; however, the experimentally determined scale factors are used in the calculations.

$F_2/H_2/O_2$ = 800/200/240 TORR

0.1 J/TORR DEPOSITED IN 2 LITERS; 5 ev/F

5 x 7.5 x 45 Cm^3 ACTIVE MEDIUM

10^7 W/Cm^2 PEAK INPUT POWER
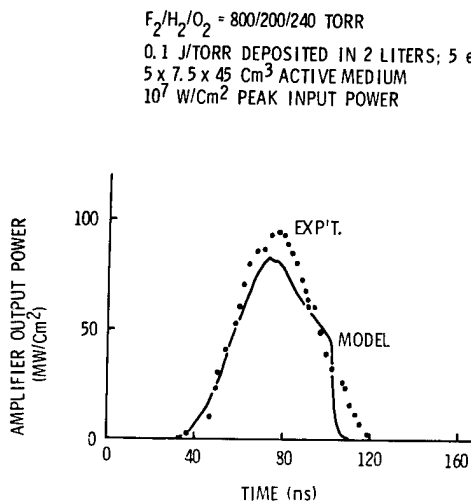
Fig. 24. Comparison of measured and calculated Phoenix I amplifier response.
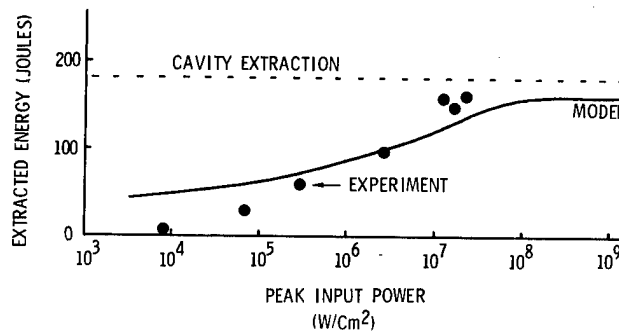
Fig. 25. Calculated and measured Phoenix I amplifier energy extraction as a function of peak input power. Also shown is the measured extraction by an optimized cavity.

Most recently, a sensitivity study has been carried out to assess the effect of the various kinetic rates on the remaining discrepancies between model prediction and experiment. First, the model kinetics were updated. The model prediction for the λ-geometry oscillator case was then shown to be in very good agreement with an equivalent aerospace calculation (Fig. 26). Finally, the λ-geometry oscillator case was recalculated a number of times, each time varying one of the groups of energy-exchange rates by a factor of 3 to 5. The pressure broadening coefficients were increased by a factor of 3 in one case. In was found that only an increase in HF V-T deactivation equivalent to increasing the self-deactivation rate by a factor of 5 would elminate the pulsewidth overprediction. Figures 27 through 29 illustrate this effect. The Phoenix-I amplifier case has not yet been run, but it is expected to be consistent with the other results.

PI OSCILLATOR
COMPOSITE SOLUTION
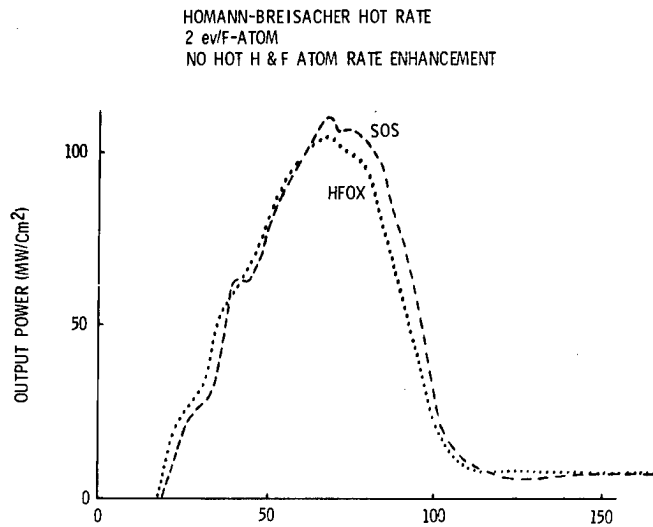
Fig. 26. Demonstration that the Sandia
HFOX and Aerospace SOS calcula-
tions of one-point short-pulse
oscillator output are the same for
same input quantities. Shown is
λ-oscillator output power vs time
for a 400 torr F_2, 100 torr H_2,
120 torr O_2 case.
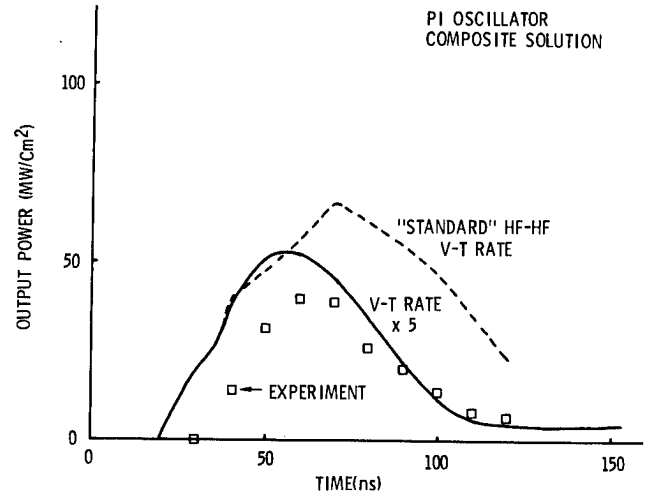
Fig. 27. Improved agreement between λ-
oscillator experiment and compos-
ite calculation when a deactivation
is introduced equivalent to increas-
ing the HF-HF V-T rate by a
factor of 5. Updated hot and
rotational-relaxation rates have
also been used.
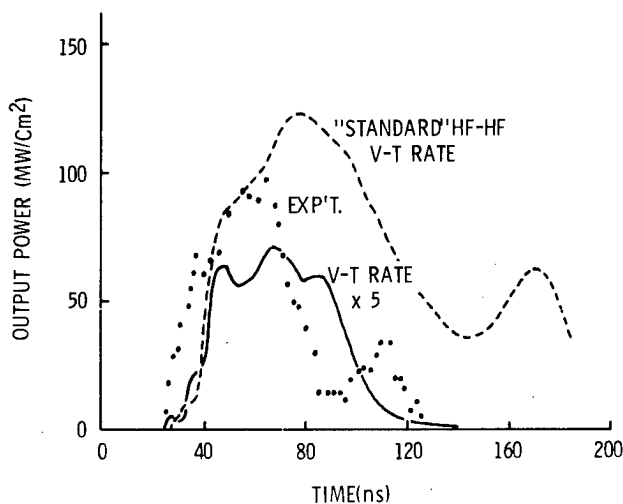
Fig. 28. Improved agreement between trans-
versely excited oscillator experi-
ment and calculation when a deacti-
vation equivalent to increasing the
HF-HF V-T rate by a factor of 5 is
introduced. Updated hot and
rotational-relaxation rates have
also been used.
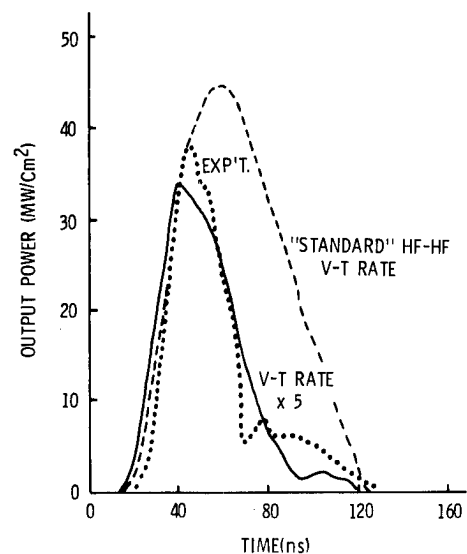
Fig. 29. Improved agreement between λ-
amplifier experiment and compos-
ite calculation when a deactivation
is introduced equivalent to
increasing the HF-HF V-T rate by
a factor of 5. Updated hot and
rotational rates have also been
used.

25

IODINE LASER PROGRAM

OVERVIEW

We now know that an iodine laser system can be built that would satisfy all near-term requirements of laser fusion including the driver of an experimental power reactor, but its efficiency needs to be improved before it can be considered as a driver for a commercial ICF power generator. With available technology, the best electrical efficiency that can be realized for a ~ 1-MJ, 1-to-10-pps iodine laser is 0.4 to 0.5%, and the overall efficiency including regeneration of laser medium starting chemicals is 0.35 to 0.4%. This low-projected efficiency requires very high laser-energy-to-thermonuclear-energy gains for economically attractive electric power generation and its low electrical efficiency would require a prohibitively high capital investment in the pulse power source. Surface discharges and HgXe* exciplexes have been selected as the two most promising advanced pump sources for a more efficient (up to 2%) iodine laser. Both of these sources will be evaluated in near-term studies.

CONTROL OF SELF-FOCUSING IN THE ATOMIC IODINE LASER

The previous semiannual report described the observations of whole beam self-focusing produced within the SAIL-1 main amplifier.[12] The six-level, two-dimensional, time-dependent Maxwell-Bloch code ISTAR[13] predicted the self-focusing with good accuracy and for that reason ISTAR can be used to predict the amount of self-focusing in other iodine laser systems. The magnitude and sign of the saturation-dependent phase shift that leads to the self-focusing beam-propagation instability can be controlled by varying the homogeneous, pressure-produced linewidth.

To explore control of the self-focusing effect, series of ISTAR calculations are presented in Table I and Fig. 30. This series was run with varying linewidth and inversion at fixed gain on the 3-4 line. The incident energy is also varied in the proper manner to maintain a fixed amount of saturation of the 3-4 line. Table I shows that the average R_c (radius of curvature) for the amplified pulse varies regularly with buffer pressure;

TABLE I

ISTAR Calculations Demonstrating Pressure Control of Self-Focusing in a 1-m Amplifier*

E_o (J)	n_U (10^{23} m^{-3})	P_{Ar} (ktorr)	G^{ss}_{3-4} (PRE)	G^{ss} (PRE)	G	R_c (m)
10^{-9}	1.0	1.0	13.8	21.2	17.6	21.83
0.5	1.0	1.0	13.8	21.2	4.0	22.14
1.0	2.0	2.0	13.8	42.4	4.8	21.92
2.0	4.0	4.0	13.8	123.0	6.2	21.51
3.0	6.0	6.0	13.8	248.5	7.0	21.39

*The incident Gaussian pulse has a temporal width of 225 ps (FWHM) and the input amplifier face is 20 m from the minimum waist of 1.32 mm. PRE denotes quantities evaluated from photon rate equations; E_o is input energy, n_U is initial J = 1/2 population, P_{Ar} is broadener pressure, G is gain, and R_c is the average radius of curvature at exit. The first line is included as an undistorted (small-signal-gain) reference case.

the average focusing power of the medium is seen to pass through zero between 2000 torr and 4000 torr of Ar. The radial dependence of R_c for these cases is displayed in Fig. 30; the plotted quantity thus represents a temporal, intensity-weighted averaging over the short pulse. The temporal average represents the maximum pulse aberration that can be corrected with passive optics. The important point is that the amplifiers can be stabilized against self-focusing (although there may be a time-dependent transverse dispersion of the pulse) and should present no problem for further chained amplification as long as the linewidths are kept appropriately large by pressure broadening. In addition, it should be mentioned that the mechanism of self-focusing that is used here seems sufficient to describe all observations. The hypothesis of level-dependent polarizability does not appear necessary.

BEAM RADIUS (cm)
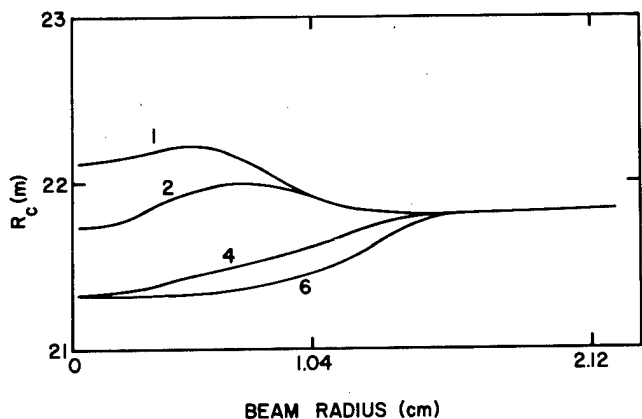
Fig. 30. Theoretical predictions (ISTAR) of the radial variation in the temporally-average radius of curvature, R_c, of a pulse amplified by a 1-m preamplifier. Additional data related to these calculations are contained in Table I. The number by each curve denotes the Ar pressure in ktorr and corresponds to the same case of Table I.

CHEMICAL REGENERATION

As is well known, the usual starting material employed in an iodine laser is a perfluoro-alkyl iodide, RI, some of which is converted to R_2 and I_2 during the operation of the laser.

Economical operation of a large iodine laser system requires that the R_2 and I_2 so formed be regenerated to RI with an energy efficiency of at least a few percent. Previous reports[14,15] have dealt with the amount of R_2 likely to be produced consequent to laser operation and with two schemes for converting I_2 plus the very stable R_2 molecules to RI. Recent experimental results are presented in the following material, and projected chemical efficiency is given as a function of amplifier size.

Laser Induced Chemistry Experiments

Reference 14 discusses experiments in which the formation of CF_3H from mixtures of C_2F_6 and H_2 was studied. The C_2F_6/H_2 system was investigated rather than the C_2F_6/I_2 system because the strong absorption coefficient of CF_3I would have needlessly complicated initial experiments. It was found that the irradiation of C_2F_6/H_2 mixtures with the 9.192-μm R(36) CO_2 laser line at a fluence of 6 J/cm^2 resulted in the formation of CF_3H. It is thought that the laser-induced formation of CF_3H proceeds through the dissociation process

$$C_2F_6 \rightarrow 2\,CF_3 \qquad (4)$$

followed by reaction of CF_3 with hydrogen, as is discussed in detail in Reference 16. The laser energy absorbed per molecule of CF_3H formed was found to be 3.9 eV, a value only about 50% larger than can be explained by dissociation requirements alone.[16] More recently, the formation of CF_3Cl in laser-irradiated C_2F_6/Cl_2 mixtures was studied, and it was found that the absorbed energy per molecule of CF_3Cl formed was 4.3 eV. Within experimental error, the energy requirements for formation of CF_3H and CF_3Cl are the same, as is to be expected if the dissociation of C_2F_6 defines the energy requirement. It is thus reasonable to project an energy requirement of about 4 eV per molecule of CF_3I for regeneration of C_2F_6/I_2 mixtures.

The figure of merit (or "efficiency") of a chemical regeneration process is defined as

$$\eta_R = \frac{\text{extracted laser energy}}{\text{energy input to regeneration process}} \quad (5)$$

and this may be expressed as

$$\eta_R = 0.94\eta_s\varphi/[M\, E_{abs}(eV)] \quad (6)$$

where η_s is the efficiency of the energy source used to induce regeneration, φ is the fraction of its output energy actually utilized, E_{abs} is the absorbed energy per regenerated molecule, and M is the number of RI molecules converted to R_2 per photon extracted from the laser. Values of M for different RI molecules and laser operating conditions are tabulated in Ref. 15, where it is shown that the value of M is 0.96 for a heavily saturated amplifier using 5-torr CF_3I and 3000-torr Argon. A photolytic pump pulse width of 1 μs and 47% photolysis are also assumed. For purposes of illustration, η_s is taken to be 0.2 for the pulsed CO_2 laser[17,18] and φ is taken to be 0.5. The value of η_R corresponding to the 4 eV per molecule required for regeneration of CF_3I is then $\eta_R = 0.025$. Thus, the laser-induced regeneration process does have a figure of merit of at least a few percent, but a better regeneration efficiency would clearly be desireable.

Several possibilities exist for obtaining larger values of η_R as can be seen from Eq (6). A process having a larger value of the product $\eta_s\varphi$ can be sought, and one such is described later in this report. Alternatively, regeneration by using the laser process can be attempted for RI species associated with values of M appreciably less than unity. From Ref. 15, a typical value of M for i-C_3F_7I is, for instance, about 0.1. Accordingly, laser-induced chemistry was studied in n-C_4F_{10} / H_2 and n-C_6F_{14} / H_2 mixtures, as well as in some others. It was found that n-C_4F_{10} dissociates to the stable molecules C_2F_4 and C_2F_6 rather than to the radicals C_2F_5, and that n-C_6F_{14} dissociates in an analogous manner. These facts seem to preclude the use of laser-induced chemistry as a successful regeneration scheme for C_2F_5I or C_3F_7I. It may be the case that CF_3I is the only iodine-laser starting material to which laser-induced regeneration is applicable.

Chemical Regeneration Using Electric Discharge Techniques

The use of electric discharges in chemical recovery of RI compounds from R_2 compounds involves the selective breaking of the R-R bond in a low-pressure gas discharge in such a manner that the resulting R radicals can react with iodine to form the desired RI compound. The basic equipment for this study has been described in the previous semiannual report.[1] Briefly, the system consists of a gas handling system which allows the gas reactants to flow through a tube in which an electric discharge is produced. Down stream from the discharge tube, mass spectrometric analysis equipment allows the quantitative determination of gas products emanating from the discharge region of the flow system. Initial studies described earlier were carried out by using a microwave discharge configuration. Much of the microwave energy was absorbed into the discharge tube rather than within the flowing gas.[1] Thus, the efficiency for producing CF_3 radicals from C_2F_6 was quite low. More recently, the microwave discharge equipment was replaced with an rf discharge system operating at about 13 MHz. Attempts to couple rf energy into the flowing gas have been much more successful.

Initial studies using C_2F_6 showed that CF_3 radicals can be produced in the electric discharge and reacted with Cl_2 to yield CF_3Cl[1]. The current set of measurements has involved the reaction of CF_3 with I_2 to produce CF_3I. However, initial attempts to form CF_3I by using continuous wave (cw), rf discharges resulted in very low product yields. The observed low yields were found to result from the fact that the cw discharge was breaking up the product before it could effuse from the discharge region. In fact, Eujen and Lagow[19] have shown that CF_3I is readily broken up into CF_3 and I with rf discharges. In order to circumvent this problem, a technique involving short, relatively high peak power, rf pulses was utilized. The technique allows selective bond breakage in C_2F_6 to produce CF_3 radicals. The pulses, however, are terminated before

significant amounts of CF_3I are formed. If the time interval between rf pulses is long enough so that the CF_3I formed after each rf pulse can be removed from the discharge region of the flow system before application of the next rf pulse, then the product can be acquired without further breakup. Utilization of the pulsed rf discharge technique has resulted in greatly improved regeneration efficiencies.

The effect of utilizing rf pulses of various time duration where the time between pulses is held at a constant 2 ms is shown in Fig. 31. The data shown in this figure represent a plot of the absorbed rf energy within the discharge, in electron volts, required to form a CF_3I molecule from C_2F_6 and I_2 as a function of rf pulse width. The flow conditions for the data shown are such that about 390 torr cm^3 sec^{-1} of $C_2F_6 + I_2$ was flowing through the discharge tube and the gas pressure at the discharge was 1.2 torr with the iodine content having a mole fraction of about 0.1. The results were not strongly sensitive to the I_2 partial pressure so long as excess I_2 was present in the flow as a lower limit. Concerning an upper limit, best results were obtained if no more than about three times the actual amount of I_2 consumed by the chemical reaction was present in the flow. Examination of the data shown in Fig. 31 reveals that the use of rf pulses as short as 20 μs allows generation of CF_3I with only about 15% of the energy required when the discharge is operated in the CW mode. The data obtained as shown in Fig. 31 were found to be essentially independent of the rf average power used over a wide range in power so long as the peak power level was kept low enough that good rf coupling of the power supply to the discharge tube could be maintained. For a gas pressure of 1.2 torr, peak rf power levels of 5 W to 20 W were utilized. For the cw measurements, average power levels of 2 W to 4 W were used and the absolute product yields obtained were in the same range as those obtained for the case where pulsed rf discharges were used.

The minimum energy required for chemical regeneration, 5.8 eV per CF_3I molecule, was obtained for the case where 20-μs rf pulses were used as shown in Fig. 31. By use of

Eq (6), a value for the figure of merit, η_R, for chemical regeneration of CF_3I from C_2F_6 and I_2 can be obtained. In the present case, a value for the quantity $\eta_S \varphi$ of 0.4 is used. A value for M of 0.96 is used and is appropriate for the case where a laser photolytic pump pulse width of 1 μs is utilized.[15] With the above mentioned values, Eq (6) yields a value of $\eta_R = 0.068$.
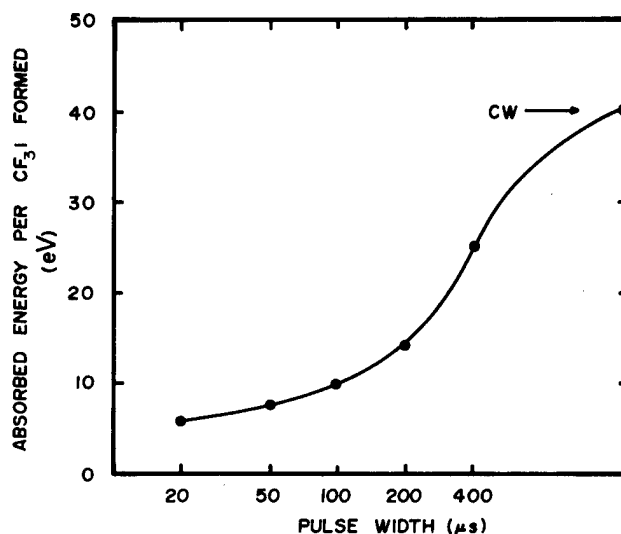
Fig. 31. The rf energy absorbed in the discharge in producing a CF_3I molecule, as a function of rf pulse width. The data apply for the case where the rf pulses occur every 2 ms.

Studies concerning the possible formation of side products using the pulsed rf discharge technique have shown that two such products can form in the discharge along with the desired product, CF_3I. These products are C_2F_4 and C_2F_5I. Both of these products exhibit relatively higher yields with respect to the CF_3I yield as the average rf power level is increased. The effects of increasing the average rf power level upon the relative yields of C_2F_4 and C_2F_5I are shown if Figs. 32 and 33, respectively. It is of interest to note that although the $[C_2F_4]/[CF_3I]$ ratio is relatively low at the 1-W power level, decreasing the power to lower levels apparently would not allow this ratio to approach zero. Examination of data such as those presented in Fig. 33 reveals that under conditions of the present experiments, C_2F_5I
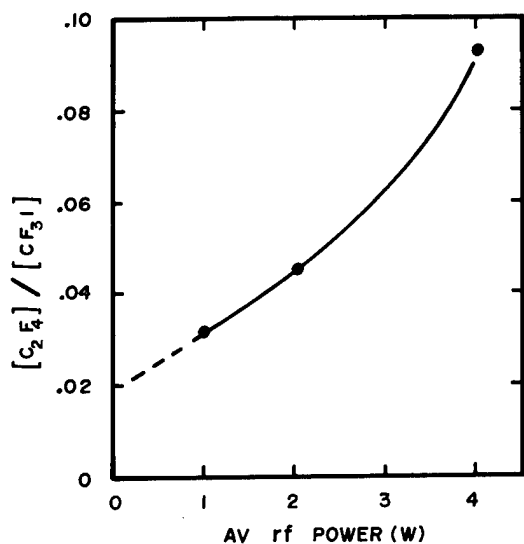
Fig. 32. The relative yield of C_2F_4 with respect to CF_3I as a function of average rf discharge power.

represents the major side product formed in the discharge for average power levels above about 0.25 W. For lower power levels and particularly under the conditions of short rf pulse widths where efficiencies for the production of CF_3I are highest, very low values for the $[C_2F_5I]/[CF_3I]$ ratio can be obtained.

Additional studies have been carried out concerning the regeneration of RI from $R_2 + I_2$ where R_2 is $n-C_4F_{10}$ or $n-C_6F_{14}$. These investigations have shown that nearly random C-C bond breakage occurs when these molecules are passed through the discharge. Thus, there appears to be little selectivity in forming the desired RI compounds. The high-regeneration efficiency, $\eta_R = 0.068$, and good selectivity achieved under optimum rf discharge conditions for production of CF_3I from C_2F_6 and I_2 appear to make CF_3I the best starting material for a photolytically pumped iodine laser.

The results obtained by using the rf regeneration technique are summarized in Fig. 34. Plotted is the chemical regeneration efficiency which can be projected for an iodine amplifier, utilizing CF_3I as a function of

Fig. 33. The relative yield of C_2F_5I with respect to CF_3I as a function of average rf discharge power.
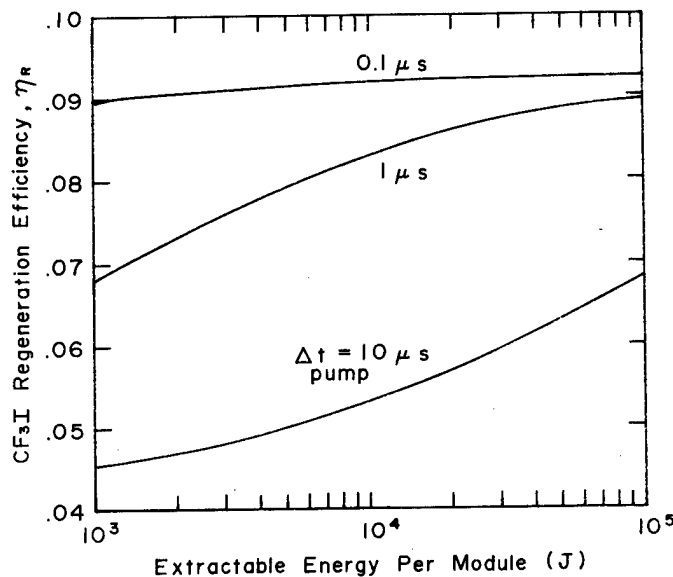
Fig. 34. Chemical regeneration figure of merit for an amplifier utilizing CF_3I, based on rf experimental results.

30

extractable energy. M is implicity dependent upon extractable energy through the scaling laws used to obtain operating conditions as a function of extractable energy per module, as detailed in Ref. 20. The value of η_R depends on photolytic pump pulse width for the reason discussed in Ref. 15. From Fig. 34, it can easily be seen that, even for a pump pulse width of 10 μs, the projected chemical efficiency is much higher than the projected electrical efficiency for large modules. The information summarized in Fig. 34 indicates that the need for chemical regeneration will not be an important barrier to the economical operation of large atomic iodine laser systems.

METAL-DOPED MICROSECOND XENON FLASHLAMPS

The experimental investigation of Te-doped xenon Flashlamps[1] has essentially been completed. It is believed that the behavior of these lamps is now better understood, and that some of the controversy surrounding previous work has been cleared up.

The experimental setup described in Ref. 21 has been modified, and two new pulse-forming networks have been used. The first consists of a 0.70-μF storage capacitor, a 0.16-μH total circuit inductance, a 10-cm arc-length by 4-mm bore flashlamp, and a Tachisto 301 spark gap. The current in this circuit is close to critically damped, and has a width (FWHM) of ~1 μs. The second consists of a 14.2-μF storage capacitor, a 0.18-μH total circuit inductance, a 10-cm arc-length by 8-mm bore flashlamp, and a Tachisto 101 spark gap. The current in this circuit is also close to critically damped, and has a width (FWHM) of ~5 μs. In both circuits, the width (FWHM) of the light output pulse is slightly shorter than that of the current pulse.

Experimental Results

It was very difficult to obtain reproducible results from Te-doped flashlamps when the initial Te powder was vaporized by the main discharge itself. Gusinow[22] observed that reliable results were difficult to obtain in

his experiments until phosphorus was introduced into his vacuum system for study as a dopant. ILC reported that reproducible results with doped lamps were not obtainable in their experiment.[23] Presumably, their vacuum system was quite clean. In the present experiment, the base pressure was 5×10^{-7} torr (the system was not baked out due to the presence of teflon ferrules), and care was taken to avoid contamination by high-vapor pressure materials such as phosphorus. All this suggests that the good metal coatings obtained by Gusinow[24] are probably somehow linked to the presence of phosphorus in his vacuum system.

Another approach was taken to produce good Te coatings. The simmer current used for the main discharge (which, by the way, enhanced the lamp efficiency considerably) was used to heat the lamp with the initial charge of powdered Te. As the lamp heated up, the Te would vaporize and coat the lamp inner wall. The proper choice of current and Xe back pressure for good coating was very unpredictable, and the whole process was essentially done by trial and error. However, once a good Te film was produced (as characterized by a shiny, opaque coating), quite reproducible experimental results were obtainable. The central 2 cm of the 10-cm arc-length was then used for testing and the remaining area was masked off with black paper. All of the data discussed below were obtained in the above manner.

Figure 35 shows the spectral irradiance efficiency (defined as the spectral irradiance at 280±10 nm divided by the capacitor bank energy) for both doped and undoped lamps. The upper and lower dashed lines represent the values for 8-mm-bore and 4-mm-bore doped lamps, respectively. The spectral irradiance for doped lamps coated in the above described manner was practically Xe pressure independent. It is clear that the values for the doped lamps are close to the Xe high-pressure asymptotes. Most probably the Te is vaporized and acts as a high-density plasma and behaves like a high-pressure lamp. This is supported by the observation (see below) that the spectrum from a doped lamp is mostly continuum and shows much less structure than an undoped

lamp, which has several strong Xe and Si lines.

20-torr-Xe lamp. However, the enhancement is quite a bit less as compared to a lamp with 60 torr or more Xe.
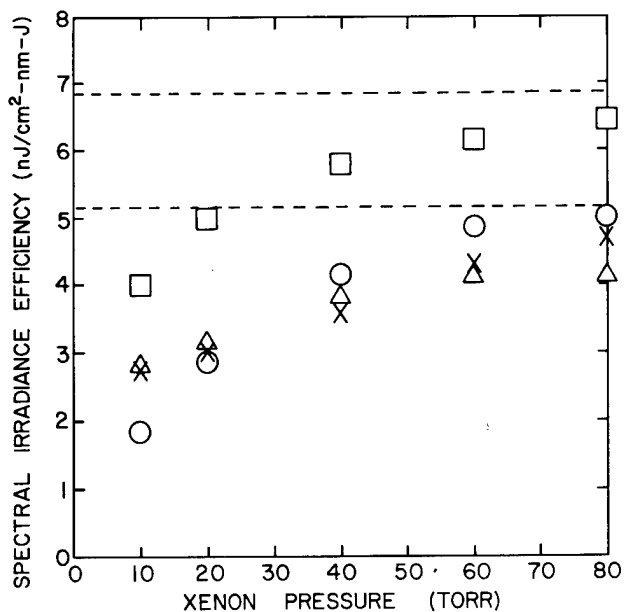
Fig. 35. Spectral irradiance efficiency of Xe flashlamps at 280±10 nm at a distance of 145 cm (19.6° from normal plane): ○-- 4-mm bore, 0.70 μF, 10 kV; X-- 4-mm bore, 0.70 μF, 13.5 kV; △-- 4-mm bore, 0.70 μF, 17 kV; □-- 8-mm bore, 14.2 μF, 5 kV. The lower (upper) dashed line is the value for a Te-doped 4-mm (8 mm) bore flashlamp at all Xe pressures. All but the central 2 cm of the 10-cm arc-length has been masked.
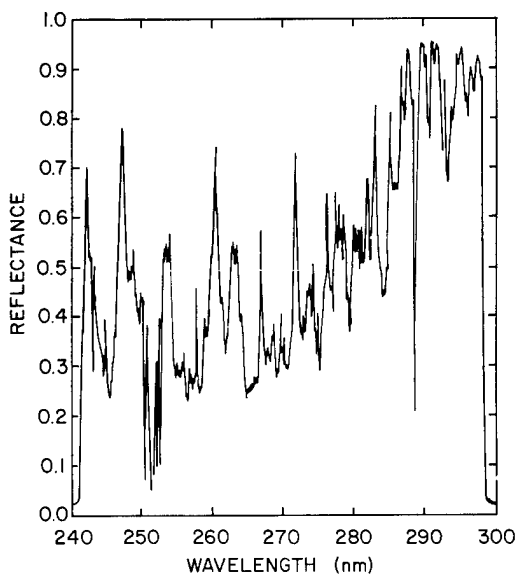
Fig. 36. Reflectance vs wavelength for 8-mm bore, 20-torr-Xe flashlamp. The charge voltage is 5 kV and the capacitance is 14.2 μF. The entrance slit width is 100 μm.

Figure 36 is a spectrum of a 20-torr-Xe flashlamp. The vertical scale is film reflectance, but the film and complete spectrograph system have been absolutely calibrated as a function of wavelength in the region ranging from 250 nm to 300 nm. Figure 37 is a spectrum of a 60-torr-Xe Te-doped lamp. As noted above, a 20-torr-Xe Te-doped lamp has essentially the same spectrum, presumably because the Te plasma is opaque and blocks the Xe emission, as well as being the major source of radiation. It can be seen that, on the average, the spectral irradiance is enhanced appreciably in the region ranging from 250 nm to 300 nm by the addition of Te as compared to a

Fig. 37. Reflectance vs wavelength for 8-mm bore, 60-torr-Xe Te-doped flashlamp. The charge voltage is 5 kV and the capacitance is 14.2 μF The entrance slit width is 100 μm.

Table II summarizes the determined spectral irradiance and net electrical efficiency of several undoped and doped lamps. The spectral irradiance is calculated for a distance of 145 cm normal to the lamp axis and at a wavelength of 280 nm. The efficiency calculated is based on a Lambertian spatial distribution and assumes a flat 400-nm bandwidth. While it appears in Figs. 36 and 37 that the radiation intensity increases towards longer wavelengths, most of this is due to the increased efficiency of the spectrograph optical components, and the actual spectral irradiance is much flatter. The efficiencies must be considered only as approximate, however, since they do not account for the rapidly varying structure in most of the spectra, especially those of the undoped lamps. By comparison, the more precise calculation of the efficiency of an 8-mm bore 20-torr-Xe undoped flashlamp done in Ref. 25 is 0.045 for the same bandwidth and peak current density as the fourth entry in Table II. Reference 25 assumed that the radiation spatial distribution was isotropic, because it was difficult to determine experimentally for the apparatus used. In the present experiment, the spatial distribution was measured up to 45 degrees from the normal to the lamp axis; a Lambertian distribution fit the data appreciably better than an isotropic distribution. Given the experimental uncertainties ($\sim \pm 15\%$ in the present experiment) the agreement is still reasonable, despite the different assumptions for the spatial distribution function.

TABLE II

Flashlamp Spectral Irradiances and Efficiencies

Lamp Size[a] (cm)	Lamp Fill	Energy (J)	Spectral Irradiance[b,d] $J/cm^2 - nm$	Efficiency[c,d]
10 x 0.4	20-torr Xe	63.8	0.19, 0.19	0.024, 0.024
10 x 0.4	60-torr Xe	63.8	0.29, 0.28	0.038, 0.036
10 x 0.4	60-torr Xe +Te	63.8	0.35, 0.32	0.046, 0.041
10 x 0.8	20-torr Xe	177.5	0.94, 1.0	0.044, 0.048
10 x 0.8	60-torr Xe	177.5	1.2 , 1.3	0.054, 0.061
10 x 0.8	60-torr Xe +Te	177.5	1.3 , 1.4	0.060, 0.066

[a] Arc-length x bore.

[b] Calculated for a wavelength of 280 nm and for a distance of 145 cm normal to lamp axis; first number is from photodiode, second is from spectrograph.

[c] A flat 40-nm bandwidth and a Lambertian spatial distribution are assumed; first number is from photodiode, second is from spectrograph.

[d] The ratios of photodiode results to spectrograph results for spectral-irradiance compared to those for efficiency for a given lamp may differ slightly due to numerical roundoff.

The results of the work on Te-doped-Xe flashlamps suggest that while metal additives do enhance the near-uv output radiation the degree of enhancement is such that they do not warrant further investigation at this time with regard to application to the inertial confinement fusion program.

KINETIC PROCESSES IN PHOTOLYTICALLY PRODUCED GROUP VI ^{1}S ATOMS

OVERVIEW

The class of gas-laser systems based on the excitation of the p^4 ^{1}S state of Group VIA atoms (e.g., O, S, Se, Te) with energy extraction on the p^4 ^{1}S $\rightarrow p^4$ ^{1}D or p^4 ^{1}S $\rightarrow p^4$ 3P transition is an extremely promising one for laser-fusion applications. Long energy-storage times are possible since the ^{1}S state exhibits a long radiative lifetime and is resistant to deactivation by a wide variety of other species. Also, these transitions occur at useful wavelengths (459 nm to 790 nm) and exhibit stimulated emission cross sections that are low enough to inhibit parasitic amplified spontaneous emission, but not so low that the medium cannot be saturated at reasonable energy fluences.

Previous work has shown that these excited atomic species can be produced with high quantum yield by the photodissociation of simple, triatomic molecules, e.g., N_2O, OCS, or OCSe. Those studies were performed with weak illumination which produced a small fractional photolysis of the triatomic and low excited $^1S_0$ - atom densities. For these conditions, the quenching of ^{1}S atoms is dominated by two-body collisions with the parent triatomic and/or added diluents. High-intensity photolysis of OCS with 146-nm radiation and OCSe with 172-nm radiation has produced S(^{1}S) and Se(^{1}S) densities near 10^{16} cm^{-3}. However, rapid quenching of both S(^{1}S) and Se(^{1}S) has been observed for these conditions, and electrons, produced initially by photoionization of the excited atoms, have been inferred as the quenching agent. In the remainder of this section, we describe the use of the F_2^* laser to photolytically produce high densities of

S(^{1}S) atoms, our examinations of electron production and the photoionization cross section at 157 nm and the quenching kinetics of S(^{1}S) atoms.

LASER PHOTOLYSIS OF OCS AT 157 nm; S(^{1}S) PRODUCTION, PHOTOIONIZATION, AND LOSS KINETICS

Apparatus

The apparatus used for the present measurements is shown in Fig. 38. An electron-beam pumped molecular fluorine laser which we developed and have described in detail in previous reports[1,5] is used as the photolysis source to dissociate OCS to S(^{1}S) at 157 nm. This laser was vacuum-coupled to a separate cell which contained the OCS to be photolyzed. The laser output was apertured to illuminate uniformly a 1.8-cm^2 area of the OCS-containing cell. A cross-sectional view of this cell is shown in Fig. 39. The laser energy, which could be varied from 1 mJ/cm^2 to 100 mJ/cm^2, was measured by a calibrated Scientech calorimeter mounted on the laser axis at the back of the cell. A 35-GHz, cw, microwave generator provided approximately 5 mW of power through a waveguide on one side of the cell to a detector mounted on the opposite side of the cell at right angles to the F_2^* laser axis. Re-entrant MgF_2 windows on the cell along the microwave axis confined the microwave to pass through the laser-illuminated volume. The volume probed by the microwave was approximately 1.4 cm in diameter and 1 cm in length, centered 1.2 cm from the laser entrance window. An RCA 48362 Photo-multiplier (PMT) was mounted at right angles to both the laser and microwave axis. Apertures in front of the PMT were used to confine its field of view to a small, nearly cylindrical volume, 0.5 cm in diameter by 1.5 cm in length, situated 0.7 cm from the MgF_2 window through which the F_2^* laser entered the cell. Several different interference filters were placed in front of the photomultiplier to isolate radiation from the pressure-induced S(^{1}S $\rightarrow$ ^{1}D) transition near 7727. The photomultiplier was carefully shielded from x-ray and electromagnetic effects associated with firing the electron

beam machine. The effectiveness of this shield was determined by measuring the dynamic response of PMT to a pulsed light source with and without firing the electron-beam machine. The responses of the various PMT/filter combinations were calibrated against the output of a 250-W quartz-iodine standard lamp, which had been calibrated by the Epply Research Laboratories.
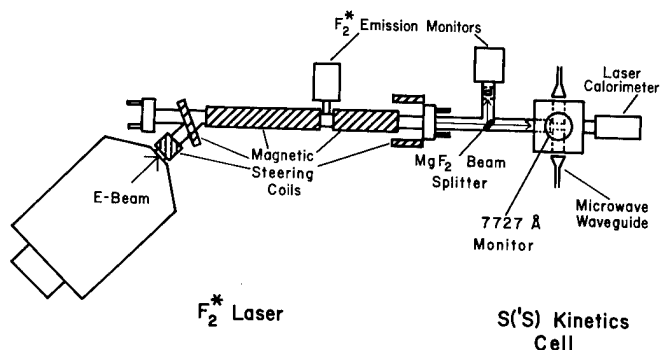
Fig. 38. Schematic diagram of the apparatus for F_2^* laser pumping of $S(^1S)$.
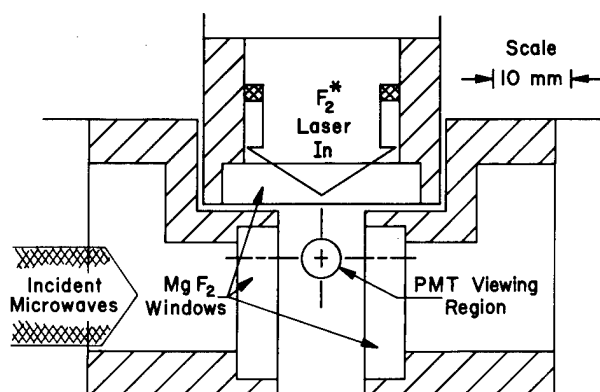
Fig. 39. Scale drawing of the interior of the OCS containing cell.

We obtained the emission spectrum of laser-irradiated mixtures of OCS and added diluents by replacing the microwave detector with a 1/4-m Jarrell Ash spectrometer/PMT combination and recording the intensity of emitted light as a function of wavelength for many sequential shots. This relative spectral sensitivity of this system was determined by measuring its response to the same standard lamps noted above.

Results and Discussion

In the first part of this section we present our data on electron densities vs time in 157-nm photolyzed mixtures of OCS, and OCS with various diluents, demonstrating the manner in which the electron quenching problem can be overcome. As a result of these measurements, we are able to infer an experimental value for the photoionization cross section of $S(^1S)$ by 157-nm light. In the second part of this section, we present our results for time histories of the formation and decay of $S(^1S)$ concentrations in photolyzed mixture during and after the 157-nm photolysis pulse. These data, combined with the electron density measurements, allow us to construct a simple kinetic model of the production and quenching of $S(^1S)$ in these mixtures. In the final part of this section, we present our value for the quantum yield of $S(^1S)$ by 157-nm photons on OCS and, as a necessary adjunct to these measurements, our data on the pressure-induced spectrum of $S(^1S)$ in N_2 and Kr diluents.

The output of the F_2^* laser consists of three narrow lines at 157.6 nm, 157.5 nm, and 156.7 nm, each containing approximately one-third the total energy in a pulse width of about 80 ns. The effective absorption cross section of OCS for the laser radiation was measured by fitting data on low-intensity laser transmission vs OCS pressure to a Beer's law plot and found to be $7\pm0.5 \times 10^{-17}$ cm^2, in good agreement with the literature value.[26] This value of the cross section implies an energy saturation fluence for the dissociating transition of about 18 mJ/cm^2. The transmission of the microwave power through the OCS cell depends parametrically on several variables, including the electron density N_e and the effective electron collision frequency ν. For an idealized slab plasma with sharp boundaries in which coherence effects are ignored, the expected power transmission is given by

$$T = \frac{(1-r)^2 \exp(-2\alpha d)}{1-r^2 \exp(-4\alpha d)} \qquad (7)$$

where

$$r = \frac{(1-\mu)^2 + \chi^2}{(1+\mu)^2 + \chi^2}$$

$$\mu^2 = \frac{1}{2}(1-A) + \frac{1}{2}\left[(1-A)^2 + \left(\frac{\nu A}{\omega}\right)^2\right]^{1/2}$$

$$\chi^2 = -\frac{1}{2}(1-A) + \frac{1}{2}\left[(1-A)^2 + \left(\frac{\nu A}{\omega}\right)^2\right]^{1/2}$$

$$A = \frac{\left(N_e/N_c\right)}{1+(\nu/\omega)^2}$$

and

$$\alpha = \chi\omega/c \ .$$

The quantity d is the slab thickness, ω is the microwave frequency, and N_c is the electron density for which the electron plasma frequency equals the incident microwave frequency. For the present case,

$$N_c = 1.5 \times 10^{13} \ cm^{-3} \ .$$

Equation (7) shows that if the electron collision frequency is small compared to the microwave frequency, the plasma will be opaque for electron densities $N \geq N_c$. However, the addition of diluents, as was done for the present study, insures that the electron collision frequency is of the same order as ω. For those conditions, the plasma is expected to be partially transmitting even for N considerably greater than N_c.

Several examples of the measured microwave transmission vs time are shown in Fig. 40. In each case, the particular gas sample was irradiated with an 80-ns 60-mJ/cm² pulse of 157-nm laser light. This intensity is sufficient to bleach more than 90% of the initial OCS in the volume probed by the

microwaves. It is evident that electron densities greater than 10^{13} cm⁻³ are produced by the photolysis and that the electrons persist for a time that depends on the added diluent.
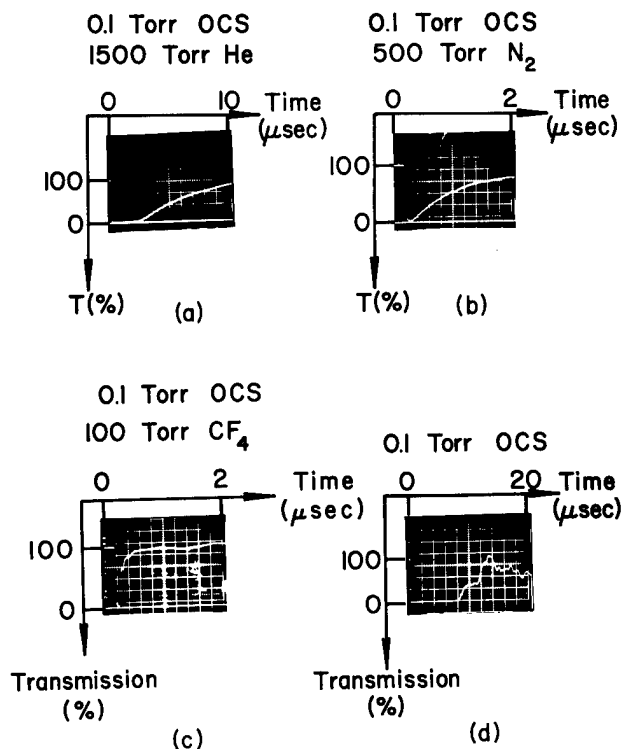
Fig. 40. Microwave transmission vs time following the F_2^* laser pulse for several mixtures. Incident laser energy was 60 mJ/cm² in all cases.

With added diluents such as helium (case (a) in Fig. 40) or nitrogen (case (b) in Fig. 40), the electron density reaches a maximum at the end of the photolysis pulse and decreases slowly thereafter. If an electron attaching gas much as CF_4 (case (c)) or SF_6 is used as a diluent, the microwave transmission, and, therefore, the electron density, tracks the incident laser pulse. This behavior is consistent with the supposition that photoionization of $S(^1S)$ is the primary source of electrons. If no diluent is added to the OCS, the microwave transmission exhibits the erratic behavior of case (d) in which high-electron densities persist for relatively long times. With the aid of Eq (7), data such as those in Fig. 40 (a) or (b) can be unfolded to infer an

electron density vs time behavior. Such inferences are most meaningful for cases in which several hundred torr of a molecular gas such as N_2 is added to relatively low OCS concentrations and for times following the end of the incident laser pulse. A N_2 buffer insures rapid cooling of the initially produced 0.26-eV photoelectrons, and the electron collision frequency with N_2 is well known. With added nitrogen, the electron density derived via Eq (7) from the measured microwave transmissions exhibits a time dependence, following the laser pulse, of the form

$$\frac{1}{N_e} = \frac{1}{N_o} + \beta t$$

that is characteristic of simple electron-ion recombination. The constant β depends on the pressure of added nitrogen, increasing by about an order of magnitude as N_2 pressure increases from 259 torr to 1500 torr. The value of N_o, the electron density remaining at the end of the laser pulse, is proportional to the incident laser flux. For case (b) of Fig. 40 the peak electron density is calculated to be about 2×10^{13} cm^{-3}.

These data of microwave transmission through photolyzed mixtures of OCS and N_2 can also be used to estimate the value of the photoionization cross section of S(^{1}S) at 157 nm. The analysis, which is complicated by the fact that the incident 157-nm radiation first produces S(^{1}S) and then photoionizes it under conditions for which the dissociating transition is partially bleached, proceeds as follows.

Since the laser energy is much higher than the level required to bleach the medium, a first order estimate of the photoionization cross section can be obtained by assuming that all of the OCS has been converted to S(^{1}S) at time zero and that all 60 mJ/cm^2 of the laser beam is available to photoionize the S(^{1}S). The number of photoelectrons produced (N_e) is then;

$$N_e = N_o (1 - e^{-\sigma_i I})$$

where

N_o = initial S(^{1}S) density

σ_i = photoionization cross section

I = laser fluence/cm^2

This approximation yields a value of 1.2×10^{-19} cm^2 for the photoionization cross section.

A more careful approach utilizes the radiative transport equation of the 157 nm laser light in the OCS medium

$$\frac{\partial I}{\partial x}(x, t) + \frac{1}{c}\frac{\partial I}{\partial t}(x, t) =$$

$$- \sigma_d I(x, t)\rho(x, t) = \frac{\partial \rho}{\partial t}(x, t) \qquad (8)$$

in which I is the laser intensity, ρ is the OCS density, and σ_d is the cross section for dissociating OCS. We assume that photoionization has a negligible effect on the radiation transport, i.e., the photoionization cross section is assumed to be much smaller than σ_d. (As shown below, this assumption is quite reasonable.) Equation (8) can be solved exactly to give

$$I(x, t) = \frac{I_o(t-x/c) \exp\left[\sigma_d \int_{-\infty}^{t-x/c} du\, I_o(u)\right]}{U}$$

$$\rho(x, t) = \frac{\rho_o(x) \exp\left[\sigma_d \int_{-\infty}^{x} du\, \rho_o(u)\right]}{U}$$

$$U = \exp\left[\sigma_d \int_{-\infty}^{t-x/c} du\, I_o(u)\right]$$

$$+ \exp\left[\sigma_d \int_{-\infty}^{x} du\, \rho_o(u)\right] - 1$$

where I_o is the input laser pulse intensity at $x = 0$ and ρ_o is the density distribution of OCS at $t = 0$.

The density of electrons N_e produced by photoionization of $S(^1S)$ is given by

$$\frac{\partial N_e(x,t)}{\partial t} = \sigma_i I(x,t)\rho^*(x,t)$$

$$- [\text{electron loss rate}] \qquad (9)$$

where σ_i is the photoionization cross section and ρ^* is the $S(^1S)$ density. In terms of the OCS density,

$$\rho^*(x,t) = \varphi^*\left[\rho_o(x) - \rho(x,t)\right]$$

where φ^* is the quantum yield for $S(^1S)$ production. The relationship between the electron density at any position x and the photoionization cross section is obtained by integrating Eq (9) in time.

Examination of Fig. 40 (b) shows the photoelectrons are produced on a time scale that is short compared to the electron-ion recombination time. Therefore, the maximum electron density occurs near the end of the laser pulse and is not reduced very much by recombination during the pulse. For this reason, we can neglect the electron-loss term in Eq (9), and obtain the maximum electron density by integrating Eq (9) in time to the end of the laser pulse. The result is

$$N_e(x) = \frac{\sigma_i \varphi \rho_o}{\sigma_d}\left\{ \ell n\left[V/\exp(\sigma_d \rho_o x)\right] \right.$$

$$\left. + \left[1 - \exp(\sigma_d E_o/h\nu)\right]/V \right\}$$

$$V = \exp(\sigma_d E_o/h\nu) + \exp(\sigma_d \rho_o x) - 1 \qquad (10)$$

where E_o is the incident laser flux and $h\nu$ is the photon energy. In deriving Eq (10), we assumed a temporally rectangular laser pulse and a uniform initial density of OCS. For an input fluence of 60 mJ/cm^2 and an OCS pressure of 0.1 torr, we infer a peak electron density of $2\pm1 \times 10^{13}$ cm^{-3} from our microwave transmission data at a variety of added N_2 pressures between 250 torr and 1500 torr. The microwave probe is centered at $x = 1.2$ cm. As will be shown later, $\varphi^* \approx 0.85$. Substitution of these values in Eq. (10) implies a photoionization cross section of

$$\sigma_i \cong 2.3 \times 10^{-19} \text{ cm}^2 .$$

We believe this value, which represents an average over the three lines in the laser spectrum, to be accurate to within a factor of 2, based primarily on the uncertainty in the derived electron density.

There are no other experimental determinations of σ_i and only two theoretical ones with which we can compare our result. McGuire has performed calculations of the photoionization cross sections for the ^1S states of all the Group VI atoms via excitation to autoionizing levels. Both configuration and spin-orbit interaction were included, and the term energies were adjusted to agree with experimental values. Near 157 nm, McGuire's calculated cross sections are sharply peaked with a value of 4×10^{-18} cm^2 at 157.5 nm, falling to 1.5×10^{-18} cm^2 at 157.6 nm and

$< 10^{-19}$ cm^2 at 156.7 nm. His predicted value, averaged over the three laser lines, is 1.8×10^{-18} cm^2, about an order of magnitude larger than our measured value.

A second major effort of the present experiment was to monitor the S(^{1}S) density as a function of time during and after the photodissociating laser pulse in coincidence with the microwave transmission measurements. Radiation from the S(^{1}S $\rightarrow$ ^{1}D) transition near 773 nm was used as a direct indicator of the S(^{1}S) density.

Figure 41 contains three examples of the various time dependent signals we observed during and immediately following the incident 157-nm laser pulse. The circles were obtained with a mixture of 1-torr OCS and 1500-torr Kr at a low incident fluence of 3.2 mJ/cm^2. No detectable electrons are produced in this use, and, indeed, Eq (10) predicts an $N_e \approx 10^{10}$ cm^{-3}. The S(^{1}S) density rises to a peak in about 100 ns, which is consistent with the time scale for passage of the laser pulse through the region viewed by the photomultiplier. As the laser fluence is increased to the value for saturation and beyond, the S(^{1}S) density rises to its peak value before the entire laser pulse passes through the viewing region, and significant numbers of photoelectrons are detected by the microwave probe. The signal denoted by X's is a mixture of 1-torr OCS and 1500-torr N$_2$ irradiated with 45 mJ/cm^2 of 157-nm radiation. The microwave transmission shows electron densities $> 1.5 \times 10^{13}$ cm^{-3} (total absorption) persisting for about 150 ns following the start of the laser pulse. The PMT signal in Fig. 41 shows that considerable quenching of the S(^{1}S) density occurred during that time of high-electron density and that the quenching rate decreases markedly at later times for which the microwave transmission indicated considerably fewer electrons ($\approx 10^{12}$ cm^{-3}). The presumption is that the rapid quenching is due to electrons. However, the rate constant for electron quenching of S(^{1}S) is estimated to be about 10^{-8} cm^3 s^{-1}, which requires an electron density of about 10^{15} cm^{-3} to account for the quenching we observe. Equation (10) predicts electron densities from direct photoionization of only 5×10^{13} cm^{-3}. It may be

that under these particular conditions, electron multiplication and loss of S(^{1}S) is occurring through superelastic heating of the electrons, and subsequent ionization of S(^{1}S).
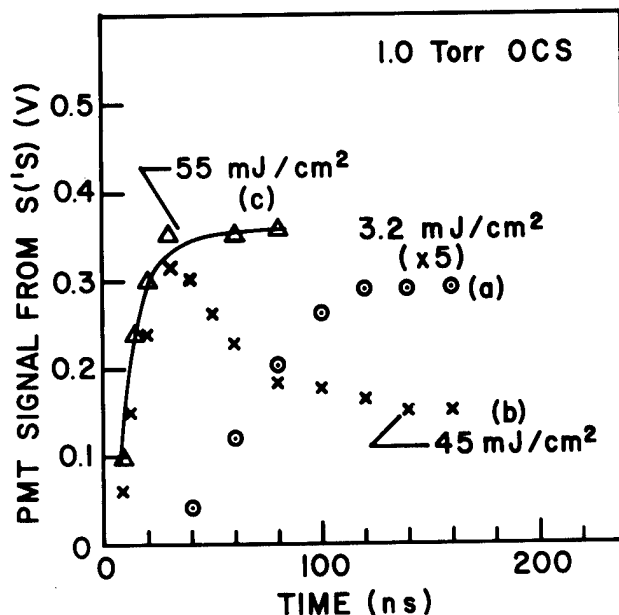
Fig. 41. Photomultiplier signal near 773 nm vs time following the start of the F$_2^*$ laser pulse. The conditions are as follows: curve a: 1-torr OCS, 1500-torr Kr at an incident laser fluence of 3.2 mJ/cm^2; curve b: 1-torr OCS, 1500-torr N$_2$ at 45 mJ/cm^2; curve c: 1-torr OCS, 200-torr CF$_4$, 1300-torr N$_2$ at 55 mJ/cm^2.

The final set of data in Fig. 41, the triangles, show the effect on the time dependence of the S(^{1}S) density when a mixture of 1.0-torr OCS, 200-torr CF$_4$, and 1300-torr N$_2$ is irradiated with 55 mJ/cm^2 of 157-nm light. Again, the S(^{1}S) density rises to its peak in a time that is short compared to the duration of the laser pulse. The expected rise time of the S(^{1}S) density is determined by the propagation of the bleaching wave through the region viewed by the PMT. From Eq (8), this rise time is given approximately by $t_r = 1/I_0\sigma_d$ or ≈ 25 ns in the present case, which agrees quite well with the measured rise time of Fig. 41. The more significant feature of these data is that the addition of CF$_4$ has eliminated the rapid quenching that is

evident when N_2 alone is used. The trans-mitted microwave signal for this case appears very similar to that of Fig. 40c; that is, electron densities $\geq 1.5 \times 10^{13}$ cm^{-3} are observed only during the laser pulse with a rapid decrease to lower values at the termination of the pulse.

Figure 42 contains the late-time behavior of the $S(^1S)$ density for nearly the same conditions depicted in Fig. 41. For low-incident laser fluence, the quenching of $S(^1S)$ is quite slow; curve (a) exhibits an electron-folding time of 9 μs.
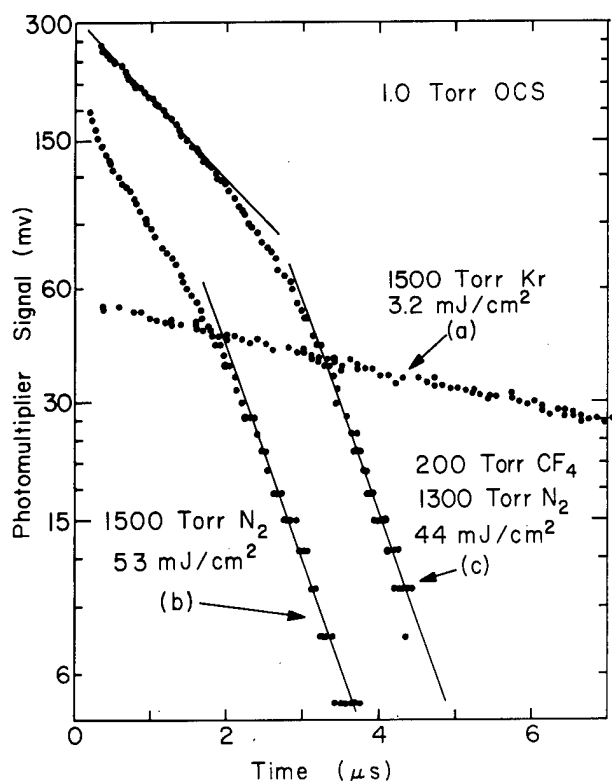
Fig. 42. Same as Fig. 41 except for the indicated incident fluences.

As the incident fluence level is increased, the peak $S(^1S)$ density increases as expected, but the quenching rate increases also. If CF_4 is added to control the electron quench-ing (curve (c)), then we observe an initial slow decay followed by a faster one at later times. Back extrapolation of the slow decay to t = 0 gives the same peak signal as is observed for data taken on the early time

scale of Fig. 41. If the photoelectrons are not controlled, (curve (b)), the quenching of $S(^1S)$ is more rapid than case (c) during the early part of the decay, but the quenching rates for cases (b) and (c) are nearly the same at late times.

A series of decay curves similar to case (c) above, in which electron quenching of the $S(^1S)$ is not important, were obtained at a variety of incident fluence levels and OCS densities. In each case, the curves were analyzed in terms of an early and late time decay frequency. Figure 43 contains a plot of these decay frequencies vs the amount of OCS dissociated by the incident 157-nm laser pulse in the volume viewed by the photo-multiplier. The initial $S(^1S)$ density is directly proportional to the amount of OCS photolyzed. Within the scatter in the data, both decay frequencies increase linearly with increasing photolysis, regardless of the initial OCS pressure or incident fluence level. That is, high-fluence shots into low-OCS concentrations and low-fluence shots into high-OCS concentrations which give the same photolyzed amount also exhibit the same early and late time decay frequencies. The observed linearity of the early-time decay frequency with increasing initial $S(^1S)$ density is evidence that self-quenching of $S(^1S)$ is not important, at least for densities $\approx 3 \times 10^{16}$ cm^{-3}.
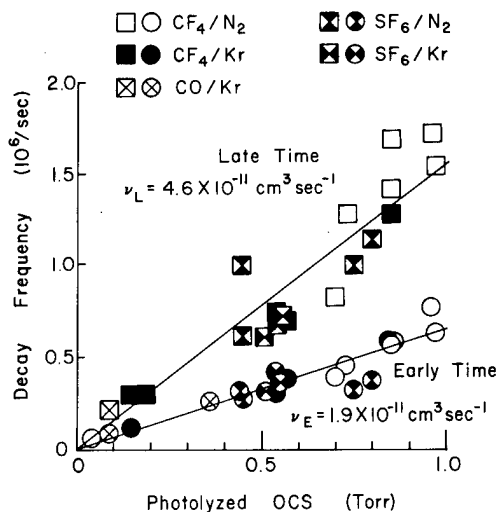
Fig. 43. Decay frequency of the $S(^1S)$ density vs the fraction of OCS phototyped.

The behavior of the S(^{1}S) density with time exemplified by the data contained in Figs. 41 and 42 can be explained with the aid of a simple kinetic model. For OCS dissociation by 157-nm photons, there are three energetically allowed channels leading to different electronic states of the sulfur atom and a fourth channel leading to CS formation:

$$OCS + h\nu \ (157 \ nm) \xrightarrow{\ \varphi^*\ } CO + S(^1S)$$

$$\xrightarrow{\ \varphi_d\ } CO + S(^1D)$$

$$\xrightarrow{\ \varphi_p\ } CO + S(^3P)$$

$$\xrightarrow{\ \varphi_m\ } CS + O(^3P)$$
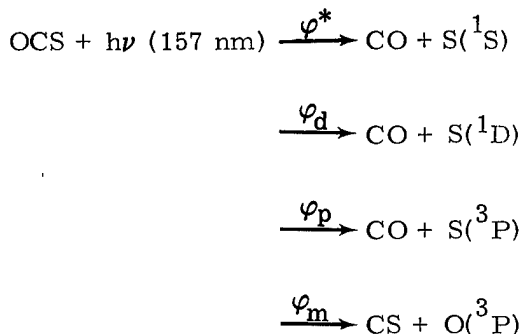
Each channel is labeled with its respective quantum yield; the latter two dissociation channels are spin-forbidden.

Following the laser pulse, any or all of the above species, in addition to the parent compound, added diluents, and electrons can possibly influence the quenching of S(^{1}S). However, the data in Fig. 43 indicate that the major influence must be by species produced in direct proportion to the amount of OCS photolyzed. At any time following the laser pulse, when CF_4 or SF_6 is included as a diluent, deactivation by electrons does not appear to be important, at least for incident fluence levels ≤ 100 mJ/cm^2 and S(^{1}S) densities $\leq 3 \times 10^{16}$ cm^{-3}. Another potential quencher, S(^{1}D), is itself deactivated to S(^{3}P) by the added diluents so quickly under our conditions that it, too, can be neglected. The quenching of S(^{1}S) by CO has been measured previously and is negligibly small for the conditions of Fig. 43. The species that are most likely to be responsible for the observed decay rates are S(^{3}P), CS, and O(^{3}P). The association rates for removing these atomic and radical species are too slow to appreciably affect their concentrations during the lifetime of S(^{1}S). Thus, at early times following the laser pulse, the S(^{1}S) decay frequency can be represented by

$$\nu_E = \left[k_p(\varphi_d + \varphi_p) + (k_m + k_m')\varphi_m \right] f \ [OCS]_o$$

where f is the fraction of the initially present OCS, $[OCS]_o$, dissociated, k_p is the rate constant for S(^{1}S) quenching by S(^{3}P), and k_m and k_m' are the rate constants for deactivation by CS and O(^{3}P), respectively. As time progresses, the S(^{1}S) is quenched to S(^{3}P), which in turn accelerates the quenching of S(^{1}S), leading to the rollover in the measured decay curve. At late times, for which little S(^{1}S) remains, the decay frequency is expected to reach a constant value given by

$$\nu_L = k_p \varphi^* f[OCS]_o + \nu_E \ .$$

From the data in Fig. 43, we obtain directly that

$$\varphi^* k_p = 2.7 \times 10^{-11} \ cm^3 \ s^{-1}$$

and

$$\varphi_m (k_m + k_m') =$$

$$1.9 \times 10^{-11} \left\{ 1 + 1.5 \ \frac{(\varphi_d + \varphi_p)}{\varphi^*} \right\} cm^3 \ s^{-1}.$$

From the quantum-yield data to be presented later, $\varphi^* \sim 0.8$ so that

$$k_p \approx 3 \times 10^{-11} \ cm^3 \ s^{-1}$$

This value of the rate constant for S(^{3}P) quenching of S(^{1}S) can be compared to the analogous rate constant for O(^{3}P) quenching of O(^{1}S) measured by Slanger and Black[27] of 1.8×10^{-11} cm^3 s^{-1}.

Since φ^* is approximately 0.8, then $(\varphi_m + \varphi_d + \varphi_p) \approx 0.2$ and

$$k_m + k_m' \approx \frac{2 \times 10^{-11}}{\varphi_m} \text{ cm}^3 \text{ s}^{-1} .$$

If φ_m were about 0.1, then our present data would be consistent with $k_m + k_m' \approx 2 \times 10^{-10}$ cm^3 s^{-1}, a value that is not unreasonably large.

Curve (b) of Fig. 42 can also be interpreted in terms of this kinetic model. During very early times following the laser pulse (100 ns to 200 ns), the electrons quench approximately half of the S(^{1}S) to S(^{3}P) before they themselves are removed by recombination (see Fig. 41b). Thus, the early decay shown in Fig. 42b is faster than that of Fig. 41b because of the added S(^{3}P) density at early time. Both curves exhibit nearly the same late-time decay, as expected, since they correspond to nearly the same dissociation fraction of the initial OCS.

A final goal of the present study was to measure the effective quantum yield of S(^{1}S) from OCS at 157 nm under a variety of conditions. For our experimental conditions, the effective quantum yield is given by the expression

$$\varphi^* = \frac{7.8 \times 10^{16} \, V_{PMT}}{R_{PMT} \, V\Omega \, A_{eff} \Gamma f [OCS]} .$$

Where V_{PMT} is the peak voltage attributed to S(^{1}S $\rightarrow$ ^{1}D) radiation, R_{PMT} is the calibrated response of the PMT at 773 nm, V is the volume from which S(^{1}S $\rightarrow$ ^{1}D) radiation is detected, Ω is the solid angle subtended by the detection system, A_{eff} is the effective pressure-induced spontaneous emission coefficient, and Γ is the fraction of S(^{1}S $\rightarrow$ ^{1}D) radiation transmitted to the PMT by our optical filter arrangements.

The value of A_{eff} with a N$_2$ diluent has been measured by previously.[28] By comparing the S(^{1}S $\rightarrow$ ^{1}D) emission intensity with added CF$_4$ to that with pure N$_2$, we determined that A_{eff} for CF$_4$ is the same as that for N$_2$, to within our experimental accuracy ($\pm$10%). Similarly, we determined that CO is 0.8 times as effective as N$_2$ in pressure-inducing ^{1}S $\rightarrow$ ^{1}D emission. The quantity Γ is the overlap integral between our filters and the pressure-induced emission spectrum of S(^{1}S)

$$\Gamma = \frac{\int_o^\infty \epsilon(\lambda) T(\lambda) \, d\lambda}{\int_o^\infty \epsilon(\lambda) \, d\lambda}$$

where $\epsilon(\lambda)$ is the pressure-induced ^{1}S $\rightarrow$ ^{1}D emission intensity as a function of wavelength and $T(\lambda)$ is the transmission function of the particular optical filter arrangement. We determined $\epsilon(\lambda)$ for the case in which CF$_4$ and N$_2$ were added as diluents. The resulting emission spectrum is shown in Fig. 44. Figure 45 contains the emission spectrum if Kr is used as diluent in place of N$_2$. We used three different optical filter combinations for $T(\lambda)$ which overlapped from 20 to 63% of the emission spectrum shown in Fig. 44.
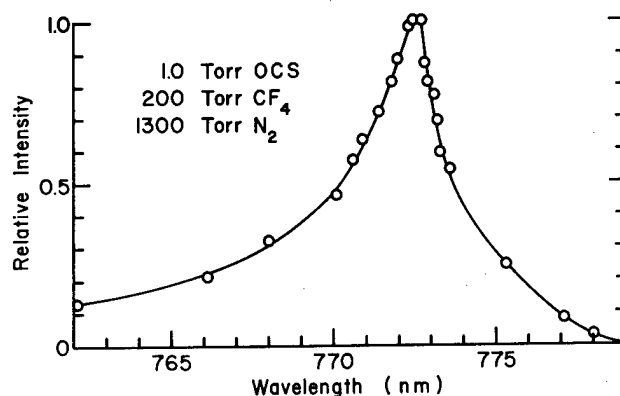
Fig. 44. Collision-induced emission near 773 nm from S(^{1}S)/N$_2$.
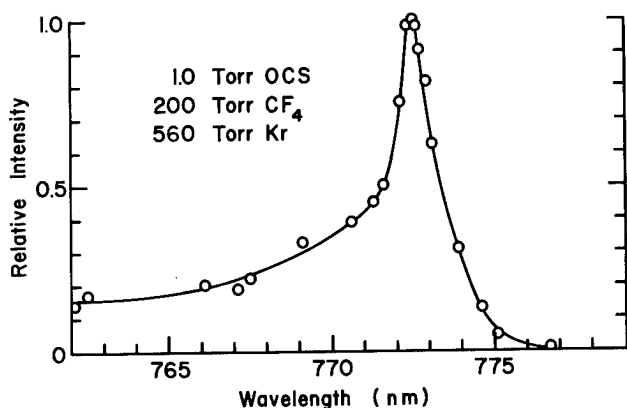
Fig. 45. Collision-induced emission near 773 nm from S(^{1}S)/Kr.

Table III contains the results of our determination of φ^* for several different conditions of incident fluence and added diluents.

Within the scatter of these data, all of these various conditions exhibit the same high effective quantum yield. In addition, the average value is in good agreement with the value measured by Black, Sharpless, and Slanger.

Conclusions

We have shown that S(^{1}S) is produced with high efficiency by photolysis of OCS by 157-nm laser light at laser intensities up to 0.1 J/cm^2 and S(^{1}S) densities up to $\sim 3 \times 10^{16}$ cm^{-3}. An experimental value for the photoionization cross section of S(^{1}S) by 157-nm light of 2.3×10^{-19} cm^2 has been obtained. We have also shown that photoionization produced electrons and that electron runaway processes can be controlled by the addition of proper electron cooling

TABLE III

Quantum Yields of S(^{1}S) at 157 nm

OCS (torr)	N$_2$ (torr)	Added Gas (torr)		E$_0$ (mJ/cm^2)	φ^*
1.0	620	200	CF$_4$	32	0.85
1.0	620	200	CF$_4$	52	0.88
1.0	1340	200	CF$_4$	55	0.71
1.0	620	400	CO	38	0.80
1.0	620	400	CO	57	0.77
1.0	1500			45	0.85
1.0	980			36	0.94
0.6	1500			3.2	0.71
0.5	760			35	0.90
0.5	760			95	0.88
0.5	760			106	0.89

Note: Average $\varphi^* = 0.83 \pm 0.08$

(N_2, CO) and electron attaching (CF_4, SF_6) diluents. We have examined the kinetics of quenching of the $S(^1S)$ populations in cases in which quenching by electrons is not important. Finally, we have demonstrated that $S(^1S)$ densities of $\sim 3 \times 10^{16}$ cm^{-3} can be efficiently produced and stored for times on the order of a microsecond. These production efficiencies and storage times are consistent with the possible use of the $S(^1S) \rightarrow S(^1D)$ transition as an efficient, high-energy storage.

Xe_2^* DRIVER FOR $Se(^1S)$ KINETICS STUDIES

One area of recent interest in the Group VI program has been the development of small, short pulse (< 100 ns) Xe_2^* driver for use in OCSe kinetics experiments. Currently, the Xe_2^* driver is excited by a Febetron 705 pulser (1.7 MeV, 80 ns, $\sim$ 300 J) with the laser resonator contained in a "lambda geometry" cell. In order to work at the high-Xenon pressures (3,000 torr) necessary for efficient Xe_2^* lasing, it was necessary to add a re-entrant window holder for the 75-μ thick titanium electron beam foil (Fig. 46). The re-entrant window holder reduces the length of high-pressure gas traversed by the electron beam before reaching the gas in the resonator cavity from 10.5 cm to 2.5 cm. Preliminary experiments with this apparatus have demonstrated that this system can generate Xe_2^* laser pulses at 1720 Å with pulsewidths on the order of 50 ns and energy densities of at least 30 mJ/cm^2. Further parameterization and optimization of the system are in progress.

PHOTOIONIZATION OF THE GROUP VI $(ns)^2(np)^4$ ^1S_O TERM VIA EXCITATION OF AUTOIONIZING LEVELS

At wavelengths of interest for photodissociating OCS and OCSe with near unity yield of $S(^1S_O)$ and $Se(^1S_O)$, the cross section for direct photoionization of the ^1S_O term is small ($\leq 10^{-20}$ cm^2). However, indirect photoionization (photoexcitation followed by autoionization) could be significant if the transitions are in the photodissociation pumpband, if the linewidth were large, and if the
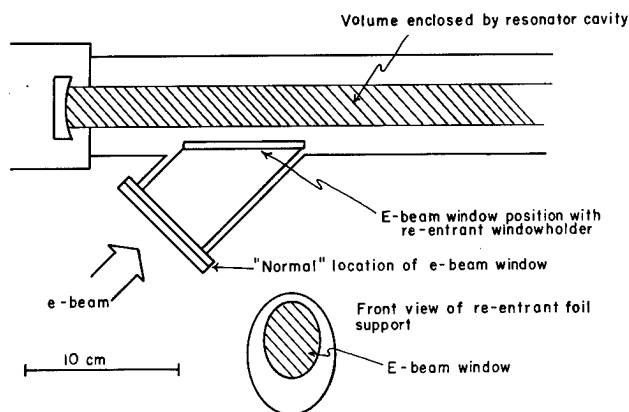
Fig. 46. Xe_2^* driver cell showing re-entrant electron-beam foil holder.

oscillator strength resulted in an effective photoionization cross section $> 10^{-19}$ cm^2. To examine this possibility we have diagonalized a 67 x 67 interaction matrix for 67 odd parity levels with J = 1. The matrix includes both configuration interaction and spin-orbit interaction. Details on the calculation of the matrix elements are given in the previous semiannual report.[1] The interaction matrix contains both bound and autoionizing levels, and, where possible, spectroscopic parameters are chosen to bring the calculated energy of bound state levels into agreement with experimental measurements. These spectroscopic parameters are used to locate autoionizing levels.

In Tables IV, V, and VI, we list the energies of the various odd parity levels with J = 1 for S, Se, and Te. In these Tables, column 1 numbers the levels, roughly in order of increasing energy, measured in cm^{-1} relative to the ground state level of the ion; column 2 lists the designation of the levels in LS coupling; column 3 (K_i) lists the diagonal entry in the interaction matrix; and column 4 (K_f) lists the eigenvalue resulting from the matrix diagonalization (the shift between columns 3 and 4 is the result of configuration and spin-orbit interaction). Column 5 is the experimental energy level from Moore's tables.[29] For S the entries in parentheses are measurements on autoionizing levels by Tondello,[30] while for Te the entries in parentheses are tentative identifications by Bartelt.[31] For S, column 6 lists

the energy levels in a close-coupling calculation of Conneely, Smith, and Lipsky.[32] The remaining two columns list the calculated autoionizing level widths and oscillator strengths from $(ns)^2(np)^4\ {}^1S_O$. For S, there are additional columns listing level widths measured by Tondello[30] and calculated by Conneely, Smith, and Lipsky.[32]

In Figs. 47, 48, and 49 the calculated indirect photoionization cross sections are shown for S, Se, and Te, respectively. For Te, the calculated cross section is large with few windows. For Se, the calculations indicate a window ($\sigma < 1 \times 10^{-19}\ cm^2$) at 1725 Å, where Xe_2^* can be used as a photodissociation pump. For S, the calculations indicate a cross section of $10 \times 10^{-19}\ cm^2$

at 1575 Å (the wavelength of the F_2^* laser) and $\approx 6 \times 10^{-19}\ cm^2$ at 1460 Å (the wavelength of the Kr_2^* laser. The dotted curve in Fig. 47 near 1460 Å is the result of "fine tuning" (varying K_i) the calculation to reproduce Tondello's measurements.

The calculations are sensitive to the choice of K_i values. The results reported here are semiempirical in that we have used spectroscopic parameters chosen to reproduce the observed energies of bound levels. Currently, we are examining the possibility of ab initio calculations. They require the inclusion of additional configuration interaction effects from the $(ns)^1(np)^4(n'p)$ configurations with n' > n.
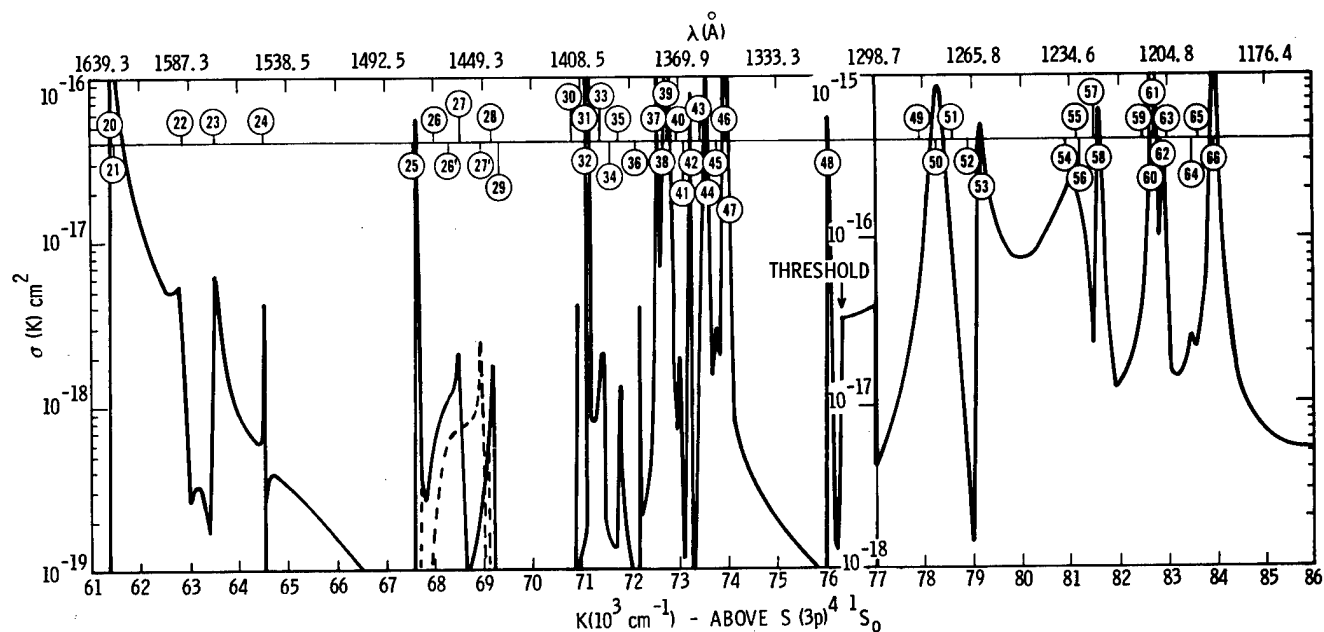
Fig. 47. The effective photoionization cross section of sulphur $(3p)^4\ {}^1S_O$ for 1640 Å $\leq \lambda \leq$ 1163 Å. The numbers in circles refer to the autoionizing levels in Table IV contributing to the cross section. The threshold at 76270 cm^{-1} corresponds to $(3p)^3\ {}^2D$ level of the ion.

45
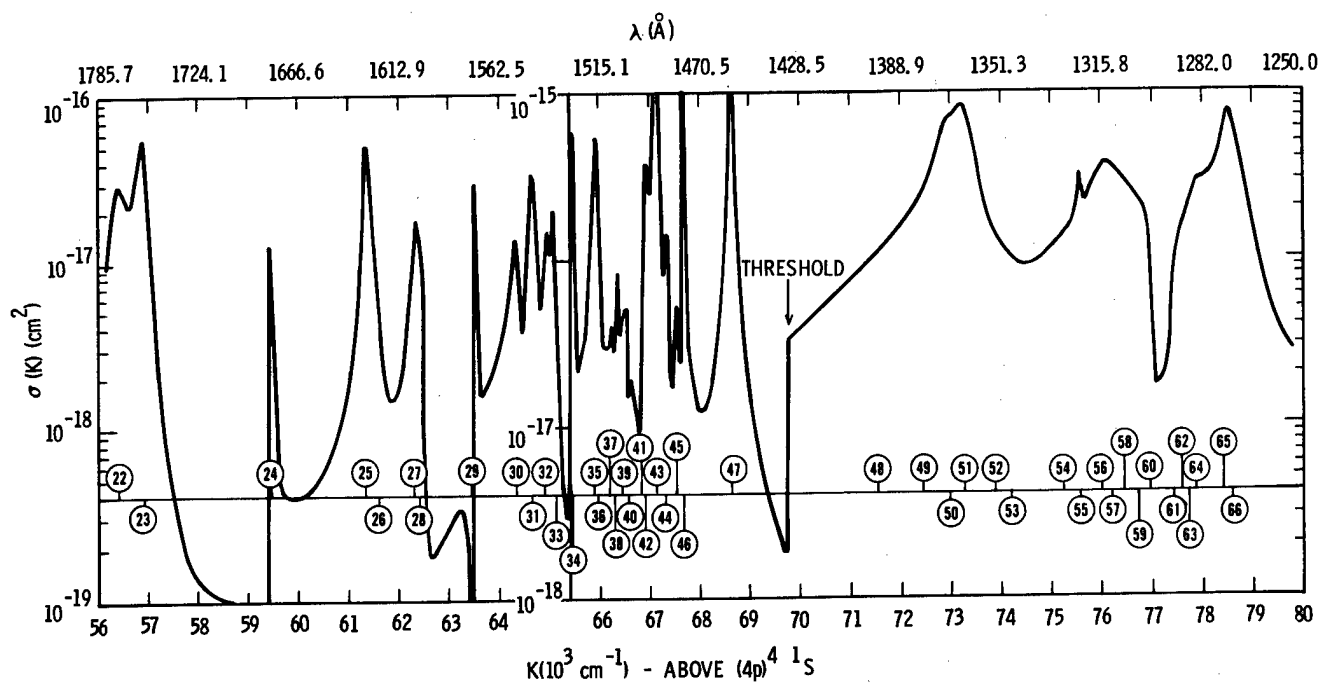
Fig. 48. The effective photoionization cross section of selenium $(4p)^4\ {}^1S_O$ for $1785\ \text{Å} \leq \lambda \leq 1250\ \text{Å}$. The numbers in circles refer to the autoionizing levels in Table V contributing to the cross section. The threshold at $69,750\ \text{cm}^{-1}$ corresponds to the $(4p)^3\ {}^2D$ level of the ion.
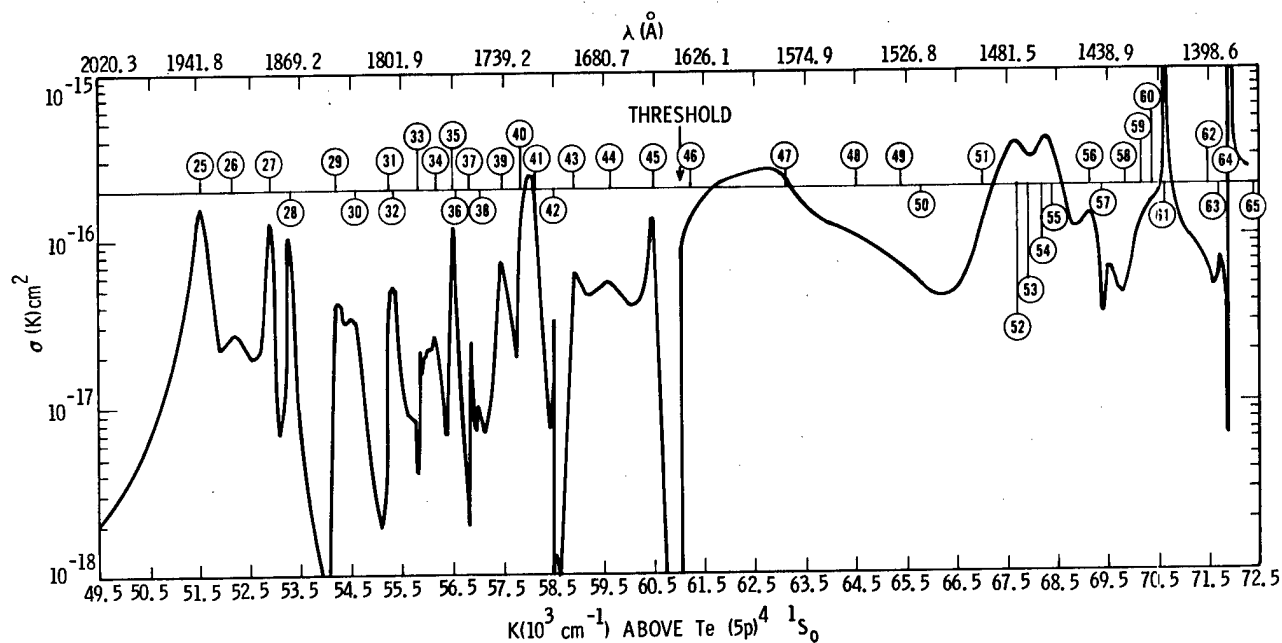
Fig. 49. The effective photoionization cross section of tellurium $(5p)^4\ {}^1S_O$ for $2020\ \text{Å} \leq \lambda \leq 1383\ \text{Å}$. The numbers in circles refer to the autoionizing levels in Table VI contributing to the cross section. The threshold at $61050\ \text{cm}^{-1}$ corresponds to the $(5p)^3\ {}^2D$ level of the ion.

TABLE IV

Energies, Levelwidths, and Oscillator Strengths from
$(3p)^4\,^1S_O$ in Sulphur for 67 Odd Parity Levels with $J = 1$ *

Level No.	Designation	K_i (cm^{-1})	K_f (cm^{-1})	K_{exp} (cm^{-1})	K(CSL) (cm^{-1})	Γ (cm^{-1})	Γ_{exp} (cm^{-1})	Γ(CSL) (cm^{-1})	$f\left[(3p)^4\,^1S_0\right]$
1	$(3p)^3\,^4S(4s)\,^3S$	-28039	-28220	-28228					1.3-4
2	$(3d)\,^5D$	-15612	-15676	-15674					2.3-6
3	$^2D(4s)\,^3D$	-15299	-15512	-15729					4.5-4
4	$^4S(3d)\,^3D$	-13097	-13305	-13389					3.0-4
5	$(5s)\,^3S$	-12210	-12206	-12206					3.6-5
6	$(4d)\,^5D$	-8520	-8538	-8583					2.2-6
7	$\left[-0.580(3s)^1(3p)^5 -0.585\,^2P(4s)\right]^3P$	2000	-8176	-11259					3.1-4
8	$^4S(4d)\,^3D$	-7605	-7684	-7606					1.5-4
9	$(6s)\,^3S$	-6846	-6837	-6838					2.6-5
10	$(5d)\,^5D$	-5325	-5323	-5289					2.2-9
11	$^2P(4s)\,^1P$	-4189	-4877	-5269					0.163
12	$^4S(5d)\,^3D$	-4791	-4804	-4867					2.8-4
13	$(7s)\,^3S$	-4380	-4373	-4373					1.5-6
14	$^2P(4s)\,^3P$	-5609	-4303	-6399					1.3-4
15	$^4S(6d)\,^5D$	-3633	-3626	-3567					3.3-8
16	^3D	-3294	-3268	-3376					4.5-5

47

TABLE IV
(cont)

Level No.	Designation	K_i (cm⁻¹)	K_f (cm⁻¹)	K_{exp} (cm⁻¹)	K(CSL) (cm⁻¹)	Γ (cm⁻¹)	Γ_{exp} (cm⁻¹)	Γ(CSL) (cm⁻¹)	$f[(3p)^4 \, ^1S_0]$
17	(8s) ^3S	-3046	-3037	-3037					9.8-7
18	(7d) ^5D	-2564	-2551	-2564					5.8-10
19	^3D	-2296	-2179	-2477					9.1-5
20	$^2D(3d)\ ^1P$	469	40			180			0.0151
21	^3D	96	106	(123)	1514	85.7	B	724	0.0057
22	^3S	1586	1500	(1872)	2534	166	95	59	3.1-4
23	(5s) ^3D	2174	2149	(2121)	2764	88.7	81	102	2.9-4
24	(3d) ^3P	1004	3164	(2927)		0.74	N		1.0-4
25	(4d) ^1P	6970	6282			0.61			0.0013
26	^3D	6654	6663	(6939)	7239	665	B		2.3-4
27	^3S	7195	7174	(7628)	7974	94.0	62	16	1.4-4
28	(6s) ^3D	7837	7802	(7822)	8182	48.3	100	19	5.8-5
29	(4d) ^3P	6985	7978	(7935)		0.014	N		1.9-4
30	(5d) ^1P	9801	9468			0.30			1.8-4
31	^3D	9722	9720	(10338)	9838	435	B	123	8.2-5
32	$^2P(3d)\ ^3P$	9530	9760			1.33			2.5-4

TABLE IV
(cont)

Level No.	Designation	K_i (cm^{-1})	K_f (cm^{-1})	K_{exp} (cm^{-1})	$K(CSL)$ (cm^{-1})	Γ (cm^{-1})	Γ_{exp} (cm^{-1})	$\Gamma(CSL)$ (cm^{-1})	$f[(3p)^4\ ^1S_0]$
33	$^2D(5d)\ ^3S$	10038	10046		10485	58.8		13	5.2-5
34	$^2P(3d)\ ^3D$	10159	10227	(10338)		642	B		7.9-5
35	$^2D(7s)\ ^3D$	10401	10399	(10338)	10507	49.1	B	33	7.1-5
36	$(6d)\ ^3P$	11471	10778			1.11			4.8-5
37	^1P	11400	11170			0.47			0.0117
38	^3D	11349	11340			236			0.0037
39	$^2P(3d)\ ^1P$	11765	11380			3.97			0.144
40	$^2D(6d)\ ^3S$	11550	11579			45.6			1.7-4
41	$(8s)\ ^3D$	11779	11747			8.08			3.9-9
42	$^2P(5s)\ ^3P$	11864	11891	(11631)		0.21	N		3.4-4
43	$^2D(7d)\ ^3P$	12491	12057	(12082)		0.12	N		1.2-4
44	^1P	12435	12206	(12316)		0.93	N		0.0332
45	^3D	12395	12385			200			4.8-4
46	$^2P(5s)\ ^1P$	12188	12558			2.44			0.0889
47	$^2D(7d)\ ^3S$	12553	12649			69.8			0.0015
48	$\left[-0.507\ ^2P(4d)-0.316\ ^2D(5d)\right]^3P$	9914	14649			0.28			7.7-4
49	$^2P(4d)\ ^3D$	16480	16533	(16401)		453	B		1.6-5
50	^1P	17064	16909			205			0.135

TABLE IV
(cont)

Level No.	Designation	K_i (cm^{-1})	K_f (cm^{-1})	K_{exp} (cm^{-1})	K(CSL) (cm^{-1})	Γ (cm^{-1})	Γ_{exp} (cm^{-1})	Γ(CSL) (cm^{-1})	$f[(3p)^4\,^1S_0]$
51	^3P	16251	17263			7707			5.4-4
52	(6s) ^3P	17257	17560	(17461)	17747	551	B	800	5.4-4
53	^1P	17652	17738		17889	134		30	0.0393
54	(5d) ^3D	19491	19530	(19587)		278	B		5.7-5
55	^1P	19832	19773			628			0.0743
56	^3P	19358	19812		19775	2117		55	0.0125
57	(7s) ^3P	20091	20108	(20068)	20203	51.5	B	47	0.0012
58	^1P	20150	20216		20269	77.6		16	0.0225
59	(6d) ^3D	21090	21123	(21186)		192	79		2.4-4
60	^3P	21005	21291		21289	1557		44	0.0057
61	^1P	21307	21327			72.0			0.0587
62	(8s) ^3P	21469	21482	(21461)	21530	22.3	B	17	0.0025
63	^1P	21499	21564		21464	62.5		9	0.0193
64	(7d) ^3D	22125	22158	(22116)		177	61		2.6-4
65	^3P	22058	22267			1262			3.8-5
66	^1P	22296	22594			25.8			0.233
67	$(3s)^1(3p)^5\,^1P$	55539	57905			104850			0.976

*The column entries are explained in the text. The notation B and N in column 8 are for broad and narrow levelwidths, respectively.

TABLE V

Energies, Levelwidths, and Oscillator Strengths From
$(4p)^4 \, {}^1S_0$ in Se for 67 Odd Parity Levels with J = 1*

Level No.	Designation	K_i (cm^{-1})	K_f (cm^{-1})	K_{exp} (cm^{-1})	Π (cm^{-1})	$f[(4p)^4 \, {}^1S]$
1	$(4p)^3 \, {}^4S(5s) \, {}^3S$	-27203	-27646	-27661		0.0034
2	${}^2D(5s) \, {}^3D$	-15898	-16694	-16977		0.0077
3	${}^4S(4d) \, {}^5D$	-15014	-15276	-15276		1.3-6
4	${}^3D$	-13078	-13390	-13359		0.0079
5	$(6s) \, {}^3S$	-11811	-12033	-12035		8.0-4
6	$(5d) \, {}^5D$	-8105	-8316	-8270		3.2-5
7	${}^3D$	-7204	-7435	-7552		0.0039
8	$(7s) \, {}^3S$	-6527	-6763	-6768		6.2-4
9	${}^2P(5s) \, {}^3P$	-5842	-6617	-7459		0.0125
10	${}^4S(6d) \, {}^5D$	-4994	-5187	-5115		2.1-5
11	${}^2P(5s) \, {}^1P$	-4343	-4744	-6089		0.155
12	${}^4S(6d) \, {}^3D$	-4484	-4662	-4794		0.0034
13	$(8s) \, {}^3S$	-4144	-4351	-4340		1.2-4
14	$(7d) \, {}^5D$	-3358	-3551	-3504		1.2-4
15	$0.482 \, {}^2D(4d) \, {}^3P - 0.638 \, {}^4S(7d) \, {}^3D$	-125	-3261	-3400		0.0077

TABLE V
(cont)

Level No.	Designation	K_i (cm^{-1})	K_f (cm^{-1})	K_f (cm^{-1})	Γ(cm^{-1})	$f[(4p)^4\,^1S]$
16	$0.423\ ^2D(4d)\ ^3P + 0.695\ ^4S(7d)\ ^3D$	-3049	-3165	-3293		8.8-4
17	$^4S(9s)\ ^3S$	-2813	-3017	-3020		1.9-4
18	$(8d)\ ^5D$	-2398	-2587	-2497		1.7-6
19	^3D	-2190	-2290	-2442		0.0016
20	$^2D(4d)\ ^3D$	-819	-1281			0.0149
21	^1P	-532	-900			0.0327
22	^3S	321	190		341	0.0072
23	$(6s)\ ^3D$	1198	710		175	0.0076
24	$^2D[-0.469(4d)+0.695(5d)]\ ^3P$	6068	3228		27.8	2.5-4
25	$^2D(5d)\ ^1P$	5880	5168		126	0.0054
26	^3D	5746	5418		326	0.0012
27	^3S	6274	6126		176	0.0030
28	$(7s)\ ^3D$	6764	6233		98.4	0.0016
29	$^2D[0.551(5d)-0.661(6d)]\ ^3P$	8909	7264		8.62	3.4-4
30	$^2D(6d)(-0.645\ ^3D-0.690\ ^1P)$	8803	8162		134	6.4-4
31	$^2D(6d)(-0.701\ ^3D+0.591\ ^1P)$	8727	8460		134	0.0029
32	$^2D(8s)\ ^3D$	9269	8727		73.6	0.0011
33	$(6d)\ ^3S$	9026	8896		97.0	0.0011

TABLE V
(cont)

Level No.	Designation	K_i (cm^{-1})	K_f (cm^{-1})	K_{exp} (cm^{-1})	Γ(cm^{-1})	$f[(4p)^4\,{}^1S]$
34	$[0.494\ {}^2P(4d)+0.571\ {}^2D(6d)]\ {}^3P$	9040	9256		10.2	0.0070
35	$-0.433\ {}^2P(4d)\ {}^3P+0.512\ {}^2D(7d)\ {}^1P$	10343	9704		60.8	0.0149
36	${}^2D(7d)\ {}^3D$	10297	9752		309	0.0049
37	$[0.528\ {}^2D(9d)+0.551\ {}^2P(4d)]\ {}^3D$	9524	10028		158	0.0010
38	${}^2D(9s)\ {}^3D$	10630	10105		2.69	4.3-4
39	${}^2D(7d)(-0.463\ {}^3P-0.468\ {}^1P)$	10407	10248		298	0.0025
40	${}^2D(7d)\ {}^3S$	10478	10352		43.1	3.5-4
41	${}^2D[-0.437(7d)\ {}^3S-0.652(8d)\ {}^3P]$	11298	10668		66.7	0.0095
42	${}^2D(8d)\ {}^3D$	11224	10682		79.5	3.0-4
43	${}^2P(4d)\ {}^1P$	10760	10939		48.1	0.133
44	${}^2D(8d)(0.439\ {}^3P+0.626\ {}^1P)$	11255	11147		39.6	0.0045
45	${}^2D(8d)\ {}^3S$	11345	11327		102	0.0032
46	${}^2P(6s)\ {}^3P$	11254	11431		7.69	0.0573
47	${}^1P$	11617	12453		41.1	0.127
48	$[0.355(4s)^1(4p)^5+0.697\ {}^2P(5d)]\ {}^3P$	15711	15322		9959	0.0236
49	${}^2P(5d)\ {}^3D$	15936	16258		2179	0.0080
50	${}^2P[-0.675(7s)\ {}^3P-0.442(5d)\ {}^1P]$	16820	16777		449	0.0188

TABLE V
(cont)

Level No.	Designation	K_i (cm^{-1})	K_f (cm^{-1})	K_{exp} (cm^{-1})	Γ(cm^{-1})	$f\left[(4p)^4\ ^1S\right]$
51	$^2P\ \left[0.571(7s)\ ^3P-0.696(5d)\ ^1P\right]$	16510	17063		477	0.111
52	$^2P(7s)\ ^1P$	16995	17680		2282	0.0230
53	$\left[-0.375(4s)^1(4p)^5+0.539\ ^2P(5d)\right]^3P$	10000	18019		9476	0.0312
54	$^2P(6d)\ ^3D$	18859	19050		1474	0.0185
55	$(8s)\ ^3P$	19325	19356		62.6	0.0010
56	$(6d)\ ^1P$	19184	19780		843	0.0669
57	^3P	18732	19980		2257	0.0035
58	$^2P(8s)(-0.445\ ^3P-0.679\ ^1P)$	19418	20218		1237	0.0271
59	$^2P(7d)\ ^3D$	20399	20555		891	0.0269
60	$(9s)\ ^3P$	20686	20731		188	0.0083
61	$^2P(7d)(0.498\ ^3D-0.520\ ^1P)$	20596	21199		300	0.0116
62	$^2P\left[-0.381(9s)\ ^1P-0.696(7d)\right]^3P$	20322	21358		568	0.0197
63	$^2P\left[-0.517(9s)\ ^1P+0.423(7d)\right]^3P$	20759	21492		1855	0.0016
64	$^2P\left[0.477(9s)\ ^1P+0.627(8d)\right]^3D$	21311	21625		427	0.0866
65	$^2P(8d)\ ^3P$	21259	22236		2330	7.2-4
66	^1P	21443	22372		461	0.234
67	$(4s)^1(4p)^5\ ^1P$	51000	53209		79260	1.043

*The column entries are explained in the text.

TABLE VI

Energies, Levelwidths, and Oscillator Strengths From
$(4p)^4\ ^1S_0$ in Te for 67 Odd Parity Levels With $J = 1$*

Level No.	Designation	K_i (cm^{-1})	K_f (cm^{-1})	K_{exp} (cm^{-1})	Γ(cm^{-1})	$f[(5p)^4\ ^1S_0]$
1	$(5p)^3\ ^4S(6s)\ ^3S$	-25643	-26778	-26814		0.0124
2	$^2D(6s)\ ^3D$	-16542	-18296	(-18782)		0.0110
3	$^4S(5d)\ ^5D$	-16144	-17219	(-17621)		8.3-4
4	^3D	-12919	-14355	(-14635)		0.0381
5	$(7s)\ ^3S$	-11177	-12089	(-12380)		0.0010
6	$[0.529(5s)^1(5p)^5 -0.599\ ^2D(5d)]\ ^3P$	-2338	-10722	(-10167)		0.0622
7	$^4S(6d)\ ^5D$	-8605	-9368	(-9170)		0.0024
8	^3D	-6907	-7865	-7772		0.0088
9	$(8s)\ ^3S$	-6381	-7253			0.0016
10	$(7d)\ ^5D$	-5283	-6086	-6030		2.2-4
11	$^2D(5d)\ ^1P$	-3004	-5866	(-5691)		0.0016
12	$^4S(7d)\ ^3D$	-4366	-5196	-5253		0.0018
13	$(9s)\ ^3S$	-4120	-4992			1.4-5
14	$^2D(5d)\ ^3D$	-3484	-4788	-3890		0.0365
15	$[0.655\ ^2P(6s)\ ^3P-0.522\ ^2D(5d)\ ^3D]$	-5269	-4506			0.0223
16	$^4S(8d)\ ^5D$	-3564	-4346	-4322		4.4-4
17	$(10s)\ ^3S$	-2889	-3765			1.6-5

TABLE VI
(cont)

Level No.	Designation	K_i (cm^{-1})	K_f (cm^{-1})	K_{exp} (cm^{-1})	Γ(cm^{-1})	$f\left[(5p)^4\,{}^1S_0\right]$
18	(8d) ^{3}D	-3020	-3737			0.0133
19	(9d) ^{5}D	-2564	-3356	-3330		9.2-5
20	^{3}D	-2212	-2726	-3067		0.0266
21	^{2}D(5d) ^{3}S	-1602	-2251			0.0120
22	(7s) ^{3}D	-223	-1658			3.3-4
23	^{2}P(6s) ^{1}P	-3604	-1295			0.143
24	^{2}D$\left[-0.565(5d)+0.593(6d)\right]{}^3$P	4150	-113			0.0017
25	^{2}D(6d)($-0.621\ {}^3$D$-0.645\ {}^1$P)	3805	2045		322	0.0312
26	^{2}D(6d) ($-0.669\ {}^3$D$+0.556\ {}^1$P)	3549	2656		638	0.0053
27	^{2}D(8s) ^{3}D	4952	3428		87.1	0.0089
28	^{2}D$\left[-0.705(6d)+0.300(7d)\right]{}^3$S	4536	3810		82.4	0.0057
29	^{2}D$\left[0.490(6d)-0.553(7d)\right]{}^3$P	6939	4722		140	0.0034
30	^{2}D(5d) ^{3}D	6615	5112		347	0.0085
31	(9s) ^{3}D	7341	5796		50.0	0.0028
32	^{2}D$\left[0.436(7d)\ {}^3$D$-0.435(8d)\ {}^3$P$\right]$	8403	5880		119	0.0053
33	^{2}D$\left[0.450(7d)+0.434(8d)\right]{}^1$P	6752	6379		14.8	7.2-5
34	^{2}D(8d) ^{3}D	8212	6717		317	0.0066

TABLE VI
(cont)

Level No.	Designation	K_i (cm^{-1})	K_f (cm^{-1})	K_{exp} (cm^{-1})	Γ(cm^{-1})	$f[(5p)^4\ ^1S_0]$
35	$^2D(10s)\ ^3D$	8628	7064		66.6	0.0042
36	$^2D[0.545(10s)\ ^3D-0.516(7d)\ ^3S]$	7148	7097		104	2.3-5
37	$^2D[-0.373(7d)+0.583(5d)\ ^3P]$	9273	7394		21.8	2.1-4
38	$^2D(9d)(0.691\ ^3D+0.548\ ^1P)$	9149	7595		140	0.0016
39	$^2D(8d)(-0.517\ ^3D+0.633\ ^1P)$	8293	8035		234	0.0122
40	$-0.445\ ^2P(5d)\ ^3P+0.555\ ^2D(8d)\ ^3S$	7463	8431		145	0.0144
41	$0.432\ ^2P(5d)\ ^1P+0.512\ ^2D(8d)\ ^3S$	8526	8660		254	0.0425
42	$^2D(9d)(-0.527\ ^3D+0.599\ ^1P)$	9202	9032		4.70	1.4-4
43	$^2D(9s)\ ^3S$	9353	9417		250	0.0119
44	$^2P(5d)(0.686\ ^3D-0.512\ ^3P)$	8269	10141		944	0.0393
45	$^2P(7s)\ ^3P$	11050	11020		133	0.0147
46	$^2P[-0.422(7s)\ ^3P+0.692(5d)\ ^1P]$	10323	11770		1683	0.236
47	$^2P(7s)\ ^1P$	11479	13662		1170	0.0231
48	$^2P(6d)(-0.438\ ^3D-0.579\ ^3P)$	14652	15651		4204	0.110
49	$^2P[-0.423(8s)\ ^3P-0.579(6d)\ ^3D]$	15076	15952		9305	8.8-4
50	$^2P(8s)(0.704\ ^3P-0.478\ ^1P)$	16225	16358		2137	4.9-4
51	$^2P[0.542(6d)-0.461(7d)]\ ^1P$	18609	17592		2391	0.0381

57

TABLE VI
(cont)

Level No.	Designation	K_i (cm^{-1})	K_f (cm^{-1})	K_{exp} (cm^{-1})	Γ(cm^{-1})	$f[(5p)^4\ ^1S_0]$
52	$^2P(6d)(0.525\ ^3P-0.427\ ^1P)$	16156	18253		804	0.0809
53	$^2P[0.480(9s)\ ^3P+0.500(7d)\ ^3D]$	18025	18449		3951	0.0075
54	$^2P(9s)(0.632\ ^3P-0.450\ ^1P)$	18614	18729		3343	0.0013
55	$^2P(8s)(-0.438\ ^3P-0.661\ ^1P)$	16402	18876		563	0.0606
56	$^2P(8d)(-0.612\ ^3D-0.466\ ^1P)$	19566	19708		641	0.0120
57	$^2P(10s)\ ^3P$	19901	19925		85.0	0.0010
58	$^2P(9d)(-0.493\ ^3D-0.484\ ^1P)$	20425	20415		614	0.0059
59	$^2P(7d)\ ^3P$	17796	20719		2205	0.0030
60	$^2P[0.438(9s)-0.406(7d)]\ ^1P$		20921		1195	0.0567
61	$^2P(9s)(0.377\ ^3P+0.594\ ^1P)$	18705	21203		46.2	0.0796
62	$^2P(8d)\ ^3P$	19430	22061		1292	0.0031
63	$^2P[-0.487(10s)+0.475(8d)]\ ^1P$	19912	22239		183	0.0422
64	$^2P(10s)(0.377\ ^3P+0.568\ ^1P)$	19955	22428		24.7	0.0552
65	$^2P(9d)\ ^3P$	20387	22951		845	1.2-4
66	$^2P[-0.386(8d)-0.621(9d)]\ ^1P$	20698	23595		3489	0.432
67	$(5s)^1(5p)^5\ ^1P$	40866	45878		99919	1.569
	$(5s)^1(5p)^5\ ^3P$	5538				

*The column entries are explained in the text.

NEW-LASER RESEARCH AND DEVELOPMENT

OVERVIEW

Two new-laser research efforts were initiated during this report period; the chemically pumped iodine laser and HgXe exciplex excitation by electric discharge. The chemically pumped iodine laser was recently discovered by personnel at the Air Force Weapons Laboratory. This laser offers exciting possibilities as an ICF driver because it does not require a capital-intensive pulse power source to drive it, and up to 10% efficiency may be possible. Modeling studies of this laser are in progress and our opinion of it as a potential high-average power laser is very favorable at this time.

The HgXe exciplex radiates in a band centered at 265 nm. We are studying this system because it could be used to pump an iodine laser. We will also assess its potential to be a high-power laser candidate.

An advanced oscillator system based upon a microprocessor-controlled Nd:YAG-pumped pulsed dye laser is being developed so that it can be used as the front end of new laser-fusion lasers and utilized in testing and making germane laser amplifier measurements of candidate laser systems for the wavelength region of 4000 Å to 8000 Å and extended range with frequency doubling and mixing. The operating requirements of the oscillator system include long-term stability, high reliability, absolute wavelength calibration and control, tunability, hands-off operation, and variable pulse width generation in the nanosecond regime. These requirements necessitate the application of microprocessor technology to laser technology thereby resulting in a state-of-the-art system capable of satisfying all of the above operating requirements.

CHEMICALLY PUMPED IODINE LASER

Personnel at the Air Force Weapons Laboratory in Albuquerque have recently been successful in obtaining cw laser oscillation on the 1.3-μm atomic iodine transition by using a purely chemical technique to generate an inversion.[33] The chemically pumped iodine laser system is so different from the photolytically pumped iodine laser that it must be thought of as a distinct entity. It has enough possible advantages as a laser-fusion driver that its potential should be investigated thoroughly. Among the most important advantages of this system over others are the following. First, purely chemical generation of the active medium avoids the capital-intensive pulsed power usually associated with other pumping processes. Simple flow systems and a chemical reactor replace capacitor banks, flashlamps, electron beams, or other sources typically used for pulsed-laser initiation. The absence of pulsed-power requirements will greatly enhance system reliability and should lower capital cost. Second, the iodine laser using chemical generation has the potential for high efficiency. The limiting theoretical efficiency is about 10%, including the cost of chemical regeneration. Third, high repetition rate is easily obtained. The chemical processes leading to a population inversion can be started and stopped quickly and frequently. If the chemically pumped iodine laser is to be developed as an effective ICF driver, it must be demonstrated that the foregoing advantages can be associated with a system that delivers short output pulses. A modeling effort directed at this task has recently been started in this laboratory. The following material briefly summarizes some information pertinent to understanding the chemically pumped iodine laser and indicates preliminary results of the modeling effort.

The chemical generation of excited atomic iodine relies on fortuitous accidents of nature which allow some interesting interactions between excited molecular oxygen and iodine. Figure 50 shows energy levels in the $O_2/I_2/I$ system and illustrates some of the fortunate coincidences. Chemical generation of excited atomic iodine, I^*, starts with a population of excited oxygen molecules in the $O_2(^1\Delta)$ electronic state. The interaction of two such molecules to form $O_2(^3\Sigma)$ plus $O_2(^1\Sigma)$ is energetically

allowed and proceeds to form $O_2(^1\Sigma)$ which collisionally dissociates I_2. As indicated in Fig. 50, the transfer of energy from $O_2(^1\Delta)$ to I to form I^* is slightly exothermic but nearly resonant. In a flowing stream initially containing only $O_2(^1\Delta)$, the injection of I_2 after the $O_2(^1\Sigma)$ density has reached an appreciable value results in the dissociation of I_2 and the excitation of some of the resulting I to I^*.
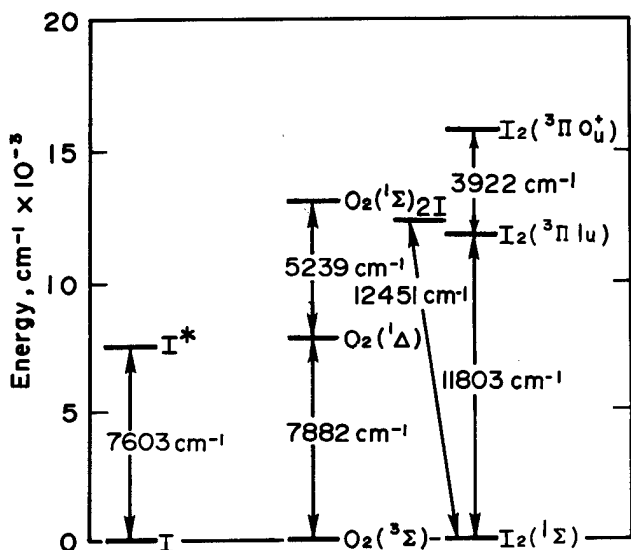

Fig. 50. Some energy levels in the $O_2/I_2/I$ system.

Figure 51 summarizes the most important processes involved in the generation of $O_2(^1\Delta)$ and I^* and also indicates the applicable chemical regeneration processes. The first line summarizes the overall chemistry involved in producing $O_2(^1\Delta)$. Cl_2 is bubbled through a basic solution of 90% H_2O_2, and $O_2(^1\Delta)$ is evolved into the gas phase. $O_2(^1\Delta)$ is thought to be produced in 100% yield in the liquid, but only about 60% yield has so far successfully been extracted into the gas phase before deactivation.[34] An 80% yield of $O_2(^1\Delta)$ is thought to be feasible. The next several lines summarize the chemical kinetics involved in generating I^*. The first step is energy pooling, that is the generation of $O_2(^1\Sigma)$. Next, $O_2(^1\Sigma)$ dissociates I_2. The collisional transfer of energy from $O_2(^1\Delta)$ to generate I^* then proceeds quickly. Both the excitation reaction and its reverse are very fast so that equilibrium is established

between oxygen molecules and iodine atoms even in the presence of other rapid processes:

$$\frac{[O_2(^3\Sigma)][I^*]}{[O_2(^1\Delta)][I]} = K_{eq} = 2.9 \qquad (11)$$

where brackets signify concentrations. An iodine inversion exists whenever $[O_2(^1\Delta)]/[O_2(^3\Sigma)] > 0.17$. The final reaction shown is another formation route for $O_2(^1\Sigma)$. This reaction proceeds faster than the initial pooling reaction and the resulting $O_2(^1\Sigma)$ ensures that the dissociation of I_2 is essentially complete.

GENERATION

$$Cl_2 + H_2O_2 + OH^- \longrightarrow H_2O + HCl + Cl^- + O_2(^1\Delta)$$

$$O_2(^1\Delta) + O_2(^1\Delta) \longrightarrow O_2(^1\Sigma) + O_2$$

Feedback:

$$O_2(^1\Sigma) + I_2 \longrightarrow O_2 + I + I$$

$$O_2(^1\Delta) + I \rightleftharpoons O_2 + I^* \text{ (FAST)}$$

$$O_2(^1\Delta) + I^* \longrightarrow O_2(^1\Sigma) + I$$

REGENERATION

$$H_2O + HCl + Cl^- \longrightarrow H_2 + Cl_2 + OH^-$$

(Electrolysis)

$$H_2 + O_2 \longrightarrow H_2O_2$$

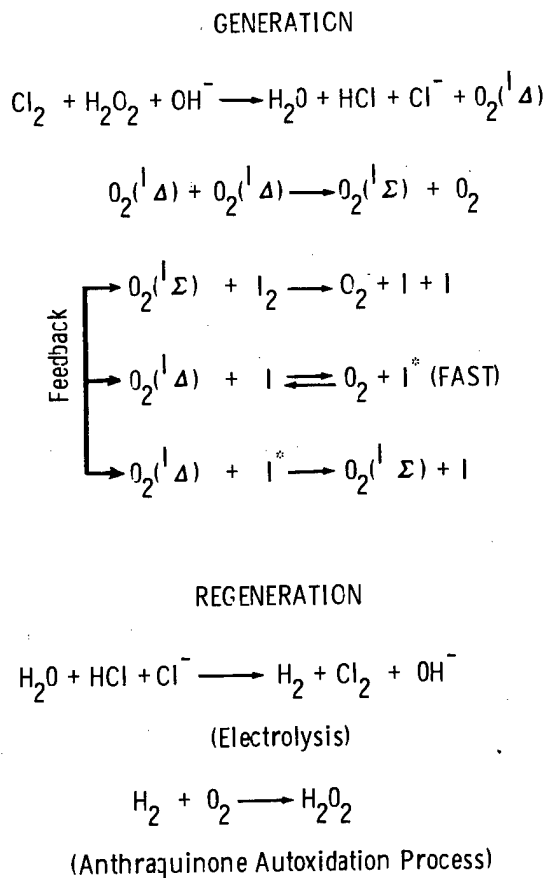(Anthraquinone Autoxidation Process)

Fig. 51. Scheme for chemical generation of excited iodine atoms and commercial processes for regeneration of starting chemicals.

Regeneration of starting materials in the chemically pumped iodine laser system involves two steps. First, the residual liquid solution from the chemical generator is subjected to electrolysis to yield H_2 and Cl_2.[35] Second, H_2 and O_2 are combined to form H_2O_2 using a reaction sequence involving the formation of an anthraquinone derivative.[36] Both steps utilize well developed, commercial industrial procedures with high efficiencies. The overall regeneration process should have greater than 50% efficiency relative to the thermodynamic minimum energy requirement, based on the experimentally observed industrial efficiencies.

The foregoing serves as background material for understanding the chemically pumped iodine laser system. It remains to be demonstrated that this system can be used efficiently to generate short output pulses. A potential complication arises from the fact that only a small fraction of the total stored energy in the chemical system is present in I^* at any instant. When energy is extracted as 1.3-μm iodine radiation, energy stored in $O_2(^1\Delta)$ subsequently feeds rapidly into I^* to reestablish the equilibrium indicated by Eq (11). Several sequential extractions must be performed before most of the energy initially stored in $O_2(^1\Delta)$ is extracted as 1.3-μm iodine radiation. As partial compensation for this complication, the gain in a chemically pumped iodine laser is low enough that amplified spontaneous emission is not a problem even for large stored energies. The modeling effort has so far been directed toward obtaining information about the number of extractions required for a given efficiency, the physical size of a laser having a given stored energy, and the sensitivity of predicted performance to uncertain chemical rate constants. All the reactions shown in Fig. 51 plus several others have been considered and presently accepted values of rate constants have been used.[37,38]

Typical starting conditions for calculations assume the presence of 10 torr O_2, 80% of which is $O_2(^1\Delta)$. After sufficient time for the generation of adequate $O_2(^1\Sigma)$, 0.3-torr I_2 and 100-torr Ar are added. The Ar serves two purposes. It carries I_2 into the O_2 stream and it pressure-broadens the iodine

transition. Calculations indicate that sufficient Ar can be added for the iodine transition to be effectively homogeneously broadened without affecting the kinetics adversely. Shortly following the addition of I_2, several energy extractions are performed sequentially, separated in time by 200 ns, a time shown in auxilliary calculations to be sufficient for approximate reequilibration to Eq (11). Present results indicate that the system is attractive. Extractable energy is high, about 15 J/L for the example given here. An amplifier with an extractable energy of 10 kJ could have an aperture 50-cm in diameter and a length of 3.5 m. Amplified spontaneous emission would not be a problem and 20 extractions would yield an overall efficiency of 6%.

The calculations indicate that several reactions for which rate constants are not well known may have important bearing on overall system performance. For instance, the process

$$I^* + O_2(^1\Delta) \rightarrow I + O_2(^1\Sigma) \tag{12}$$
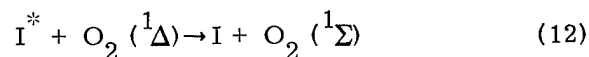
proceeds far faster than necessary to ensure complete dissociation of I_2 when the presently accepted, but uncertain, value of its rate constant is used in the calculations. The result is a buildup of $O_2(^1\Sigma)$, which represents a loss of stored energy because no pathway starting with $O_2(^1\Sigma)$ and leading to I^* exists. The calculations also indicate that more needs to be known about processes involving low-lying electronically excited states of I_2 and about several deactivation processes. Kinetic modeling is far from complete, but it is already clear that it will be important to obtain reliable experimental determinations of several rate constants as the first part of an experimental exploration of the potential utility of this system as a laser fusion driver.

HgXe EXCIPLEX STUDIES

The HgXe excimer band centered at 265 nm offers promise as an efficient ultraviolet

pump source and possibly as an efficient ultraviolet laser. In this report, we will present the results of preliminary experiments to measure the fluorescence efficiency of HgXe ($^3O^+ \rightarrow {}^1O^+$) emission at 265 nm in a discharge stabilized by electron-beam pre-ionization. These results will then be qualitatively related to the predictions for fractional power transfer into the Hg states by a Boltzmann transport code.

Experimental

The experimental apparatus is shown schematically in Fig. 52. A Febetron 706 electron-beam accelerator whose output was attenuated by a factor of one hundred using wire screens was used to preionize a gas mixture containing 10 torr to 15 torr of Hg and 1500 torr to 3000 torr of Xe in a stainless-steel test cell. The attenuated electron beam was characterized by an average electron energy of 600 keV, a current density of 100 A/cm^2 and, a pulsewidth of ~4 ns (FWHM).
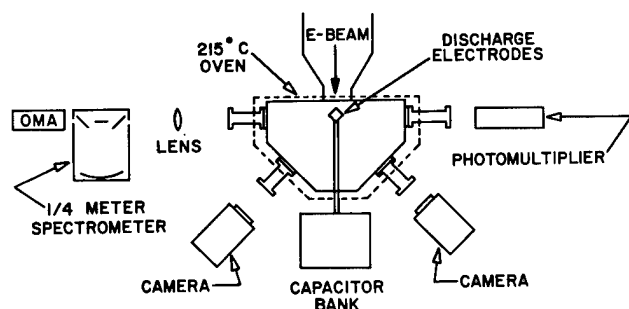

Fig. 52. Schematic diagram of experimental apparatus.

A capacitor whose value was varied from 2700 pF to 0.01 μF was charged from 1 kV to 4 kV. It supplied energy to the Hg/Xe mixture via a krytron switch which was triggered at a controlled delay time following the electron-beam pulse.

The discharge occurred between two stainless-steel electrodes spaced by 0.43 cm. The actual discharge volume was determined by photographing the discharge at right angles as shown in Fig. 52. The current drawn by the discharge was limited by a 2-kilohm ballast resistor between the anode and ground.

This allowed stable discharges to be maintained for a few microseconds.

The voltage drop across the discharge was measured by two 100:1 voltage probes positioned at the cathode and anode feedthroughs into the test cell. The current flowing through the discharge was determined by measuring the voltage drop across the current-limiting resistor.

The temporal behavior and intensity of the HgXe emission was observed on a Hamamatsu R166 photomultiplier having a CsTe photocathode. The photomultiplier plus appropriate neutral density filters were absolutely calibrated by comparing their response to a monochromatic light source to that of a photodiode which had been absolutely calibrated by the National Bureau of Standards.

Emission spectra of HgXe were taken by using a quarter-meter Jobin-Yvon spectrometer and a PAR OMA2 optical multichannel analyzer. The relative wavelength response of the entire system was determined by using an Optronic Model W-40 calibrated low-pressure D$_2$ discharge lamp.

The Xe gas used in this experiment was obtained from Cryogenic Rare Gases at a stated purity of 99.999% and was used without further purification. The Hg used in the experiment was triple-distilled. The Hg pressure supplied to the test cell was determined by the temperature in a temperature-regulated Hg reservoir. The temperature of the test cell was always maintained above the temperature of the Hg reservoir at a constant of 215°C.

Results

The fluorescence efficiency of the HgXe ($^3O^+ \rightarrow {}^1O^+$) transition is defined here as the energy emitted into 4-π steradians by the 265-nm band divided by the energy deposited in the Hg/Xe gas mixture by the discharge. Implicit in this definition is the assumption that the electron-beam used to preionize the discharge creates a relatively small HgXe ($^3O^+$) excited state population that has radiatively decayed prior to the triggering of the discharge. This is well-illustrated in

Fig. 53, which shows the photomultiplier
signal during a discharge in 15 torr of Hg
and 3000 torr of Xe with an energy input of
~1.9 J/l. The first peak is emission from
HgXe created by the electron-beam. The
second and much larger peak arises from
HgXe created by the discharge which is trig-
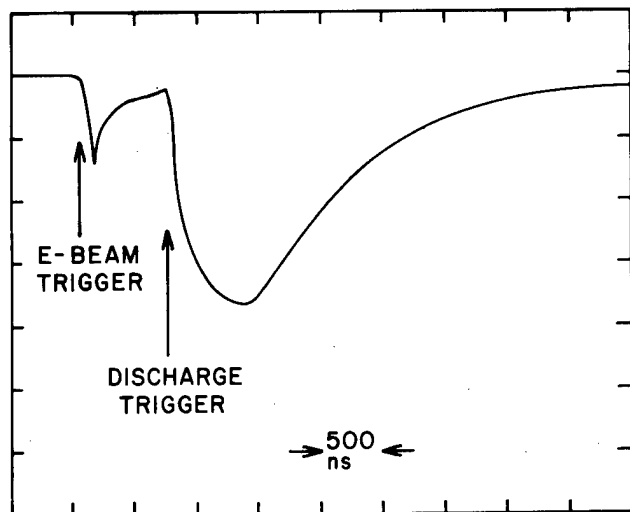gered some 700 ns after the preionizing
pulse.

Fig. 53. Optical output with electron-beam
preionized discharge excitation in
15 torr of Hg and 3000 torr of Xe.

The energy deposited in the HgXe mixture is
calculated by multiplying the voltage drop
across the discharge as a function of time
by the current drawn by the discharge as a
function of time. Figure 54 shows the volt-
age and current measurements during a dis-
charge in 15 torr of Hg and 3000 torr of Xe
with an energy input of 1.9 J/l.

The energy emitted into 4-π steradians by
the HgXe emission produced by the discharge
is calculated from the photomultiplier tube
response by assuming the discharge is a
point source. In this case the energy is
given in joules by the expression

$$E \ (J) = 4.7 \ \frac{4\pi d^2}{A} \ \frac{\int_o^\infty V dt}{(50\Omega) \times T \times G}$$
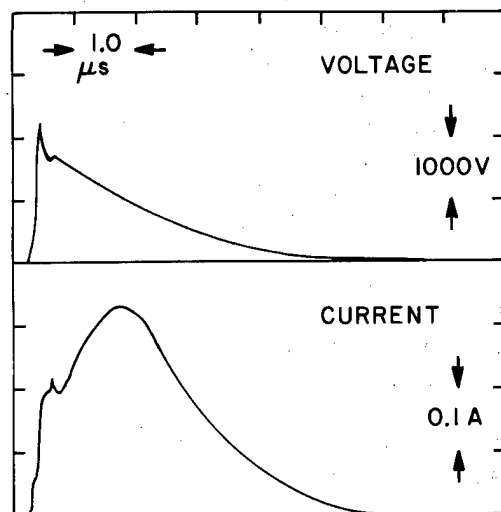

Fig. 54. Electric discharge voltage (upper)
and current (lower) in 15 torr of
Hg and 3000 torr of Xe.

where d is the distance between the dis-
charge and the photomultiplier in cm, A is
the area in cm^2 of an aperture which defines
the area of the photocathode that is illumi-
nated, T is the overall transmission of the
windows between the discharge and the photo-
multiplier, and G is the gain of the photo-
multiplier times its quantum efficiency
taking into account any neutral density filter
used during the experiment. Since G is a
function of wavelength it must be convoluted
with the spectrum obtained from the OMA to
obtain an absolute efficiency for the fluores-
cence emission.

The preliminary results indicate that the
HgXe ($^3O^+ \rightarrow {}^1O^+$) fluorescence efficiency
ranges from 6.6 to 3.3% as the power input
varies from 4 to 6 x 10^5 W/l at an E/N of
5 x 10^{-17} V-cm^2. At an E/N of 8 x 10^{-17}
V-cm^2, the fluorescence efficiency ranges
from 4.3 to 3.7% as the power input varies
from 1 to 2 x 10^6 W/l. Under these condi-
tions the electron density was ~10^{13} cm^{-3}
and the fractional ionization was ~10^{-7}.
The fraction of excited states was on the
order of 10^{-4}. Efficiencies could not be
determined at energy inputs above 2.0 J/l,
because the discharge went unstable.

A Boltzmann transport code has been used to predict the fractional power transferred to the various Hg states which correlate directly with HgXe states under conditions of high xenon pressure. The code predicts an order of magnitude increase in power transferred to the Hg ($^1P_1$) state in going from an E/N value of 5×10^{-17} V-cm^2 to 8×10^{-17} V-cm^2 at a constant Hg pressure of 15 torr. The Hg ($^1P_1$) state correlates with the HgXe ($^1O^+ \rightarrow {}^1O^+$) transition centered at ~ 210 nm. Figure 55 shows the emission spectra taken with the OMA unfolded from the wavelength response of the spectrometer and detector. At an E/N of 5×10^{-17} V-cm^2, no 210-nm emission is seen. At an E/N of 8×10^{17} V-cm^2, this band is always observed. These results hold regardless of whether E/N is varied by changing E or changing N.
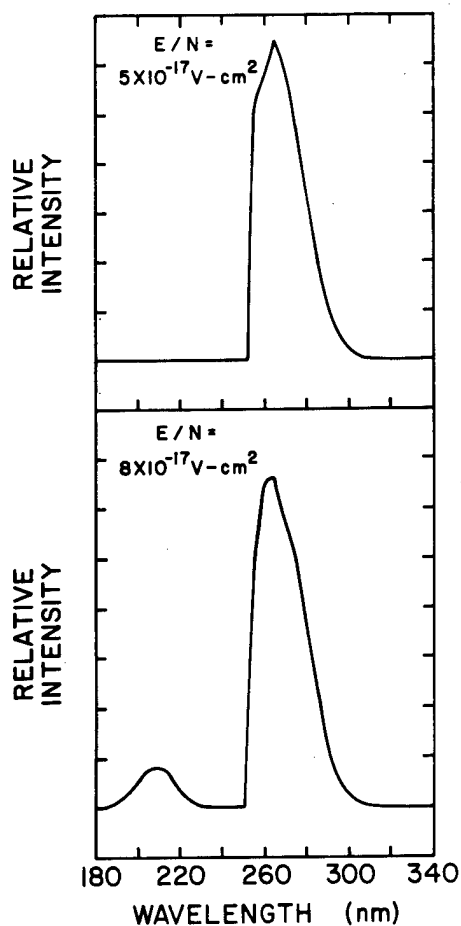

Fig. 55. HgXe discharge spectra taken at E/N values of 5×10^{-17} (upper) and 8×10^{-17} (lower) V-cm^2.

Summary

Fluorescence efficiencies for the HgXe ($^3O^+ \rightarrow {}^1O^+$) emission on the order of 4% have been measured at power inputs of $\sim 10^6$ W/1 in stable, electron-beam preionized discharge. The discharge goes unstable at power inputs greater than 2×10^6 W/1. Greater power inputs should be realizable by using an electron-beam sustained discharge.

OSCILLATOR STUDIES

An advanced oscillator system based upon a microprocessor-controlled Nd:YAG-pumped pulsed dye laser should meet all the near-to-mid term oscillator needs of advanced laser-fusion lasers with the exception of HF. Not only can this master oscillator concept be used as the front end of the laser fusion device, but it also can be utilized in testing and making germane laser amplifier measurements of candidate laser systems for the wavelength region of 4000 Å to 8000 Å and extended range with frequency doubling and mixing.

The operating requirements of such an oscillator system include long-term stability, high reliability, absolute wavelength calibration and control, tunability, hands-off operation, and variable pulse width generation in the nanosecond regime. These requirements necessitate the application of microprocessor technology to laser technology thereby resulting in a state-of-the-art laser system capable of satisfying all of the above operating requirements.

For FY78, the goal of the Sandia oscillator research and development program is to demonstrate the basic concepts of a microprocessor controlled 5-ns pulsed dye laser system operating between 4500 Å and 5000 Å. These wavelengths do not represent limitations of such a system but are chosen to be in a currently interesting wavelength region for proposed laser fusion devices. By changing the dye, Nd:YAG pumping wavelength, etc., the same system could operate any where between 4000 Å and 8000 Å.

A block diagram of the overall system

design is shown in Fig. 56. As can be seen
there are several basic modules in the design
of this kind of system. For this reporting
period, three aspects of the proposed laser
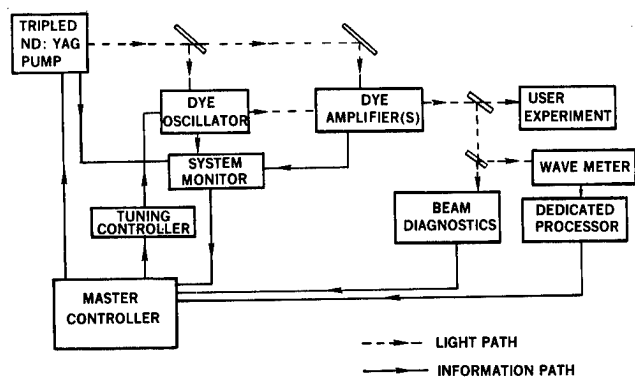oscillator design are discussed.

Fig. 56. Block diagram of overall system
design.

Nd:YAG Oscillator Pump Source

The current configuration of the tripled-
Nd:YAG-pumped pulsed dye oscillator system
is outlined in Fig. 57. The pump laser is a
pulsed, Q-switched Nd:YAG unstable resona-
tor oscillator[39] and amplifier purchased
from Quanta-Ray, Inc. Air-cooling was
added to the Q-switch device in order to pre-
vent breakthrough throughout the operating
temperature range. The output of the
Nd:YAG laser is frequency tripled to provide
7-ns 135-mJ pulses at a wavelength of 354.7
nm and a repetition rate of 10 pps. This
laser system is stable, reliable, has a flash-
lamp life of $> 10^7$ pulses and there is no
detectable alignment drift. The dye oscilla-
tor is based on an optical cavity designed by
Quanta-Ray. It contains a transversely
pumped flowing dye cuvette, a four-prism
dispersionless beam expander, and a littrow-
mount grating for tuning. In order to pump
coumarin and other blue-green dyes more
efficiently, the cuvette and pump-beam optics
have been modified to provide a gain path of
~1.5 cm at reduced pump beam intensity.
While the prism beam expander reduces the
divergence of the dye laser beam as do
telescopic and grazing incidence grating

methods,[40] it has far less stringent align-
ment requirements than the other two techni-
ques and is, therefore, more reliable.
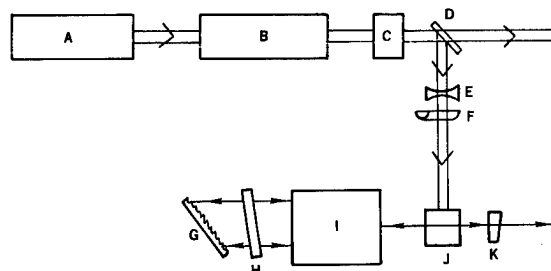
A - Nd:YAG Oscillator
B - Nd:YAG Amplifier
C - Frequency Tripler
D - Beamsplitter
E - Diverging Lens
F - Cylindrical Lens
G - Diffraction Grating
H - Intracavity Etalon
 I - Prism Beam Expander
J - Dye Cuvette
K - Output Coupler

Fig. 57. Nd:YAG/Dye Laser System.

Dye Performance Measurements

In preliminary tests with Rhodamine 6G dye,
the dye oscillator operated with 30% effi-
ciency and 1 cm^{-1} spectral linewidth at a
wavelength of 590 nm. The addition of an
intracavity etalon reduced both the linewidth
to ~0.1 cm^{-1} and the efficiency to 10 to 15%.

Subsequent experiments with blue dyes
showed the best coumarin dye thus far tested
(coumarin 481) to have an efficiency of about
16%, a narrow tuning range, and a short
lifetime (approximately 8 hrs). However,
the best dye tested (LD490) had an efficiency
of ~16% at a spectral linewidth of 1 cm^{-1},
(wavelength of 480 nm) a tuning range of
465 nm to 505 nm at the half-power points
(Fig. 58), and showed no detectable degrada-
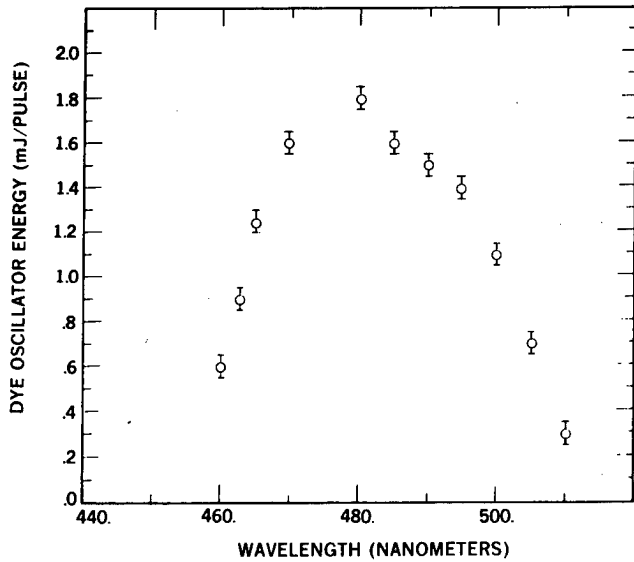tion of efficiency over 8 hr of run time.

Fig. 58. Tuning range of LD490 laser dye.

Microprocessor Controlled Wavemeter

The wavemeter module designed to facilitate automatic control of wavelength for the dye laser is shown in Fig. 59. The design is based on a Fizeau-type wedge interferometer with a Teticon photodiode array readout, as proposed by Snyder.[41] In principle, light beams reflected from the two surfaces of the wedge create a sinusoidal interference pattern on the photodiode array. The intensity values from the photodiodes are digitized, stored, and processed on a microcomputer to yield the frequency and phase of the sinusoidal pattern. This information, combined with the calibrated properties of the wedge, yields a value for the wavelength of the light
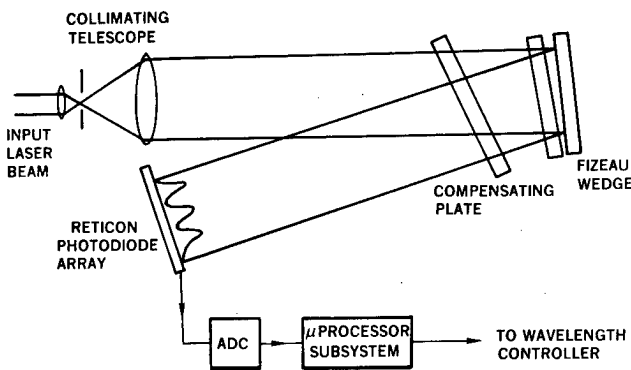
incident on the wedge. A mathematical analysis and extensive computer simulation have revealed several difficulties overlooked by Snyder, and methods have been developed to overcome these problems.

1. The angle of incidence of the light on the wedge which minimizes effects of angular deviation is not zero degrees (normal incidence), as is the case for a parallel-plate interferometer, but is a finite angle which depends upon the distance from the wedge to the detector. The resultant dispersion from the finite thickness of the front plate in the interferometer must be compensated for by the introduction of a similar plate in the reflected beam path.

2. Spatial modulation of the fringe pattern, due to the combination of the spatial profile of the incident beam and slow gain variation along the length of the detector array, changes the apparent locations of the intensity extreme and must be accounted for in the processing software.

3. Curvature of wedge surfaces leads to nonlinearity of fringe spacing, which must be corrected for in the analysis.

Fast, efficient software routines have been developed for the Z-80 microprocessor to process the fringe pattern, incorporating items 2 and 3 above. Currently, the Reticon data can be read and processed approximately four times per second. Software has been written to utilize a hardware arithmetic processor to improve this speed.

Experiments were performed with an etalon having a 0.5-mm separation and a 16 arc-second angle between wedge surfaces, $\lambda/20$ surface flatness, and 3/4 in. clear aperture. Collimation was provided by a Spectra-Physics 200-mm collimating lens and a 10-μm pinhole. Angle of incidence was $\sim$4 degrees, with the Reticon array 30 cm from the wedge. The light source was a single wavelength, from a cw HeNe laser, so no compensating plate was used. The Reticon array was a 1024 element unit with high sensitivity diodes 17 mil wide separated by 1 mil. Digitization of intensity

Fig. 59. Wavemeter.

information was performed with an eight-bit A/D converter with 5.5-μs settling time and ± 1/2 LSB accuracy. The data yielded fringe location and fringe period to an accuracy within a factor of 2 of that necessary to achieve the desired wavelength measurement accuracy of 0.01 cm^{-1} (5 x 10^{-7} at 500 nm wavelength). Uncorrectable intensity variations caused by dust on the wedge surfaces contributed partly to the errors, and it was determined that a clean wedge with a spacing of 0.25 mm and an angle of 25 arc-seconds would provide the required accuracy.

REFERENCES

1. Laser Development for Laser Fusion Applications Research Progress Report October 1977-March 1978, SAND78-0811, Sandia Laboratories, Albuquerque, NM, June 1978.

2. Reference 1, p. 20.

3. M. E. Riley and M. A. Gusinow, Appl. Opt. 16, 2753 (1977).

4. Reference 1, p. 12.

5. Laser Development for Laser Fusion Applications Research Progress Report January-September 1977, SAND77-1517, Sandia Laboratories, Albuquerque, NM, February 1978.

6. Reference 5, p. 16.

7. J. A. Halbleib, Jr., and W. H. VanDevender, SAND74-0030, Sandia Laboratories, Albuquerque, NM, March 1975.

8. Reference 5, p. 17.

9. M. A. Duguay, G. A. Fisk, J. M. Hoffman, J. B. Moreno, R. E. Palmer, M. E. Riley, and R. P. Sandoval, SAND76-0094, Sandia Laboratories, Albuquerque, NM, March 1976.

10. R. P. Sandoval, J. Appl. Phys. (Sept. 1978).

11. Reference 1, p. 16.

12. Reference 1, pp. 27-30.

13. Reference 1, pp. 50-55.

14. Reference 1, p. 42.

15. G. A. Fisk, The Effects of Chemical Kinetics and Starting Material Regeneration on the Efficiency of an Iodine Laser Amplifier, SAND77-0880, Sandia Laboratories, Albuquerque, New Mexico, May 1977.

16. G. A. Fisk, "Multiple Photon Induced Chemistry in Mixtures of C_2F_6 with H_2 or C_6H_{14}," Chem. Phys. Lett., in press.

17. O. P. Judd, Appl. Phys. Lett. 22, 95 (1973).

18. S. J. Kast and C. Cason, J. Appl. Phys. _44_, 1631 (1973).

19. R. Eujen and R. J. Lagow, Inorg. Chem. _14_, 3128 (1975).

20. The Atomic Iodine Laser, SAND78-1071, Sandia Laboratories, Albuquerque, New Mexico, June 1978.

21. Reference 1, pp. 33-35.

22. M. A. Gusinow, Sandia Laboratories, private communication.

23. J. F. Shaw, R. Maynard, and P. Lovoi, Additive Enhancement of Short Pulse Flashlamps, R-ILC-75-13/F, ILC Technology, Inc., Sunnyvale, CA, April 1977.

24. Reference 5, PP. 70-71.

25. M. A. Gusinow, IEEE J. Quantum Electron. QE-11, 929 (1975).

26. F. M. Matsumga and K. Watanabe, J. Chem. Phys. _46_, 4457 (1967).

27. T. G. Slanger and G. Black, J. Chem. Phys. _64_, 3763 (1976).

28. G. Black, R. L. Sharpless, and T. G. Slanger, J. Chem. Phys. _63_, 4551 (1975).

29. C. E. Moore, "Atomic Energy Levels," Natl. Bur. Stand, Circ. No. 467 U. S. GPO, Washington, DC (1949).

30. G. Tondello, Astrophys. Journal _172_, 771 (1972).

31. D. Bartelt, Zeit. Phys. _88_, 522 (1934).

32. M. J. Conneely, K. Smith, and L. Lipsky, J. Phys. B3, 493 (1970).

33. W. E. McDermott, N. R. Pchelkin, D. J. Benard, and R. R. Bousek, Appl. Phys. Lett. _32_, 469 (1978).

34. D. J. Benard and N. R. Pchelkin, Rev. Sci. Instrum. _49_, 794 (1978).

35. C. A. Hampel, ed., The Encyclopedia of Electrochemistry, Reinhold Publishing Corporation, New York (1964).

36. A. F. Trotman-Dickenson, ed., Comprehensive Inorganic Chemistry, Pergamon Press, Elmsford, NY (1973).

37. R. F. Heidner, III, J. G. Coffer, and C. E. Gardner, O_2 ($^1\Delta$) - I Atom Energy-Transfer Studies: cw Inversion on 1.315-μm I-Atom Transition, Report SAMSO-TR-77-215, Aerospace Corporation, El Segundo, CA, December 1977.

38. Private communication, R. R. Bousek, Air Force Weapons Laboratory, Kirtland Air Force Base, Albuquerque, NM.

9

39. R. L. Herbst, H. Komine, and R. L. Byer, Opt. Commun. __21__, 5 (1977).

40. I. Shoshan and U. P. Oppenheim, Opt. Commun. __25__, 375 (1978).

41. J. J. Snyder, Laser Wavemeter for Pulsed or cw Lasers, presented at the Conference on Lasers and Electro-Optics Systems, San Diego, CA, February 1978.

PUBLICATIONS

MULTILEVEL PARAXIAL MAXWELL-BLOCH EQUATION DESCRIPTION OF SHORT PULSE AMPLIFICATION IN THE ATOMIC IODINE LASER, M. E. Riley (4211), T. D. Padrick/ R. E. Palmer (4212), IEEE Journal of Quantum Electronics (accepted).

LASER BEAM CHARACTERISTICS OF PHOENIX, AN HF OSCILLATOR-AMPLIFIER SYSTEM, E. L. Patterson/G. N. Hays/R. A. Gerber/F. K. Truby (4212), Journal of Applied Physics (accepted).

ENERGY EXTRACTION FROM A LARGE VOLUME HF AMPLIFIER, J. M. Hoffman/ E. L. Patterson/R. A. Gerber (4212), Journal of Applied Physics (accepted).

PULSED ACOUSTO-OPTICAL MODULATOR DRIVER, E. D. Jones/F. R. Franklin (4214), R. E. Palmer/T. D. Padrick (4212), Rev. Sci. Instrum. $\underline{49}$, 1355 (1978).

RAMAN SPECTRUM AND CROSS SECTIONS OF $n-C_3F_7I$: IMPLICATIONS FOR A LARGE-SCALE ATOMIC IODINE LASER, J. C. Cummings/D. P. Aeschliman (4216), and R. E. Palmer (4212), Optics Communications (accepted).

MULTIPLE PHOTON INDUCED CHEMISTRY IN MIXTURES OF C_2F_6 WITH H_2 OR C_6H_{14}, G. A. Fisk (4212), Chemical Physics Letters, $\underline{60}$, 11 (1978).

DIFFRACTION-LIMITED ATOMIC IODINE PHOTODISSOCIATION LASER, R. E. Palmer/ T. D. Padrick (4212), and M. A. Palmer (4234), Optical and Quantum Electronics (accepted).

PRESENTATIONS

BEAM QUALITY MEASUREMENTS OF SANDIA'S HF OSCILLATOR-AMPLIFIER CHAIN, E. L. Patterson/G. N. Hays/J. M. Hoffman/R. A. Gerber/G. C. Tisone/F. K. Truby (4212), and R. P. Sandoval (4214), 10th Int'l Quantum Electronics Conf., IEEE/OSA, Atlanta, GA, May 29-June 1, 1978.

ENERGY EXTRACTION FROM AN ELECTRON-BEAM-INITIATED HF AMPLIFIER, E. L. Patterson/G. N. Hays/G. C. Tisone/J. M. Hoffman and J. B. Moreno (4212), 10th Int'l Quantum Electronics Conf., Atlanta, GA, May 29-June 1, 1978.

BROADENING OF THE CF_3I ABSORPTION BAND NEAR 270 nm BY VIBRATIONAL EXCITATION OF ν_1 WITH CO_2 LASER IRRADIATION, T. D. Padrick/A. K. Hays (4212), and M. A. Palmer (4234), Pacific Conference on Chemistry and Spectroscopy, Society for Applied Spectroscopy and American Chemical Society, San Francisco, CA, 9/27-29/78.

DISTRIBUTION:
TID-4500-R66 UC-21 (208)

US DOE/NS (13)
Washington, DC 20545
Attn: Lt. Gen. A. D. Starbird
     C. M. Stickley (6)
     L. E. Killion
     R. Schriever
     E. Braunschweig
     S. Kahalas
     Maj. Gen. J. K. Bratton
     F. C. Gilbert

US DOE/AE (2)
Washington, DC 20545
Attn: E. Kintner
     B. Miller

US DOE
Albuquerque Operations Office
P. O. Box 5400
Albuquerque, NM 87185
Attn: H. E. Roser, Mgr.

US DOE
San Francisco Operations Office
1333 Broadway
Oakland, CA 94612

Los Alamos Scientific Laboratory (7)
P. O. Box 1663
Los Alamos, NM 87544
Attn: R. Perkins (5)
     O. Judd, AP-DO
     S. Singer, L-1, MS 548

University of California (6)
Lawrence Livermore Laboratory
P. O. Box 808
Livermore, CA 94550
Attn: J. Emmett (5)
     J. Nuckolls

Department of Physics
University of California
Los Angeles, CA 90024
Attn: B. B. Fried

Westinghouse Electric Corporation
Research Laboratories
1310 Beulah Road
Pittsburgh, PA 15235
Attn: W. P. Kovacik

University of California
Los Angeles, CA 90024
Attn: J. Dawson

University of California
Irvine, CA 92664
Attn: N. Rostoker

Cornell University
Ithaca, NY 14850
Attn: R. Sudan

California Institute of Technology
Pasadena, CA 91109
Attn: R. Gould

California Institute of Technology
Elec. Eng. & Applied Science
Pasadena, CA 91125
Attn: W. B. Bridges, 116-81

University of California
P. O. Box 109
La Jolla, CA 92037
Attn: K. Brueckner

University of California
Berkeley, CA 94720
Attn: G. Pimental

University of Southern California
Los Angeles, CA 90007
Attn: J. Marburger

Cal Tech
Department of Physics
Pasadena, CA 91109
Attn: A. Yariv

Rockwell International Corporation
Rocketdyne Division
6633 Canoga Avenue
Canoga Park, CA 91304
Attn: TIC

Office of Director of Defense
Research and Engineering
Room 3E1006, The Pentagon
Washington, DC 20301
Attn: R. Cooper

DISTRIBUTION (cont):

Stanford University (3)
Stanford, CA 94305
Attn: A. Schawlow, Physics Dept.
      A. Siegman, Microwave Lab.
      S. E. Harris, Microwave Lab.

University of Arizona
Tucson, AZ 85721
Attn: M. D. Scully

Environmental Monitoring &
  Support Laboratory
P. O. Box 15027
Las Vegas, NV 89114
Attn: B. J. Mann, Chief
      Evaluation Branch
      Office of Radiation Programs, LVF

Battelle Laboratories (2)
505 King Avenue
Columbus, OH 43201
Attn: L. Masters, AEC Library
      P. Mallozzi

University of Texas at Austin (2)
College of Engineering
Austin, TX 78712
Attn: O. M. Friedrich, Jr., Ass't Director
      Electronics Research Center
      W. Drummond

University of Illinois
Urbana, IL 61801
Attn: J. Verdeyn

Harry Diamond Laboratories (2)
Washington, DC 20438
Attn: R. Oswald
      S. Greybill

Maxwell Laboratories (2)
9244 Balboa Avenue
San Diego, CA 92123
Attn: A. Kolb
      A. Trivelpiece

Physics International (3)
2700 Merced Street
San Leandro, CA 94577
Attn: I. Smith
      S. Putnam
      P. Champney

R&D Associates (2)
P. O. Box 9695
Marina Del Rey, CA 90291
Attn: B. Hartenbaum
      C. McDonald

Combustion Engineering, Inc.
1000 Prospect Hill Road
Windsor, CT 06095
Attn: M. Clark

Imperial College of Science & Technology
London, England
Attn: D. J. Bradley

University of Hull
Hull, England
Attn: S. A. Ramsden

Culham Laboratory
UKAEA Research Group
Abingdon Oxfordshire OX14 3 DB
England
Attn: Mrs. Margaret King

C.I.S.E. Laboratories
Milano, Italy
Attn: F. T. Arecchi

Technische Universitat
Munchen, Germany
Attn: W. Kaiser

Institute of Laser Engineering
Osaka University
Osaka 565, Japan
Attn: C. Yamanaka

Atomic Weapons Research Estab. (2)
Aldermasten, England
Attn: J. C. Martin
      John Weale

National Research Council
Division of Physics
Ottowa, Canada
Attn: A. J. Alcock, Head
Laser & Plasma Physics Sect

75

DISTRIBUTION (cont):

Department of the Army, The Pentagon
Washington, DC 20301
Attn: R. B. Watson
      Chief, Research and Development

Advanced Research Projects Agency (2)
1400 Wilson Blvd.
Arlington, VA 22209
Attn: E. Gerry
      P. Clark

P. Haas (3)
Defense Nuclear Agency
Washington, DC 20305
Attn: G. Soper

USAF/RDPS
Washington, DC 20330
Attn: Col. F. L. Young

US Air Force (3)
Air Force Weapons Laboratory
Kirtland AFB, NM 87117
Attn: Col. O. R. Cunningham, DOUA (2)
      A. H. Guenther, DOUA

Mission Research Institute
P. O. Drawer 719
Santa Barbara, CA 93102
Attn: C. L. Longmire

University of Rochester (5)
Rochester, NY 14627
Attn: M. Lubin

KMS Fusion, Inc. (2)
P. O. Box 1567
Ann Arbor, MI 48106
Attn: H. Gomberg

U. S. Army Missile Command
Redstone Arsenal, AL 35809
Attn: J. P. Hallowes
      Physical Sciences Director

Naval Ordnance Systems Command
Department of the Navy
Washington, DC 20360
Attn: Capt. J. G. Wilson, USN (PMO-405)

U. S. Naval Research Laboratory
Washington, DC 20390
Attn: T. Coffey

Massachusetts Institute of Technology
Mechanical Engineering
Mudd Building, Room 236
Cambridge, MA 02139
Attn: A. Javan

Columbia University
New York, NY 10027
Attn: R. A. Gross

Bell Telephone Laboratories
Network Planning & Customer's Services
Room 2G-602
Holmdel, NJ 07733
Attn: S. J. Buchsbaum, Vice President

Bell Telephone Laboratories (2)
Murray Hill, NJ 07974
Attn: A. M. Clogston
      J. A. Giordmaine

Bell Telephone Laboratories
Holmdel, NJ 07733
Attn: C. K. N. Patel

Electric Power Research Institute (3)
3412 Hillview Avenue
Palo Alto, CA 94304
Attn: R. E. Bolzhiser
      N. Amherd
      W. Gough

Argonne National Laboratory
9700 South Cass Avenue
Argonne, IL 60439
Attn: P. Persiani

United Aircraft Research Labs.
East Hartford, CT 06108
Attn: A. J. DeMaria

Hughes Research Labs.
Malibu, CA 90265
Attn: W. B. Bridges

DISTRIBUTION (cont):

MPB Technologies, Inc.
P. O. Box 160
21051 North Service Rd/
Tran-Canada Highway
Ste-Anne-de-Bellevue, Quebec
H9X 3L5, Canada
Attn: M. P. Bachynski, President

Lawrence Livermore Laboratory
P. O. Box 5508
Livermore, CA 94550
Attn: Wayne L. Johnson, L-482

AFWL Technical Library
Mail Stop: SUL
Kirtland Air Force Base, NM 87117

University of Utah
Department of Electrical Engineering
Salt Lake City, Utah 84112
Attn: R. W. Grow

MAX-PLANCK-INSTITUT FÜR PLASMAPHYSIK
8046 Garching Bei Munchen
Germany
Attn: Ruth Lengyel, Bibliothek

1	M. Sparks
400	C. Winter
1000	G. A. Fowler
1100	C. D. Broyles
1200	L. D. Smith
1400	L. J. Heilman
1500	W. A. Gardner
2000	E. D. Reed
2100	D. M. Olson
2300	J. C. King
2500	J. C. Crawford
2600	L. E. Hollingsworth
3145	L. S. Ostrander
3312	G. E. Tucker, Jr.
4000	A. Narath
4200	G. Yonas (30)
4210	J. B. Gerardo (10)
4211	E. J. McGuire
4212	R. A. Gerber
4214	E. D. Jones
4216	A. W. Johnson
4216	R. A. Hill
4230	M. Cowan
4231	J. H. Renken
4232	W. Beezhold
4234	M. A. Gusinow

4240	G. W. Kuswa (30)
4241	J. R. Freeman (20)
4242	A. J. Toepfer
4244	P. A. Miller
4247	M. M. Weidner
4250	T. H. Martin
4252	J. P. VanDevender
4254	S. A. Goldstein
4400	A. W. Snyder
4420	J. V. Walker
4422	R. L. Coats
4423	J. E. Powell
4451	T. R. Schmidt
4452	L. D. Posey
4700	J. H. Scott
8000	T. B. Cook, Jr.
8100	W. J. Spencer
8200	A. N. Blackwell
8300	B. F. Murphey
8342	P. L. Mattern
8347	W. Bauer
8266	E. A. Aas
3141	T. L. Werner (5)
3151	W. L. Garner (3)
	For DOE/TIC (Unlimited Release)

Org.	Bldg.	Name	Rec'd by *	Org.	Bldg.	Name	Rec'd by *

* Recipient must initial on classified documents.